Master Thesis, Department of Geosciences

Snow Redistribution Modelling in Alpine Norway

Validation of SnowModel for a wet, high mountain climate

Tobias Litherland

UNIVERSITY OF OSLO

FACULTY OF MATHEMATICS AND NATURAL SCIENCES

Snow Redistribution Modelling in Alpine Norway

Validation of SnowModel for a wet, high mountain climate

Tobias Litherland

Master Thesis in Geosciences

Discipline: Hydrology

Department of Geosciences

Faculty of Mathematics and Natural Sciences

University of Oslo

03.05.13

Abstract

The redistribution of seasonal snow is an integral part of the processes controlling soil temperature, permafrost, soil moisture and vegetation distribution, and plays an important role in the planning of infrastructure and hydropower production. Models exist that are able to simulate these snow distributions by using available meteorological data. In this study, an extensive dataset of snow distributions has been collected to evaluate the performance of the snow evolution and distribution model SnowModel. Snow distributions are observed at Finse, a high mountain plateau in Norway, at monthly intervals over 2 winter seasons. Ground Penetrating Radar (GPR) has been used to determine snow depth distribution within a 1 km^2 area. The observations show a heterogeneous snow cover in rough terrain, due to wind redistribution. Additionally, 3 meteorological weather stations were installed and have recorded wind speed, wind direction and temperature. SnowModel is implemented for the study area with a spatial resolution of 4 m and 1 h time steps, and model results are compared with the collected validation data. Initial results suggest that SnowModel is unable to reproduce the observed snow distributions under the given climatic conditions. The issues are accredited to 4 sources: (1) The modelled wind distribution does not show sufficient variation to recreate the observed wind distributions, with a mismatch of 42 %, 50 % and −28 % of the observed wind speed from the validation stations. (2) SnowModel recreates hard, immovable snow layers if temperatures exceed 3 ℃, but does not handle immovable layers created by wind-induced mechanical metamorphism. (3) Snow surface density is reset to the new snow density at any solid precipitation event, regardless of snow surface density evolution up until that point. And (4) simulations show that snow is transported out of the model domain without any snow being introduced upwind in the model domain, leading to a loss of snow. The issues may be due to the climate in alpine Southern Norway, when compared with previous implementations. Methods for improving model performance are discussed and implemented, and manage to rectify the loss of snow out of the domain at the cost of the spatial variation in snow depth.

Foreword

This project has been the brain child of Kjersti Gisnås and me ever since we drew a rough sketch of the study in September 2011. I always wanted to work on a project involving snow, modelling and field work ever since I started taking courses in hydrology. No current projects contained any significant amount of neither field work, modelling nor snow. Therefore we made our own project, with Kjersti studying permafrost and temperature transfer and me studying snow distribution modelling. The 40 days of cold, sunny and spectacular winter field work and the installation of weather stations was made possible with the generous help of Statkraft AS, E-CO Energi AS, CryoMet and the University of Oslo.

A warm thank you to Kjersti Gisnås for being a partner in this endeavour, and for enduring the cold weather, slow snow pits, good food and helicopter rides. It was a pleasure! Thanks to Thomas Vikhamar Schuler for being a very supportive and interested supervisor, with all the time in the world for hour-long discussions on snow modelling. Also, thanks to Glen Liston for the use of SnowModel, feedback on the project and for replying to all my questions.

Thanks to: Erika Leslie from the Finse Alpine Research Station for being a kind and pleasant person, and for helping with everything at Finse; Trond Eiken for technical advice and assistance with the GPR equipment; the Finse Red Cross for when we they were needed; and my wonderful field assistants; Thorben “The Tractor” Dunse, Bas Altena, Sebastian Westermann, Torbjørn Ims Østby, and Christopher D’Amboise.

Thanks to my dad, Darren Litherland, for proofreading, and to all my family for both mental and financial support.

Last, but most importantly, thanks to Margrethe for supporting me when I was tired, cheering me on when things have gone well, and for doing a fantastic job as a field assistant.

I wish you a good read.

Tobias Litherland Oslo, 03.06.13

Table of contents

Figures

Tables

Equations

Code

1 Introduction

Winter precipitation in high latitude mountainous areas falls mainly in the form of snow, producing layers of solid precipitation distributed across the terrain. This distribution strongly affects atmospheric and soil temperatures, radiation balance, permafrost and their active layers, soil moisture and runoff, and the vegetation distribution (Blöschl et al., 1991; Kirnbauer et al., 1994; Marsh, 1999; Liston and Sturm, 2002; Harris et al., 2003; Bruland et al., 2004; Liston and Elder, 2006a). Knowledge of snow distribution is of the utmost importance when forecasting runoff, either to prepare for flooding or to provide predictions for hydropower production, as river discharge during the spring is often governed by mountainous snow (Erxleben et al., 2002). In Norway, an estimated 30% of annual precipitation is solid (seNorge.no, 2013). Even though knowledge regarding mountainous snow cover distributions is important, accurate observations over wide areas are lacking; distributions of solid precipitation have until now been virtually unknown (Liston and Sturm, 2002). Sparse precipitation gauges in mountainous areas, the difficulty and cost associated with successive manual snow depth and distribution measurements, and precipitation gauges underestimating snow fall during wind events all contribute to this lack of knowledge (Yang et al., 1996; Liston and Sturm, 2002).

Wind is the dominant factor governing snow transportation, as mountainous winter precipitation tends to falls when it is windy (Liston et al., 2007). The slope and aspect of the terrain and the location and type of vegetation are the controlling factors concerning where the relocated snow finally settles (Dingman, 2002; Lehning et al., 2008). Consequently, areas with low vegetation height and windy, mountainous areas have a snow cover that is mainly governed by wind direction and speed relocating snow across variations in the terrain (Dingman, 2002; Liston et al., 2007; Mott et al., 2010). In these kinds of areas, blowing snow leads to large scale redistributions of precipitation; snow is moved away from exposed areas and deposited on the lee side of terrain formations and within the bounds of taller vegetation, with transport distances as long as $3\,km$ (Tabler, 1975a; Liston et al., 2007). Sparse precipitation measurement networks in remote arctic and mountainous areas and the low temporal resolution of manual snow surveys make traditional observations incapable of describing these snow distributions on smaller scales (Dingman, 2002; Liston and Sturm, 2002). There has been a need for alternative methods to determine the distribution of snow; methods that do not rely solely on the interpolation of precipitation measurements and manual distribution observations (Liston and Sturm, 2002). The increased importance of

environmental concerns and studies of extreme conditions, and a need for more precise distribution information, has led to the development of distributed snow models (Kirnbauer et al., 1994).

Several models exist that attempt to model spatial redistribution of snow (Essery et al., 2013). These models may be divided into 4 groups; (1) those that calculate the seasonal distribution and evolution of snow, without calculating redistribution by wind (e.g. Tarboton et al., 1994; Marks et al., 1999; Essery et al., 2013); (2) physically based models that calculate redistribution by wind on short time spans (events), but not the seasonal evolution of the snow packs them selves (e.g. Uematsu et al., 1991; Gauer, 2001); (3) empirical, equilibrium snow profile models that estimate static snow distribution characteristics (e.g. Tabler, 1975b); and lastly, (4) models that handle both seasonal evolution and wind events, as is the case with ALPINE3D (Lehning et al., 2006), Isnobal with wind forcings (Winstral et al., 2013) and SnowModel (Liston et al., 2007).

1.1 Objective

The three objectives of this thesis are (1) to establish a calibration and validation scheme for snow distribution models at a high-wind mountainous plateau in mainland Norway, (2) use this scheme to assess the performance of the snow distribution and evolution model SnowModel run at high spatial and temporal resolutions (Liston et al., 2007), and (3) present adjustments to SnowModel with the aim of improving performance for modelling snow in a Norwegian, alpine climate.

Model calibration and validation schemes for high resolution modelling often consist of snow distribution data obtained from Ground Penetrating Radar (GPR) surveys. Examples include: A GPR survey over an area of 4 km^2 at peak snow accumulation on Svalbard and mainland Norway (Bruland et al., 2004); 4 GPR surveys covering 8 km^2 on Svalbard for a single season (Jaedicke and Sandvik, 2002); and aerial GPR scans of 13 km^2 along with LIDAR scans 2 times during a single season in the Swiss alps (Dadic et al., 2010). In this study, snow distribution data was collected monthly using a GPR rig covering 20 km of gridded tracks each month from a study area at Finse, an alpine plateau in the southern Norwegian mountains. The study area was surveyed 4 times per season through the winters of 2011-2012 and 2012-2013, for a total of 8 complete GPR sets of the study area. The aim is to be able to assess the intra-annual evolution of the snow cover variation through the accumulation

season, and any models ability to recreate these variations. As the primary interest is the accumulation season, GPR surveys were performed up until the melt season began. Wind is a primary driving force behind wind accumulation and erosion (Uematsu et al., 1991). Observations therefore also consist of meteorological data collected from 3 meteorological stations installed within the study area as part of this project. The meteorological data consists of wind speed, wind direction and temperature logged at $1\ h$ intervals.

These data are then used to assess the performance of SnowModel. Of resent date, several studies have run high resolution simulations using SnowModel: (1) On Svalbard with a $25\ m$ grid size and $6\ h$ temporal resolution (Bruland et al., 2004); (2) in the German alps with $30\ m$ and $200\ m$ grid size and $1\ h$ temporal resolution (Bernhardt et al., 2009; Bernhardt et al., 2010); (3) and in the Chilean mountains with a $90\ m$ spatial resolution and $24\ h$ temporal resolution (Gascoin et al., 2012). In this study, the model will be run within its stated operational bounds, but at a higher resolution than previous studies over a test site at Finse, Norway. SnowModel is implemented with a $4\ m$ spatial and $1\ h$ temporal resolution for the two winter seasons. The model performance is evaluated by comparing modelled snow and wind speed distributions with the observed validation data. Attempts are also made to adjust parameterizations within SnowModel with the aim of improving model performance in simulating snow distributions for the study area.

First, the methodology behind the collection of GPR and weather validation data is presented. Secondly, the structure and methodology of SnowModel is presented. Results of the data collection and the initial modelling are then presented in separate chapters, followed by a discussion and presentation of model sensitivity tests and adjustments. Lastly, a general discussion of data collection and model results is presented followed by a conclusion.

2 Study area

The selected study area is located just south east of the village of Finse in Southern Norway (Figure 1). Finse lies in Hordaland County and is part of the Hardangervidda plateau, at the north end of Hardangervidda National Park. It is the highest point on the railway between Oslo and Bergen, and is only accessible by train, snowmobiles or skis during wintertime. Finse is also home to the Finse Alpine Research Station, operated by the Universities of Oslo and Bergen. The research station has been the base of operations for the field work conducted in this study. The study consists of a $1\,km^2$ grid over Vesle Hansbunut, a hill to $4\,km$ south east of Finse (Figure 2). Vesle Hansbunut rises $150\,m$ above the surrounding terrain, and features a rough, undulating topography.

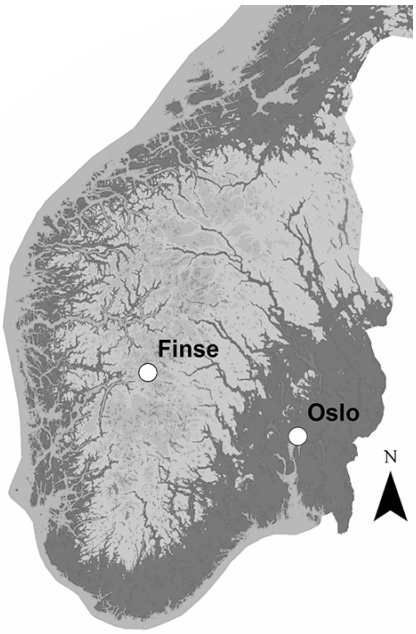

Figure 1 – The location of Finse in southern Norway.

2.1 Topography and vegetation

Hardangervidda is Europe's largest alpine plateau at 10 000 km^2, with the entire area located above the tree line at elevations between 1100 and 1800 m above sea level (Sømme and Østbye, 1997; Store Norske Leksikon, 2012). Most of the plateau is covered in moraine material, with accumulations of sand, gravel and boulders (Store Norske Leksikon, 2012). Vegetation is dominated by moss, alpine shrubs and grass, with bare outcrops and peaks.

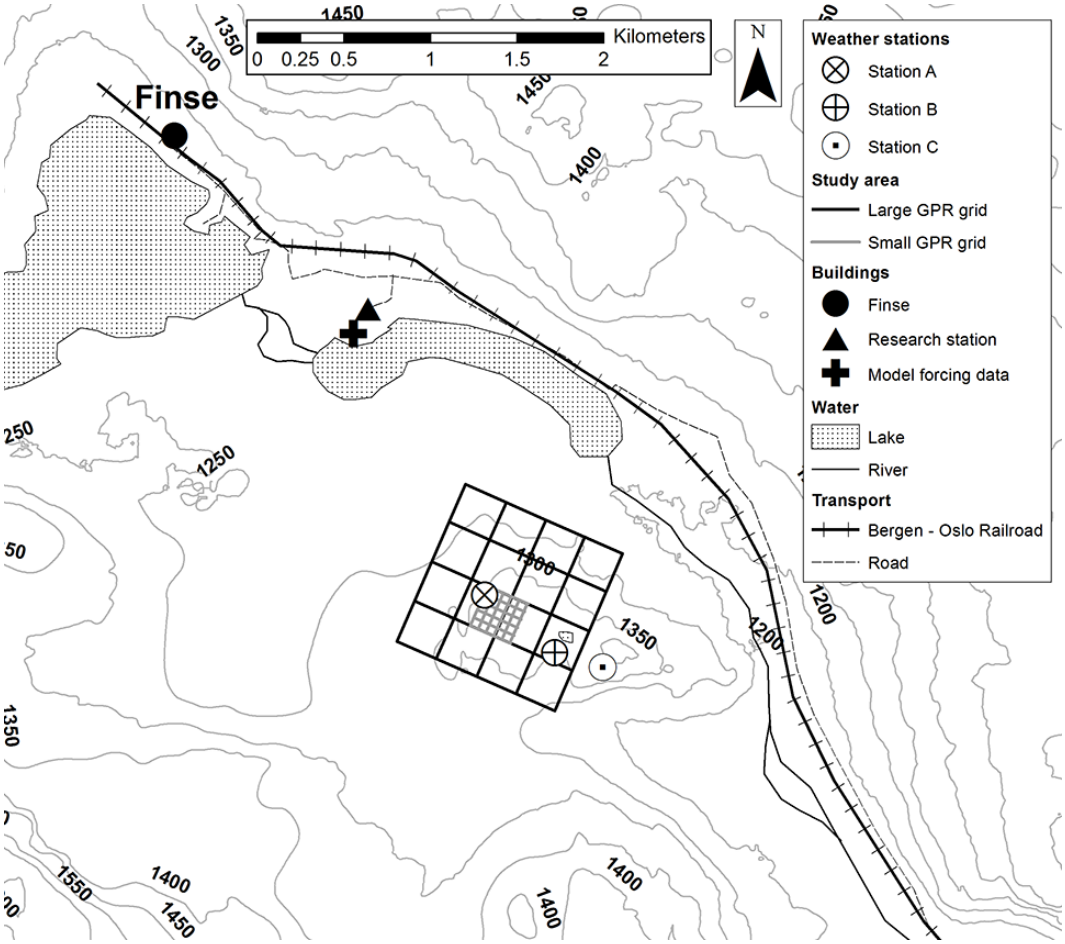

Figure 2 – Map over study area, showing GPR grids and locations of meteorological stations. The model forcing data is the met.no operated Finsevatn meteorological station. GPR grid covers Vesle Hansbunut, with it's peak just above 1350 m.

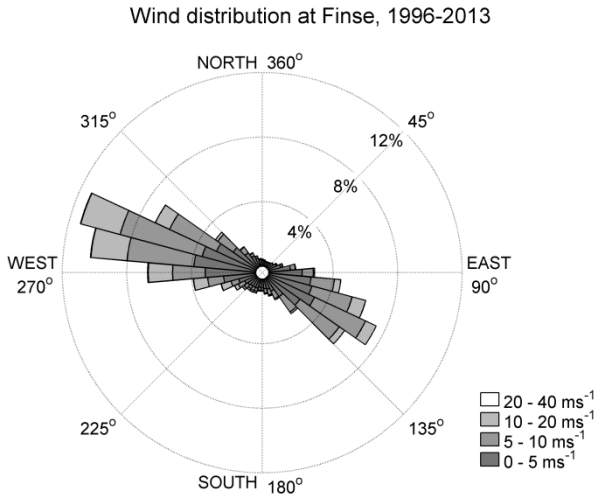

Figure 3 – Wind rose showing the observed 10 m wind speed distribution of the Finse meteorological weather station for the time period 1996-2012.

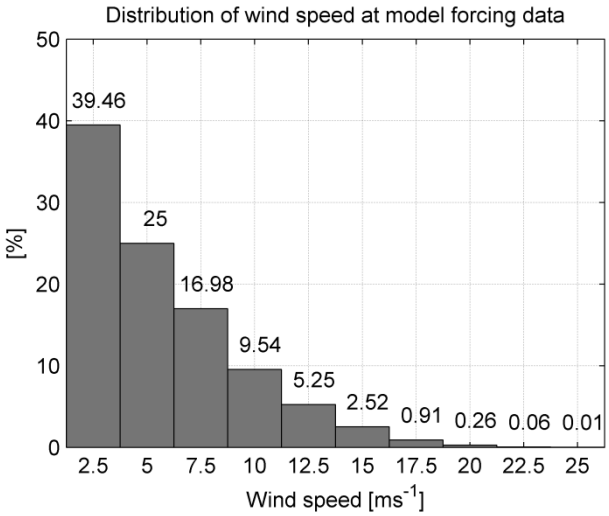

Figure 4 – 10 m wind speed distribution at 2.5 ms^{-1} intervals (± 1.25 ms^{-1} on stack label) for the Finse meteorological weather station for the time period 1996-2012.

2.2 Climate

Finse is located on the boundary between a continental and a coastal climate, with Finse being mainly dominated by warm moist air from the Atlantic ocean to the west (Pomeroy and Gray, 1990). The contrast between the maritime air masses from the west, and the dryer continental air coming from the east, results in large variations in weather depending on the wind direction. There are steep precipitation gradients along a west-east axis; Myrdal $30\ km$ to the west of Finse and Haugastøl $25\ km$ to the east experience $175\ \%$ and $70\ \%$ of the annual precipitation of Finse, respectively (Sømme and Østbye, 1997). The precipitation is strongly influenced by orographic effects; the glacier Hardangerjøkulen to the south of Finse receives 3-4 times as much precipitation as Finse (Sømme and Østbye, 1997).

Finse has a mean annual precipitation of $1027\ mm$, and the average winter ground snow cover is $1.6\ m$ (Berthling et al., 2001). Due to the amount of precipitation and a prevalence of high-altitude lakes and reservoirs, Hardangervidda represents a substantial source of hydroelectric power (Store Norske Leksikon, 2012).

The local winds at Finse are strongly influenced by the channelling effect of the local topography, resulting in 70% of all wind events occur along the west-east axis of the valley and the strongest winds coming from the west (Figure 3). Wind speeds are generally high, with an average winter (December through March) wind speed of $6.45\ m\ s^{-1}$ (Figure 4).

3 Validation data collection

3.1 Ground penetrating radar

Ground penetrating radar (GPR) data was collected using a commercially available antenna and receiver system coupled with a GPS receiver for positioning data. The GPR rig was pulled behind a snowmobile in a specially prepared sled, containing all necessary equipment. The highest amplitude return signals are from the snow-ground interface (Yamamoto et al., 2004). Data processing involved manually tracking reflection horizons, and converting two-way-travel times into depths using observed bulk snow density according to Kovacs et al. (1995). For a full description of GPR theory and methodology, see Appendix A.

3.1.1 Post processing

GPR measurement are acquired at intervals of $0.25\ s$. The spatial point density of snow depth recordings is therefore a function of the horizontal movement of the antenna. For further analysis purposes, the spatial distribution of data should be spatially homogeneous to prevent sampling a bias towards areas were snowmobile speed is low. A function was therefore written in MATLAB to rescale point measurements according to a raster congruent with the model output. If several snow depth measurements were located within the same grid cell, the script calculates the average depth. Output of this script also contains the maximum, minimum and standard deviation of snow depths within grid cells allowing a study of sub-grid variability at points of interest.

Figure 5 – Performing snow pit surveys in January 2012. The aluminium tube is seen at the bottom of the extracted column. The pit shown is $1.41\ m$ deep. (photo: Tobias Litherland)

3.1.2 Snow pit surveys

Representative bulk snow density is used to convert GPR signal time recordings to actual snow depths. These densities were collected from snow pit surveys every time a GPR data set was

collected. The surveys consisted of digging a pit down to the ground surface and extracting and weighing columns of snow (Figure 5). 2 columns were extracted for each pit, piece by piece, using a 20 cm long and 500 cm^3 aluminium tube. The sections were weighed, and the section density calculated. The surveys were performed at Station A and B, and averaged to get a representative density for the study area. An uncertainty analysis of the density data was also performed, with regards to the impact on snow depth calculations.

3.1.3 Calibration data

Manually tracking reflection horizons in the GPR data may introduce depth offsets in the form of tracking the wrong return wavelength. Manual snow depth measurements were performed to measure this uncertainty. These measurements were done with a snow probe at the same time as data was collected by GPR. The snow probe was inserted into the snow close to the GPR antenna, and the depth was recorded. This depth was then compared with the processed GPR depth.

3.2 Meteorological validation data

SnowModel's spatial interpolation of wind speed and wind direction is, along with calculations of snow surface threshold friction velocity, pivotal for the performance of the model in general. 3 meteorological stations were installed within the study area to validate this spatial interpolation. The stations all contain sensors for measuring temperature, wind speed and wind direction, and perform measurements every 4 min while logging the average value every 1 h.

The location of each station is selected to capture the variation in topography in the study area (Figure 6). Station A is located in a north-west moderate slope of little curvature facing the prevailing westerly winds. Station B is located in a south-east slope in a positive curvature on the lee side of a hill. Station C is placed near an exposed top just to the east of the study area. This variation in location should capture the local topographic effects on wind speed. Precise locations, elevations and sensor heights for each station is found in Table 1. For a complete description of the equipment and construction schematics, see Appendix B.

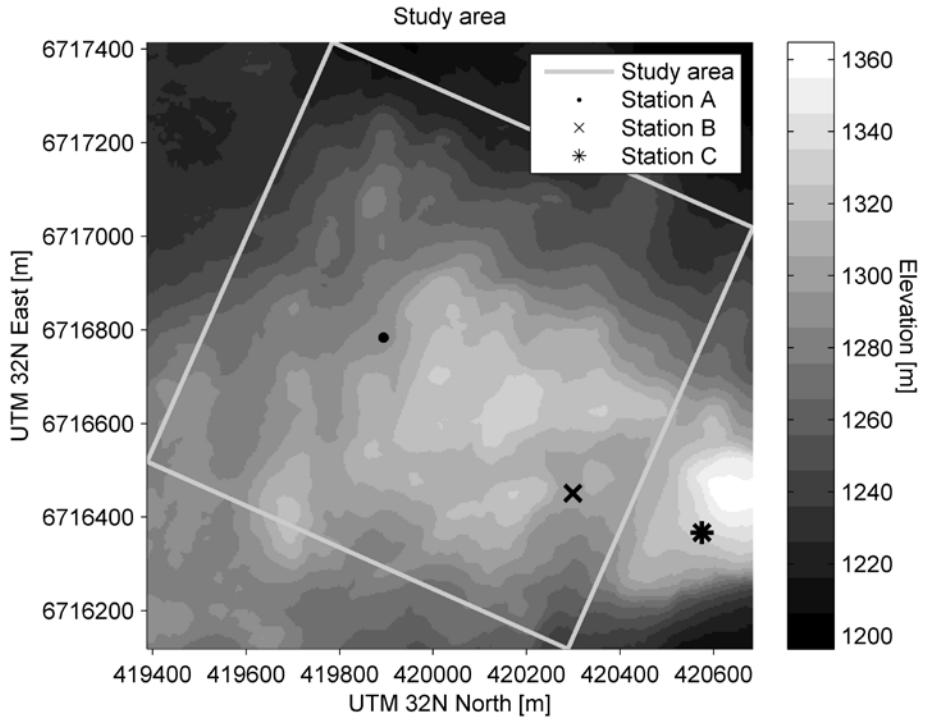

Figure 6 – Study area topography and the location of the meteorological validation stations.

Table 1 – Information on meteorological validation stations. All data for this thesis was downloaded from the stations on March 19th 2013.

	Station A	Station B	Station C
Sensor height	3.80 m	4.20 m	2.30 m
UTM 32N North	6716784	6716451	6716367
UTM 32N East	419894	420299	420575
Elevation	1294 m	1300 m	1336 m
In operation from	March 23rd 2012	October 22nd 2012	March 23rd 2012

3.2.1 Operational time spans

Station A and C were in operation logging wind speed, direction and temperature from the 23rd of March 2012. Installation of sensors for Station B was impossible at this time due to the station being completely buried in snow. After an extension in October 2012, Station B has also collecting data on wind speed, direction and temperature. Meteorological validation data for this thesis was collected from the stations on March 19th 2013.

After a freeze event in December 2012 the wind sensor of Station A stopped working. The station has continued to measure only wind direction and temperature since then.

3.2.2 Treatment of missing or bad data

The data from the stations are controlled by a MATLAB program which checks for and removes erroneous data, repeating values of more than 4 hours, and values exceeding maximum and minimum thresholds. Temperature thresholds are set at a minimum of -35 ℃ and a maximum of 35 ℃, while wind speed is limited at $0\ m\ s^{-1}$ and $40\ m\ s^{-1}$. The resulting gaps in the series are not filled in, as only actual observed values are used in comparison with model output.

3.2.3 Height scaling of wind

Varying sensor height introduces a systematic bias in wind speed measurements. Each station has a different initial height above ground to account for local snow accumulation conditions, and the increasing snow cover through the winter will also impact the effective sensor height. To have comparable station data, wind speed needs to be downscaled to a uniform height above ground. As the height above ground is constantly varying, Each station is equipped with automatic temperature loggers at $10\ cm$ intervals up to $2\ m$ above the ground. The loggers track the temperature on a daily resolution. Along with the air temperature sensor their data can be used to estimate the snow depth with a $\approx 10\ cm$ accuracy for each day. These depths are calibrated with manual snow depth measurements every month.

Scaling wind down to a uniform height can then be done by the Prandtl-von Karman Universal Velocity-Distribution for turbulent flow (Equation 1).

$$v_z = \frac{1}{k} u_* \ln\left(\frac{z_h - z_d}{z_0}\right) \quad z_h > z_d + z_0 \qquad \text{Equation 1}$$

Here, $v_z\ [ms^{-1}]$ is the wind velocity at sensor height $z_h\ [m]$, $u_*\ [ms^{-1}]$ is the friction velocity, $z_d\ [m]$ is the zero-plane displacement, z_0 is the roughness height, and $k\ [1]$ is a constant (Pomeroy and Gray, 1990; Dingman, 2002). Usually, $k = 0.4$ (ibid). The roughness z_0 is set to $0.001\ m$, equal to the default roughness set internally in SnowModel. This keeps wind speeds consistent and comparable between data sets. The zero-plane displacement z_d is defined to account for non-zero velocity at maximum vegetation height. Since snow cover has a more solid boarder, we define $z_d = 0\ m$. On the other hand, the actual sensor elevation at

the meteorological station is a function of snow depth. The sensor height is $z_h - z_{sn}$, where z_{sn} is the snow depth at time step n. The wind speed for time step n at sensor height z_h is defined as $v_{z_h n}$. The friction velocity u_* can then calculated as

$$u_* = \frac{v_{z_h n} k}{\ln\left(\frac{z_h - z_{sn}}{z_0}\right)}. \quad \text{Equation 2}$$

Equation 2 is inserted for u_* in Equation 1, resulting in the final equation:

$$v_{2n} = \frac{v_{z_h n}}{\ln\left(\frac{z_h - z_{sn}}{z_0}\right)} \ln\left(\frac{z}{z_0}\right). \quad \text{Equation 3}$$

As the friction velocity for a the sensor is known, the $2\ m$ wind speed at any given time step can be calculated by $z = 2\ m$ in

$$v_{2n} = \frac{v_{z_h n}}{\ln\left(\frac{z_h - z_{sn}}{0.001}\right)} \ln\left(\frac{2}{0.001}\right). \quad \text{Equation 4}$$

Equation 4 is now an equation for $2\ m$ wind speed v_{2n} as a function of sensor wind speed $v_{z_h n}$ for sensor height z_h, snow depth z_{sn} at observation n.

The total set of daily snow depth measurements were not available by the time this thesis was finished. All analysese of wind speed will therefore be done by scaling wind speed to a uniform height of $2\ m$.

4 Model description

SnowModel is a spatially distributed snow-evolution modelling system designed to handle snow accumulation; blowing-snow redistribution and sublimation; forest canopy interception, unloading and sublimation; snow density evolution; and SnowPack ripening and melt (Liston et al., 2007). The model is developed by Glen Liston and others over several years (Liston and Sturm, 1998; Liston and Elder, 2006a, 2006b; Liston et al., 2007) and it has been tested on a wide range of areas prone to snow redistribution; Colorado (Greene et al., 1999), Antarctica (Liston et al., 2000; Liston and Winther, 2005), Idaho (Prasad et al., 2001), Wyoming (Heimstra et al., 2002), Alaska (Liston et al., 2002; Liston and Sturm, 2002), Greenland (Hasholt et al., 2003; Mernild, Liston, Steffen, et al., 2010; Mernild, Liston, van den Broeke, et al., 2010; Mernild et al., 2011), Svalbard (Bruland et al., 2004) and Germany (Bernhardt et al., 2009).

It is tested for spatial grid sizes of 1 meter to 200 meters, and time intervals of 10 minutes to 1 day. The model requires precipitation, temperature, wind direction, wind speed and humidity as meteorological input (Liston and Elder, 2006a). It is a modular program, made up of several sub-models that handle specific snow-related calculations. The sub-models are MicroMet for meteorological interpolation and general handling; SnowTran-3D for distribution and sublimation by wind; EnBal handles energy balance calculations; and SnowPack deals with layering, density and snow depth. Here follows a description of all sub models.

4.1 Processing of meteorological input

SnowModel's meteorological forcings are handled by MicroMet, a quasi-physically-based, high-resolution, meteorological distribution model that handles air temperature, relative humidity, wind speed, wind direction, incoming solar radiation, incoming long-wave radiation, surface pressure and precipitation (Liston and Elder, 2006b).

MicroMet contains a set of interpolation methods for each of the meteorological variables it handles, both horizontally and vertically, by taking into account the DEM input in SnowModel (Liston and Elder, 2006b). Point data is scaled to an arbitrary, uniform height, interpolated, and then scaled back to actual elevation using the DEM and any applicable elevation lapse rates. The spatial interpolation applies a variant of a Gaussian distribution for distance weighting of station values (ibid). The simulations in this study use a single meteorological station, so the between-station interpolation is not used.

4.1.1 Temperature and humidity

Temperature and humidity are calculated as a function of elevation by monthly linear lapse rates (Table 2).

4.1.2 Precipitation

Precipitation elevation adjustment uses an adjustment factor χ $[km^{-1}]$ found in Table 2 in the equation

$$P = P_0 \left[\frac{1 + \chi(z - z_0)}{1 - \chi(z - z_0)}\right]. \quad \text{Equation 5}$$

Here, P_0 $[mm]$ is the observed station precipitation, z_0 $[m]$ is the interpolated station elevation surface and z $[m]$ is the elevation precipitation is interpolated to.

4.1.3 Radiation and surface pressure

MicroMet also contains sub-models for the calculation of short wave and long wave radiation and surface pressure fields on the basis of the other input, if the radiation and pressure data is not defined. For an in depth description, see Liston and Elder (2006b).

Table 2 – Overview of hard-coded monthly elevation lapse rates for temperature, vapour pressure and precipitation for SnowModel (Liston and Elder, 2006b).

Month	Air temperature lapse rate (°C km^{-1})	Vapour pressure coefficient (km^{-1})	Precipitation adjustment factor (km^{-1})
January	4.4	0.41	0.34
February	5.9	0.42	0.35
March	7.1	0.40	0.35
April	7.8	0.39	0.30
May	8.1	0.38	0.25
June	8.2	0.36	0.20
July	8.1	0.33	0.20
August	8.1	0.33	0.20
September	7.7	0.36	0.20
October	6.8	0.37	0.25
November	5.5	0.40	0.30
December	4.7	0.40	0.35

4.1.4 Wind speed and direction

Wind speed and wind direction are radial values, and the values are decomposed into x- and y-directional wind speeds before being interpolated. The calculations are

$$u = -W sin\theta \quad \text{Equation 6}$$

$$v = -W cos\theta \quad \text{Equation 7}$$

where W ($m\,s^{-1}$) is wind speed, θ (°) is the wind direction, and u and v ($m\,s^{-1}$) are the wind velocities in x and y direction, respectively. u and v are then interpolated across the domain, before they are recompiled as radial values by

$$W = (u^2 + v^2)^{\frac{1}{2}}$$ Equation 8

$$\theta = \frac{3\pi}{2} - \tan^{-1}\left(\frac{v}{u}\right).$$ Equation 9

The addition of $3\pi/2$ is to shift the zero azimuth to north (i.e. upwards in a plot). Wind speed is influenced by 4 topographic characteristics; concave features and lee slopes decrease wind speed, while convex features and windward slopes increase wind speed (Liston and Sturm, 1998). On the basis of these shapes, the module modifies the wind speed and direction according to the terrain features. The terrain slope, designated by β is calculated as

$$\beta = \tan^{-1}\left[\left(\frac{dz}{dx}\right)^2 + \left(\frac{dz}{dy}\right)^2\right]^{\frac{1}{2}}.$$ Equation 10

Here, z (m) is the topographic height and x and y are horizontal coordinates. dz/dx and dz/dy are the changes in elevation in the grid point in direction x and y. In total, the function calculates the amount of tilt of the terrain at a specific coordinate as the angle of the vector sum of the slope in x- and y-direction. The aspect of the slope (i.e. the angle between the horizontal slope direction and the zero azimuth), is calculated as

$$\varepsilon = \frac{3\pi}{2} - tan^{-1}\left(\frac{\frac{dz}{dy}}{\frac{dz}{dx}}\right).$$ Equation 11

The slope β and the aspect ε are then used to calculate the actual slope in the wind's direction Ω_s:

$$\Omega_s = \beta \cos(\theta - \varepsilon),$$ Equation 12

where β is the slope at the given point, ε is the aspect, and θ is the direction of the wind.

Curvature in the direction of the wind is calculated by a more complex formula, using a parameter μ, called the curvature length scale. μ defines the distance over which a height difference calculation is performed, to identify if a point is located on a convex or concave feature. μ is therefore a measure of the size of the features relevant to the snow distributions, and is defined as one-half of the topographic wave length; the distance between a snow-eroded top to a depression that receives snow (Liston et al., 2007). The curvature is calculated

along 4 axes; south-north, west-east, southwest- northeast and northwest-southeast. The calculation of the topographic curvature is done by

$$\Omega_c = \frac{1}{4}\left[\frac{z-\frac{1}{2}(z_S+z_N)}{2\mu}+\frac{z-\frac{1}{2}(z_W+z_E)}{2\mu}+\frac{z-\frac{1}{2}(z_{SW}+z_{NE})}{2\mu}+\frac{z-\frac{1}{2}(z_{NW}+z_{SE})}{2\mu}\right]. \quad \text{Equation 13}$$

z indicates the elevation in the point of interest, and z_x is the elevation at a distance equal to curvature length scale μ away from the point of interest, in the direction indicated by subscript x (Liston et al., 2007). In essence, the formula calculates the average inclination/declination per meter in 4 sets of opposite directions. The curvature Ω_c is only calculated using the terrain, and is not a function of wind direction, as opposed to Ω_s. As a result Ω_c and Ω_s are in the interval $[-0.5, 0.5]$ (Liston et al., 2007).

Any given point in the terrain now has a wind speed W, a curvature Ω_c and a slope Ω_s (where the slope is in the winds direction θ). Wind speed W is then corrected by

$$W_t = (1 + \gamma_s\Omega_s + \gamma_c\Omega_c) * W. \quad \text{Equation 14}$$

Here, γ_s and γ_c are the adjustable weights that controll the relative importance of the slope and curvature influence on wind speed. Liston proposes that in operational runs of the model, the weights be set so that $\gamma_s + \gamma_c = 1$ (Liston et al., 2007), although this is not required (Liston's comment in model code). SnowTran-3D also implements a wind diversion algorithm that changes the direction of the wind according to the slope and aspect of terrain features it encounters. The algorithm is given by

$$\theta_t = \theta - 0.5\Omega_s \sin\big(2(\varepsilon - \theta)\big), \quad \text{Equation 15}$$

where θ is the original, interpolated wind direction; Ω_s is slope in the direction of the wind; and ε is the aspect of the terrain in the selected point. The combination of wind speed W_t and direction θ_t is then decomposed back to perpendicular vectors u and v, which are then used in the snow transport equations of SnowTran-3D.

4.2 Energy balance calculations

Standard surface energy balance calculations are handled by the EnBal-submodel (Liston and Elder, 2006b). This subroutine simulates surface temperatures, moisture and energy fluxes in response to simulated atmospheric conditions. The output from MicroMet is fed into a surface energy balance given by

$$(1-\alpha)Q_{si} + Q_{li} + Q_{le} + Q_h + Q_e + Q_c = Q_m. \quad \text{Equation 16}$$

Here, α [1] is the surface albedo, Q_{si} is the solar radiation, Q_{li} is the incoming longwave radiation, Q_{le} is the emitted longwave radiation, Q_h is the turbulent exchange of sensible heat, Q_e is the turbulent exchange of latent heat, Q_c is the conductive energy transport, and Q_m is the energy flux available for melt (Liston and Elder, 2006a). All energy components Q have the unit [$W\ m^{-2}$]. The model handles different albedos according to surface cover, with classifications for snow, ice, snow below forest canopies, snow in forest free areas and glacier ice. For in depth descriptions of the components of Equation 16, see Liston and Hall (1995) and Liston (1995).

4.3 Metamorphism of snow

The SnowPack submodel handles snow pack changes and melt according to the data from MicroMet and EnBal. Evolution of snow pack density is calculated as a function of snow temperature, the weight of overlaying snow and snow melt (Liston and Elder, 2006a).

Density is initially set by calculating the new snow density of any newly fallen snow.

$$\rho_{ns} = 50 + 1.7(T_{wb} - 258.16)^{1.5} \quad T_{wb} \geq 258.16 \quad \text{Equation 17}$$

where T_{wb} [K] is the wet-bulb temperature calculated according to Liston and Hall (1995). This density is then updated according to melt and compaction. Compaction is calculated according to Anderson (1976) as

$$\frac{\partial \rho_s}{\partial t} = A_1 W_s \rho_s\, e^{-0.08(T_f - T_s)} e^{-A_2 \rho_s}, \quad \text{Equation 18}$$

where $\partial\rho_s/\partial t$ [$kg\ m^{-3}\ s^{-1}$] is the change in snow density as a function of time, T_s [$°K$] is the snow temperature, T_f[$°K$] is the freezing temperature, and A_1 and A_2 are constants at $0.0013\ m^{-1}\ s^{-1}$ and $0.021\ m^3\ kg^{-1}$ respectively (Liston and Hall, 1995). Melting snow

reduces the depth of the snow pack and subsequently increases the density. When a maximum snow density of $550\ k\ gm^{-3}$ is reached, any excess melting or rainfall will be removed as discharge. The potential snow melt is calculated by

$$\rho_i L_f \frac{dM_p}{dt} = Q_m. \quad \text{Equation 19}$$

Here, ρ_i $[k\ gm^{-3}]$ is the snow density, L_f $[J\ kg^{-1}]$ is the latent heat of freezing, M_p $[m^3]$ is the amount of water melted, t $[s]$ is the time, and Q_m $[J\ s^{-1}]$ is the energy available for melting (Liston and Hall, 1995).

4.4 Wind redistribution

Wind is the most important factor when it comes to redistributing snow on a large scale (Liston et al., 2007). In SnowModel, SnowTran-3D is the submodel that handles the redistribution of snow. The model is mainly tested in arctic and continental, low-vegetation areas with below freezing temperatures, strong winds and solid precipitation (Liston et al., 2007). The sub-models primary components are (1) a forcing field generated from wind flow, (2) calculations regarding the wind-shear stress on the ground/snow surface, (3) saltation and turbulent suspension of snow, (4) sublimation of the saltating and suspended snow (as sublimation of moving snow is higher than snow lying still (Tabler, 1975a; Zhang et al., 2004)), and (5) the accumulation and erosion of snow by wind (Liston et al., 2007). SnowTrans-3Ds basis is a wind field and a mass-balance equation that for each point in the simulation domain calculates the flux in saltation, suspension, sublimation and precipitation.

The actual transport of snow is handled by a mass balance equation that controls deposition and erosion (Liston et al., 2007). In mathematical terms, the equation is of the form

$$\frac{d(\rho_s h)}{dt} = \rho_w P - \left(\frac{dQ_{salt_x}}{dx} + \frac{dQ_{turb_x}}{dx} + \frac{dQ_{salt_y}}{dy} + \frac{dQ_{turb_y}}{dy}\right) + Q_v, \quad \text{Equation 20}$$

where; h (m) is snow depth; ρ_s and ρ_w $(kg\ m^{-3})$ are the densities of snow and water, respectively; P (m) is precipitation; Q_{salt} and Q_{turb} $(k\ gm^{-1}\ s^{-1})$ are saltation transport rate and turbulent suspension transport rate; and Q_v $(kg\ m^{-2}\ s^{-1})$ is the amount of sublimated snow (Liston et al., 2007). Saltation and suspension are derivatives in x- and y-direction, to differentiate between directions of movement (the wind field is divided into north-south and east-west components, and these are reflected in the x and y components of

the snow movement). The individual components are described in depth in the following papers; Q_{salt} in (Pomeroy and Gray, 1990); Q_{turb} in (Kind, 1992) and Liston and Sturm (1998); and Q_v in Liston and Sturm (1998).

SnowTran-3D also handles variations in the threshold friction velocity of the snow; the amount of wind speed needed to move the snow at any given time at any given place (Liston et al., 2007). The threshold friction velocity u_{*t} is calculated as a function of surface snow density. The calculations of surface density are separate from the calculations of bulk snow density for the snow pack. The surface density is only used for calculations of threshold friction velocity, while the bulk density is used to handle snow depth and water balance.

SnowTran-3D treats the snow as being composed of two layers; one soft top layer containing snow available for moving, and one hard layer containing immobile snow. The entire snow pack is defined as immobile if temperature exceeds 3 ℃ or if the surface density is sufficiently high (Liston et al., 2007). The soft layer is represented as a fraction of the total snow water equivalent depth, and the soft layer density is used for calculating threshold friction velocities. The initial density of soft layer ρ_s $[kg\ m^{-3}]$ is the sum of new snow density ρ_{ns} and the wind-related density offset ρ_w:

$$\rho_s = \rho_{ns} + \rho_w \qquad \text{Equation 21}$$

Here we have the new snow surface density defined as

$$\rho_{ns} = 50 + 1.7(T_{wb} - 258.16)^{1.5} \quad T_{wb} \geq 258.16 \qquad \text{Equation 22}$$

where T_{wb} $[K]$ is the wet-bulb temperature calculated within SnowModel according to Liston and Elder (2006a). Equation 22 is the same as the one used to calculate new snow density in SnowPack. SnowPack does not include the wind-related density offset ρ_w, so bulk density is not affected by wind. The wind offset for the density is found as

$$\rho_w = D_1 + D_2\left(1.0 - e^{-D_3(W_t - 5.0)}\right) \qquad \text{Equation 23}$$

where W_t $[ms^{-1}]$ is the terrain modified wind speed at $2\,m$, and D_1, D_2 and D_3 are parameters at $25\,kg\,m^{-3}$, $250\,kg\,m^{-3}$ and $0.2\,m\,s^{-1}$. The change in surface density ρ_s $[kgm^{-3}]$ as a function of time t [s] is calculated by

$$\frac{\partial \rho_s}{\partial t} = CA_1 U \rho_s e^{\left(-B(T_f - T_s)\right)} e^{(-A_2 \rho_s)}$$ Equation 24

where $U\ [m\ s^{-1}]$ is the wind speed, and T_f [℃] and T_s [℃] are the freezing and snow temperatures respectively (Liston et al., 2007). A_1, A_2 and B are constant set to $0.08\ K^{-1}$, $0.0013\ m^{-1}$ and $0.021\ m^3\ kg^{-1}$ according to Kojima (1967). C [1] is a constant for controlling the rate of snow density change. For wind speeds above $5\ m\ s^{-1}$, U is calculated by

$$U = E_1 + E_2\left(1.0 - e^{-E_3(W_t - 5.0)}\right).$$ Equation 25

Here, $W_t\ [m\ s^{-1}]$ is the terrain-modified wind speed, with the constants E_1, E_2 and E_3 controlling the offset wind, maximum wind and progression at $5.0\ m\ s^{-1}$, $15.0\ m\ s^{-1}$ and $0.02\ m\ s^{-1}$, respectively. Any wind speed lower than $5.0\ m\ s^{-1}$ is assumed to not have an effect on the compaction of snow and U is therefore set to 0 (Liston et al., 2007).

The resulting surface density ρ_s is used to calculate the threshold friction velocity u_{*t} by

$$\begin{aligned} u_{*t} &= 0.10e^{0.003\rho_s} \quad for\ 50 < \rho_s \leq 300 \\ u_{*t} &= 0.005e^{0.013\rho_s} \quad for\ 300 < \rho_s \leq 450. \end{aligned}$$ Equation 26

This threshold velocity is then compared with the modelled surface wind velocity to control wind transport (Liston et al., 2007).

Improvements to SnowTran-3D in 2007 (Liston et al., 2007) included calculating Tabler-surfaces for controlling the maximum amount of snow depth for any given topographical snow trap. These calculations are turned off in our simulations due to simulations artefacts when implemented.

5 Model application

5.1 Scale and resolution

The model was run with a $4\,m$ spatial resolution and a $1\,h$ temporal resolution. The model is run for 3 separate time periods. Snow distribution data for the 2 winter seasons is modelled for the time period of October 10th to April 1st for both winter of 2011-2012 and 2012-2013. Simulations for the validation of temperature, wind speed and wind direction were run from March 19th 2012 to March 19th 2013 to capture the entire data period for the meteorological validation stations.

Vegetation at Finse is generally very sparse, and a significant portion of the terrain is bare rock or unconsolidated material with low growing moss. Field observations also indicate that vegetation plays an insignificant role in the accumulation of snow in the study area, with the exception of a few shrubberies up to a height of 20 to $30\,cm$ which might affect snow distribution in early winter. Snow cover is generally far deeper than any vegetation height, so a uniform vegetation height of $20\,cm$ was applied to the simulations to account for accumulation in any low shrubberies. Detailed vegetation data is not readily available for the study area

The terrain model for the study area was derived from aerial photographs and has a resolution of $4\,m$. The photographs only cover the immediate area around the study area, so the terrain model is padded with a downscaled $10\,m$ DEM from the Norwegian Mapping Authority, and masked to fit the chosen modelling domain.

According to Liston, the model needs a boundary of 2 to $3\,km$ around the study area to keep the net snow flux within the study area at a minimum (pers.com. Liston, 2012) (Appendix E.1). Otherwise, snow might blow out of the modelling domain without any new snow being reintroduced at the upwind boundary. Available computer memory limits this study's model implementation to a total of about $3 * 10^6$ grid cells, depending on configuration. A modelling domain of 2500 by 1000 grid cells with a $4\,m$ resolution is therefore used, covering a total area of $40\,km^2$ (Figure 7). The rectangular shape of the modelling area is devised to accommodate the prevailing wind direction and thereby keep the net flux of snow through the study area at a minimum. With the prevailing winds occurring on an east-west

axis, the distance between the study area and the model boundary is approximately 4 km along and 2 km perpendicular to the prevailing winds.

All model runs for snow distributions and SWE calculations produce diurnal output for both winters of 2011-2012 and 2012-2013.

For temperature, wind speed and direction, the model is run with 1 h output.

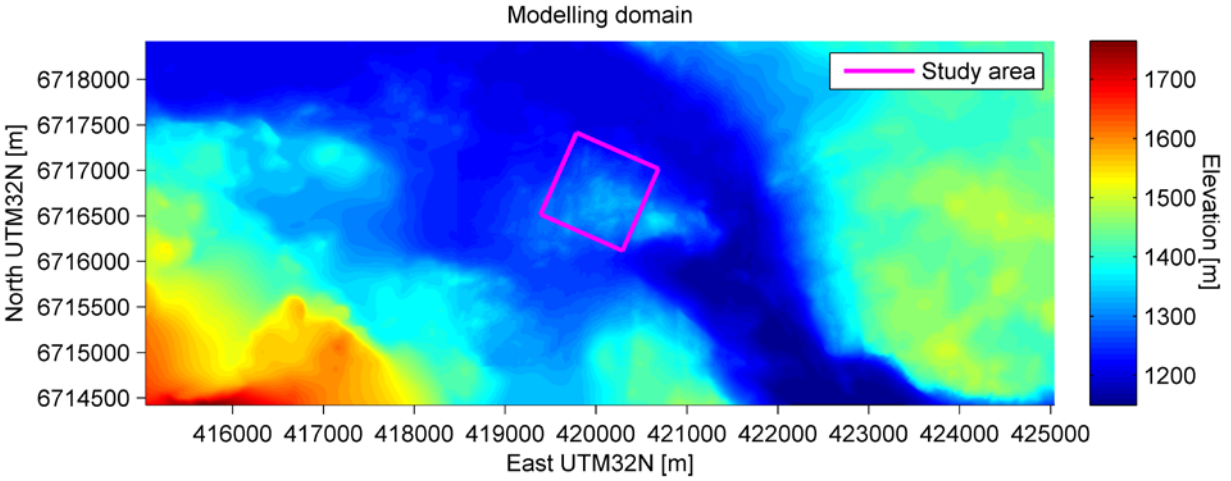

Figure 7 – Entire modelling domain, showing elevation and location of the $1km^2$ study area.

5.2 Parameters

The curvature length scale $\mu\,[m]$ (Equation 13) is used for calculations of terrain curvature, and represents the length over which simplified curvature calculations are performed. Ideally, this parameters should be about half a wavelength of the undulating terrain, and depends on the resolution of the terrain model. The undulation of the terrain in the study area dictates a curvature length of about 100 m.

All other parameters are the default for SnowModel. For a complete list, see (Appendix C).

5.3 Model forcing data

The model forcing data for SnowModel is obtained from the meteorological station Finsevatn operated by the Norwegian Meteorological Institute (met.no) (Figure 2). The station has been in operation since October 1993, and collects hourly observations of temperature, wind direction and speed, humidity and precipitation (met.no, 2012). Model performance relies on

optimal input data, so gaps, errors and biases in the dataset need to be treated. 6 % of station data is missing for the modelling period from October 2011 to May 2013, not counting errors.

A manual and automatic control and correction was performed according to a procedure defined by the hydropower producer Statkraft, as described in the following sections.

As a result of this control and correction, model forcing data is substantially different from the raw data from the Finsevatn meteorological station, and the meteorological input data is therefore hereby named “model forcing data”, to differentiate it from the available raw data from Finsevatn.

5.3.1 Precipitation

Precipitation is notoriously difficult to measure, with large uncertainties arising from wind-induced undercatch and the general instability of accumulated bucket-type precipitation measurement due to evaporation and diurnal fluctuations due to heating (Yang et al., 1996; Liston and Sturm, 2002). Connection loss may also produce time spans without any measurements, as well as values having to be removed due to a manual control exposing bad data. The effect of these errors must be reduced as much as possible.

The precipitation sensor at Finsevatn registers the hourly weight of an accumulating $600\ mm$ precipitation bucket and converts it into a time series of diurnal precipitation in mm. The Norwegian Meteorological Institute does not have an hourly resolution time series available for download outside of their national models, so the hourly time series for use with SnowModel must be created from the accumulated series. The hourly precipitation P is therefore the hourly change (dt) in accumulated precipitation P_{acc}:

$$P = \frac{dP_{acc}}{dt} \qquad \text{Equation 27}$$

This calculation is simple, but the accumulated precipitation series suffers from occasional systematic fluctuations, spikes and gaps, making a direct conversion of raw data impossible. P_{acc} is therefore controlled and corrected using the precipitation correction scheme utilized by the hydro power producer Statkraft. This scheme consists of a control routine that removes unacceptable values, and a correction routine that fills the resulting gaps.

The precipitation control routine checks for absolute limits of precipitation in bucket, at $P_{acc} > 650\ mm$ and $P_{acc} < 8\ mm$. Limits to hourly precipitation state that any values of P_{acc}

are removed if hourly change is not within $-2\,mm < P < 30\,mm$. Notice that the routine accepts negative precipitation. This is due to the daily, temperature induced fluctuations of bucket weight, and are handled by distributing the amount of negative precipitation across the hours of positive. An exception is when the precipitation bucket is emptied: Values are accepted as a manual emptying when $-100\,mm < P < -600\,mm$.

The control scheme will leave gaps in the accumulated series. The accumulating series is, for the most part, a strictly increasing series with the exception of manual emptying of the bucket. As a result, the amount of precipitation over a gap is known, even though the profile of the precipitation event is not. The correction scheme will fill these gaps by inserting a precipitation profile from a regression-weighted average of accumulated precipitation series from nearby stations. The Statkraft-operated meteorological stations at Ossjøen, Geilo and Strengen were used for the regression of both precipitation and temperature.

The systematic error resulting from wind-induced undercatch is corrected by the method of Førland et al. (1996), using a relationship between temperature and wind speed to provide a correction factor for precipitation. The equation states that

$$k = e^{a(T)*v}. \qquad \text{Equation 28}$$

Here, k [1] is the correction factor at any time step, v [ms^{-1}] is corresponding wind speed and $a(T)$ [1] is a factor representing the precipitation type:

$$a(T) = \begin{matrix} 0.0134 & if & T > 1.7\,℃\ (rain) \\ 0.0271 & if & 0 < T \leq 1.7\,℃\ (mixed) \\ 0.0486 & if & -5 < T \leq 0\,℃\ (snow) \\ 0.0820 & if & T \leq -5\,℃\ (snow) \end{matrix} \qquad \text{Equation 29}$$

As an example from Finse, a high wind snowfall may experience wind speeds of $12\,m/s$ at temperatures of -15 ℃. From Equation 28 and Equation 29 this gives a correction factor of

$$k = e^{0.0820*15\,m/s} = 3.4212 \qquad \text{Equation 30}$$

As a result, the model input precipitation is substantially higher than the raw observed precipitation data from Finsevatn. For the model time periods, the total precipitation is increased with a factor of 1.54 and 1.63 for the 2011-2012 and 2012-2013 seasons, respectively (Figure 8). The same precipitation correction is used by Bruland et al. (2004) in a similar study on SnowModel.

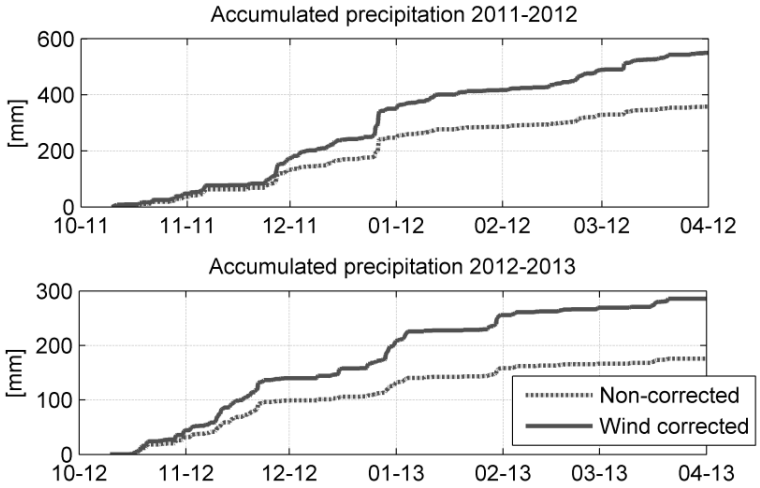

Figure 8 – Accumulated precipitation for both wind corrected and non-corrected data.

5.3.2 Wind speed and direction

Wind series are prone to errors in the form of frozen speed and direction sensors, and erratic, nonsensical values observed during manual correction. Any gaps in the wind series were filled with the median wind speed 4.80 $m\ s^{-1}$ from Finsevatn station. The spatial variation in wind results in difficult conditions for interpolation between weather stations over large distances, so a simple median was used for long gaps. Short gaps in the series (up to 4 hours) are filled using a linear interpolation. The wind series used for the precipitation correction in Equation 28 was filled with the median wind at precipitation events, which is generally higher than the regular median wind (Liston et al., 2007). The median wind at precipitation events was found to be 5.50 $m\ s^{-1}$.

5.3.3 Temperature and humidity

Gaps in the temperature series were filled with interpolated data from the nearby Statkraft-operated meteorological stations at Ossjøen, Geilo and Strengen. Small gaps of up to 4 hours in length are linearized. The gaps in the humidity series were linearized, regardless of gap length.

6 Validation data

6.1 Meteorological data

6.1.1 Wind speed and direction

All the collected wind speed data from the stations are displayed in Figure 9. On December 11th 2012, the study area experienced humid weather with an abrupt shift to cold weather and gentle winds, resulting in wind speed and direction sensors freezing solid. This event is visible in all the plots in Figure 9 as the time span where A and C have no data, and Station B shows very low wind speeds. The wind direction sensor also froze in this time period. Station A suffered damage from this event, and the wind speed sensor has been out of order since then. With the exception of this event, the stations have performed well with few freeze events and errors.

The collected wind data shows a high degree of topographic variability, with wind direction and wind speed being altered by the local terrain (Figure 10). As expected, the wind direction is predominantly bi-directional, due to the strong channelling effect of the valley. 75 % of model forcing data occurs along a east-west axis. The validation data from Stations A, B and C show a trend towards a north-south axis. The westernmost A has the least axis shift, while the eastern Station C shows a general axis shift of $+40°$ when compared with the model forcing data. Station C has the highest observed wind speeds of all stations, owing to its exposed location.

The wind speed distribution shows that the sheltered location of Stations A and B give an intuitive skew towards low velocities, and the exposed location of Station C yields a velocity distribution closely resembling the raw model forcing data at $10\ m$ height.

Figure 11 shows the difference in wind speed between Station A and Station B, categorized in different wind directions. The topographic effects are apparent when viewing Figure 6 and comparing the wind speeds of Station A and B for different wind directions. When the wind direction is from the south-east, Station B has higher wind speeds relative to Station A, while the opposite is in effect when the wind speed is from the north-west. It is worth noting that this analysis does not cover a lot of data points, due to the erroneous sensor at Station A, resulting in a short overlapping time period of data.

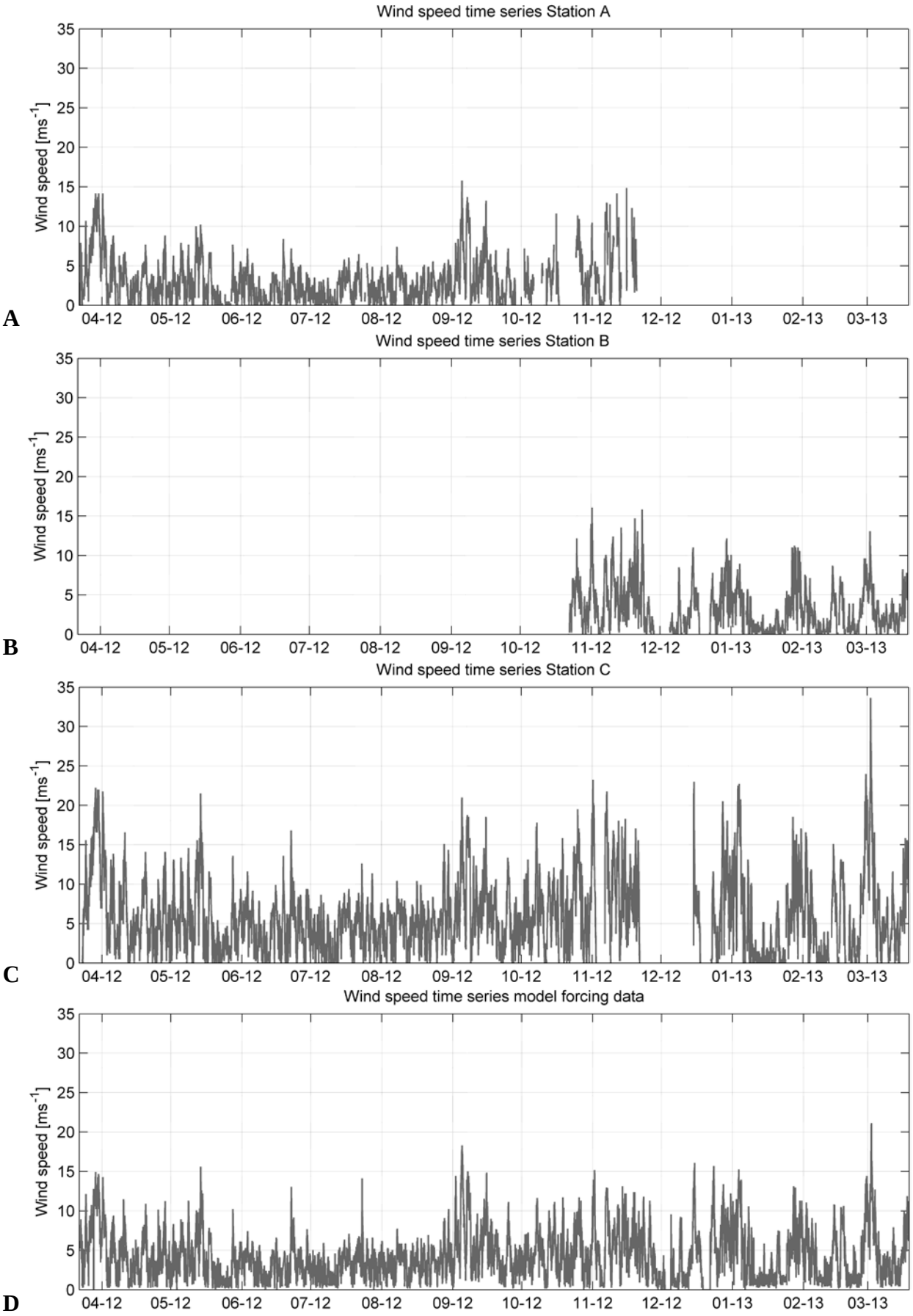

Figure 9 – Illustration showing wind speed data. Plots are Stations A, B and C, with the model input data as D. All data is scaled to a uniform height of 2 m.

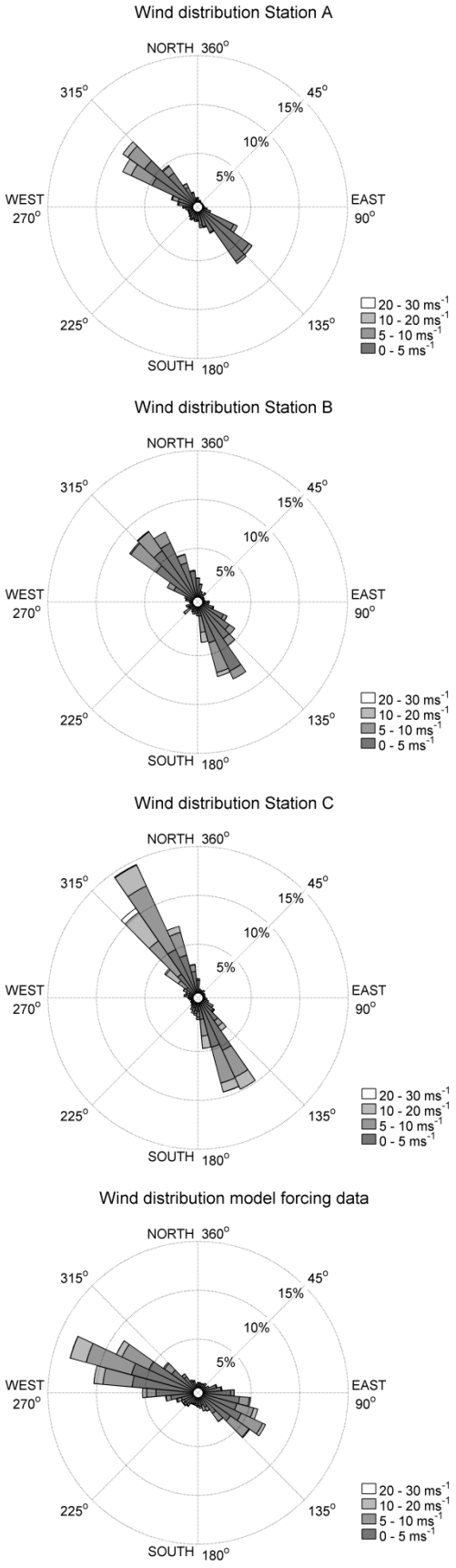

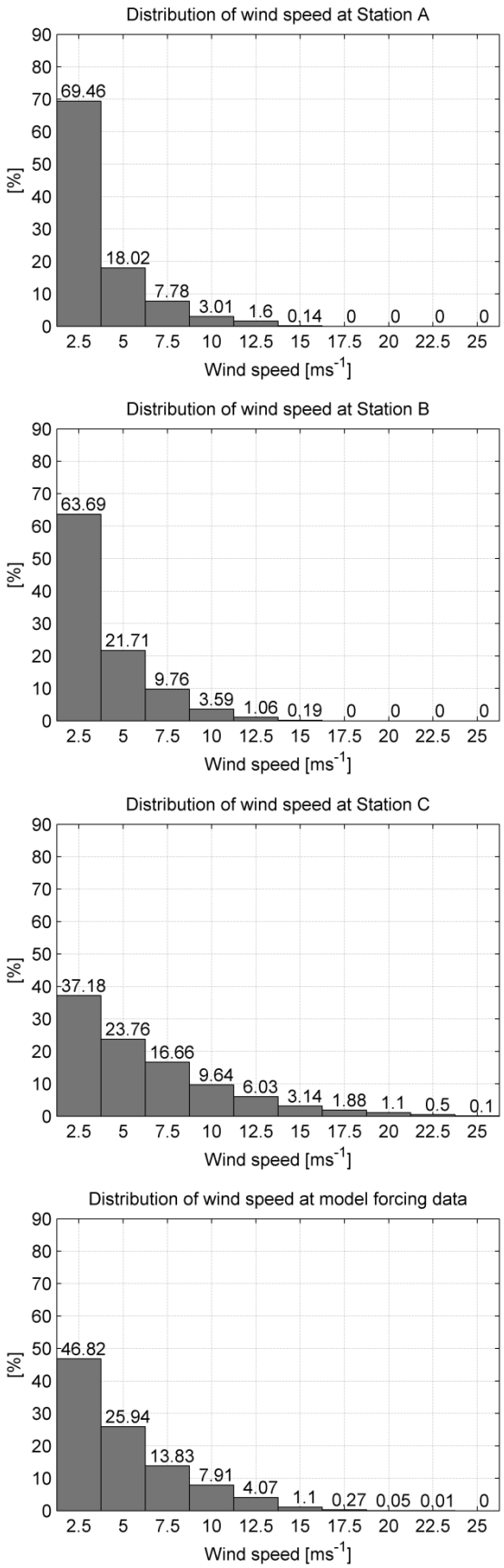

Figure 10 – Wind distributions for all observed data between 22nd of March 2012 until 19th of March 2013. Plots from the top down show Stations A, B, C, along with the model forcing data (bottom). All wind speeds are scaled to 2 m above ground.

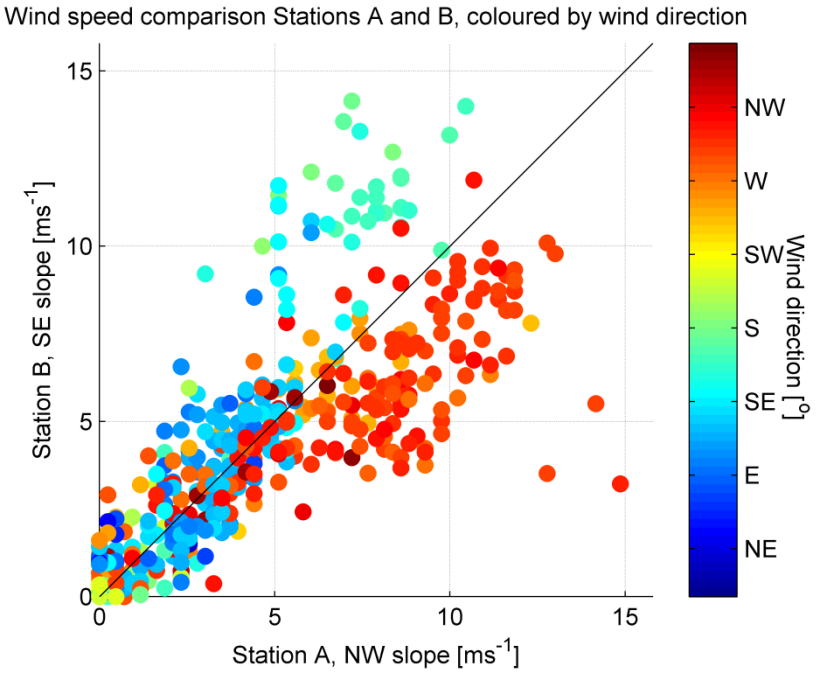

Figure 11 – Scatter plot showing differences in wind speed covariation between Station A and Station B. Data points are colour coded for wind direction. The solid line shows a 1: 1 relationship.

6.1.2 Temperature

Temperature data is not prone to the same equipment errors and freeze events as wind speed sensors, as there are no moving parts. The temperature series are complete, with no erratic values or faulty sensors.

Table 3 shows the variation in maximum and minimum temperatures, and we see that all stations register temperatures in approximately the same range. The model forcing data has a substantially lower minimum temperature, even though the station is located lower in the terrain and would intuitively have experienced higher temperatures. In Figure 12 and Figure 13 we see the evolution of temperature through 10 days at the end of February 2013 and May 2012. The three validation stations correspond well with each other, while the model forcing data has some sharp drops in observed temperature. Both of these time spans have an observed wind speeds below $3\,m\,s^{-1}$, and this effect is correlated with wind speed (Figure 14). In this scatter plot, we see that all cold temperatures for the model forcing data occur at low wind speeds. For higher wind speeds, the model forcing temperature is on average 1.34 ℃ warmer than Station C, which is reasonable given that Station C is located $126\,m$ higher up in the terrain. For gentle winds, the model forcing data is as much as 15 ℃ colder

than Station A, even though Station A is located only 84 m higher up and 2 km south east of the Finsevatn station.

In Figure 12 we also see that Station C (red) seems to experience some spikes in daytime temperatures compared to Station A and B. This is most likely due to the exposed location of C, and the fact that the ground is often bare of snow due to high wind speeds , which then absorbs a lot of short wave radiation during clear sky events.

Table 3 – Maximum and minimum temperatures for stations between March 22nd 2012 and March 19th 2013. *Station B has only been in operation since October 2012.

Station	Minimum temperature	Maximum temperature	Elevation
Station A	−21.9 ℃	18.4 ℃	1294 m
Station B*	−22.0 ℃	4.2 ℃	1300 m
Station C	−21.1 ℃	17.7 ℃	1336 m
Model forcing data	−30.5 ℃	18.6 ℃	1210 m

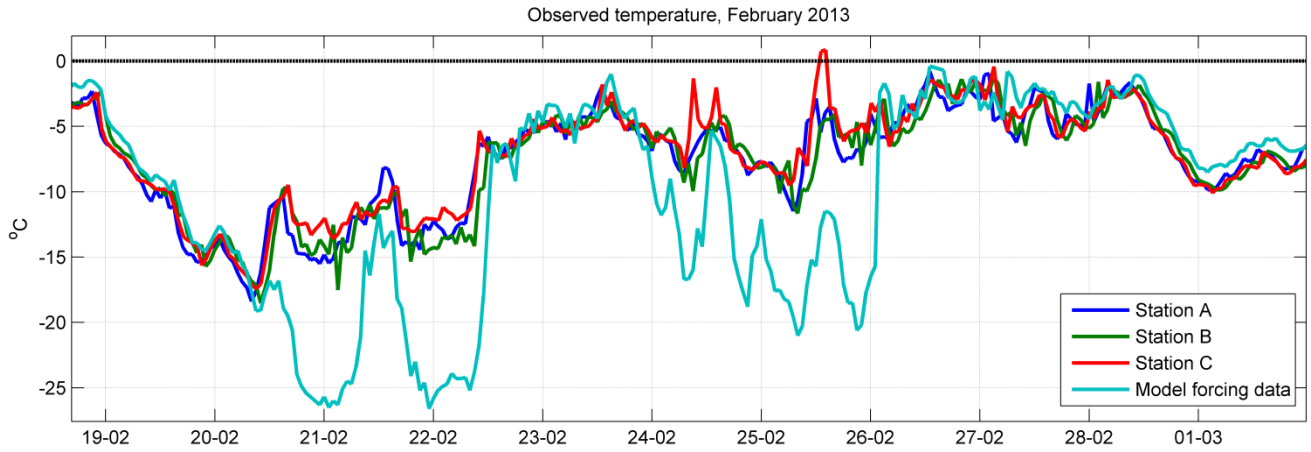

Figure 12 – Temperature data from the end of February 2013. Plot shows data from Stations A, B and C along with the model forcing data. This type of event is the winter inversion in Figure 14.

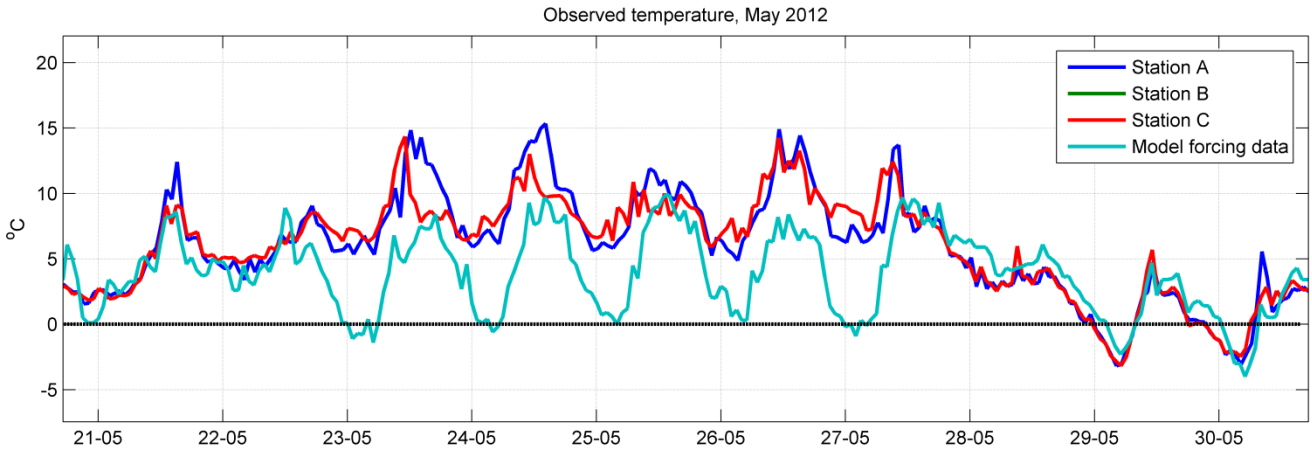

Figure 13 – Temperature data from the end of May 2013. Plot shows data from Stations A and C along with the model forcing data. Station B was not in operation during this time span. This type of event is the spring inversions in Figure 14.

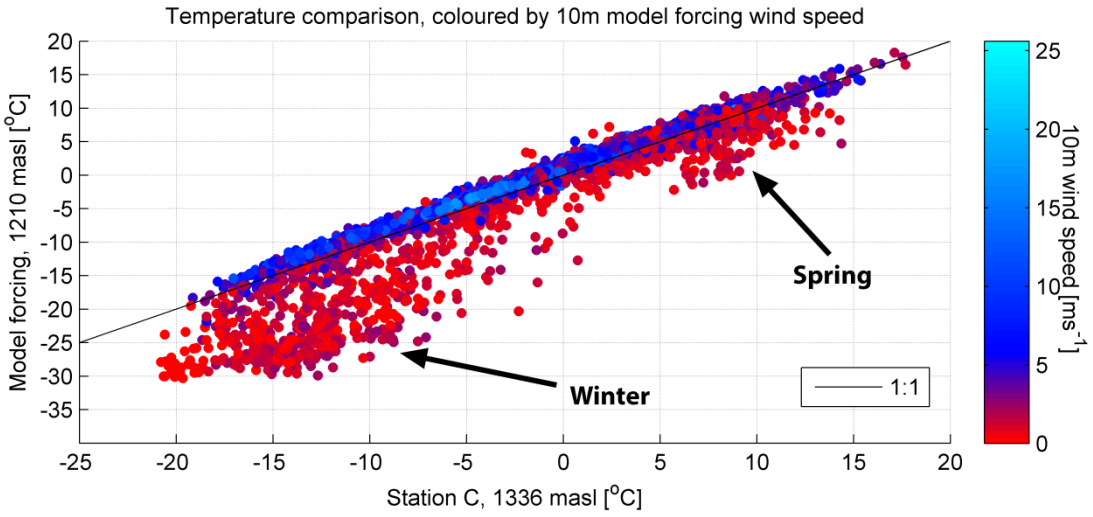

Figure 14 – Scatter plot showing the relationship between temperatures at Station C and the model forcing data. Colour coded for 10 m wind speed.

6.2 GPR data

Field work for GPR and snow surveys were performed once a month through the winter months of December, January, February and March during the winters of 2011-2012 and 2012-2013. These expeditions involved 4 days of GPR tracking of the entire study area by snowmobile along the tracks displayed in Figure 2. The GPR grids are on two scales: A larger grid with $250\ m$ grid spacing and a smaller grid with $50\ m$ grid spacing to better capture the topographic variability.

6.2.1 Snow pit surveys

Representative bulk snow density is used to convert GPR signal time recordings to actual snow depths. Table 4 shows an example of a monthly set of density measurements. Table 5 shows the bulk densities for each month in both seasons. Due to time and weather constraints, the completeness of each monthly set varies. No density measurements were available for February 2012, so for GPR velocity calculations the density for January 2012 was used. Appendix D contains the complete data on snow density measurements.

6.2.2 GPR snow depth observations

The recorded GPR return signals were converted to distances by manually tracing the highest amplitude return signal from the snow-ground interface. To more easily detect the highest amplitude, several filters were used to improve the contrast of the signal and remove noise. Figure 15 shows an example of data processing. Note the horizontal return signals between traces 1350 and 1490. With the trace time being $0.25\ s$, this indicates a standstill of the snowmobile lasting $35\ s$. Stops of this length were done regularly to check if the equipment was functioning properly, to plan a route for the snowmobile in difficult snow conditions, and to do snow depth calibration measurements.

Table 4 – Snow pit data and radar signal velocity from Finse, February 25th 2013. Full density data sets presented in Appendix A. The average density is calculated as the weighted average of the depth of each profile, and the velocity was calculated using Equation 35 and Equation 36.

Tube length:	20.00 cm			
Tube volume:	500.00 cm^3	Average density [g/cm^3]:		0.33
Bag weight:	30.00 g	Average speed acc. to Kovacs (1995) [mns^{-1}]:		0.23
Station A	Profile 1			
Start depth [cm]	Stop depth [cm]	Column length [cm]	Weight w/o bag [g]	Density [gcm^{-3}]
97.00	77.00	20.00	175.00	0.35
77.00	57.00	20.00	170.00	0.34
57.00	37.00	20.00	170.00	0.34
37.00	17.00	20.00	185.00	0.37
17.00	0.00	17.00	185.00	0.44
			Aver. density [$g\ cm^{-3}$]:	0.36
Station A	Profile 2			
99.00	79.00	20.00	175.00	0.35
79.00	59.00	20.00	170.00	0.34
59.00	39.00	20.00	170.00	0.34
39.00	19.00	20.00	185.00	0.37
19.00	0.00	19.00	185.00	0.39
			Aver. density [$g\ cm^{-3}$]:	0.36
Station B	Profile 1			
97.00	77.00	20.00	130.00	0.26
77.00	57.00	20.00	155.00	0.31
57.00	37.00	20.00	200.00	0.40
37.00	17.00	20.00	190.00	0.38
17.00	0.00	17.00	120.00	0.28
			Aver. density [$g\ cm^{-3}$]:	0.33
Station B	Profile 2			
99.00	79.00	20.00	130.00	0.26
79.00	59.00	20.00	145.00	0.29
59.00	39.00	20.00	145.00	0.29
39.00	19.00	20.00	145.00	0.29
19.00	0.00	19.00	145.00	0.31
			Aver. density [$g\ cm^{-3}$]:	0.29

The deepest snow drifts usually give a fuzzy return signal which is hard to trace. Section 0 contains a discussion and comparison of GPR depth and manual snow probe measurements that shows that manually processed GPR data generally tends to underestimate the deepest snow catches. Tracing the deepest snow depths is therefore done in spite of their relatively unclear signal returns. Figure 15.C shows an example of deep, diffuse return signals at trace number 2050. The signal times were then convert to snow depth by using the according to Kovacs et al. (1995) using the snow densities from Table 5.

Table 5 – Bulk snow densities for each GPR set. All values in gcm^{-3}. Note the missing density from February 2012 due to complications during field work.

Year	December	January	February	March
2011-2012	0.31	0.38	–	0.45
2012-2013	0.34	0.31	0.33	0.34

Figure 15 displays all the monthly sets of GPR measurements. The total length of GPR tracks across all expeditions is 114 km. With 250 000 point measurements, this yields an average point density of about 0.5 m for the entire dataset.

The terrain and snow conditions at any given excursion defined where it was possible to drive the snowmobile. The rough topography's ever changing snow drifts made exact planning of tracks impossible. The observed GPR tracks will therefore differ from those planned in Figure 2. The resulting representativeness of the tracks is calculated from the actual tracks, and not the planned tracks. Also, some sets are incomplete due to errors from equipment failure and difficult conditions:

In most field trips there were issues with GPS battery lifetime. Another issue turned out to be positioning of the GPS on the GPR sled. When mounted vertically, the GPS would turn off if it experienced any sharp movement (i.e. bumping across protrusions of hard snow). The lack of positioning made the data impossible to relate to any other observations. The affected data was removed from further analysis.

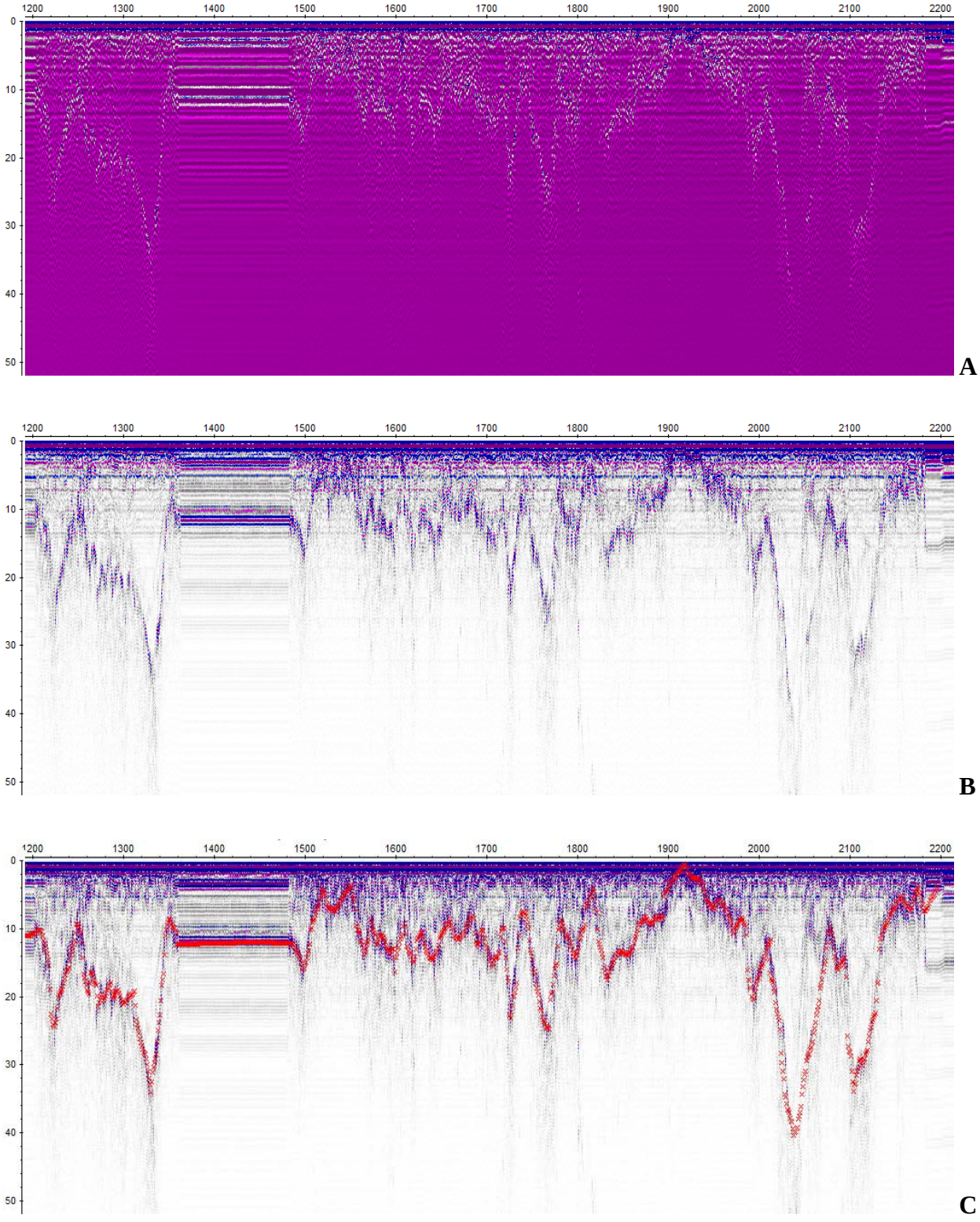

Figure 15 – Example of processing GPR signals. Radar waves are shown with varying amplitude (colour) at different return times in nanoseconds $[ns]$ (y-axis). x-axis is the trace number, each number indicating a registered return signal, driving from left to right. (A) contains the raw data, (B) is the same data after a bandpass-filter, and (C) has the added manual tracing of ground return signal. Data is an excerpt from the GPR survey on the 25th of February 2013.

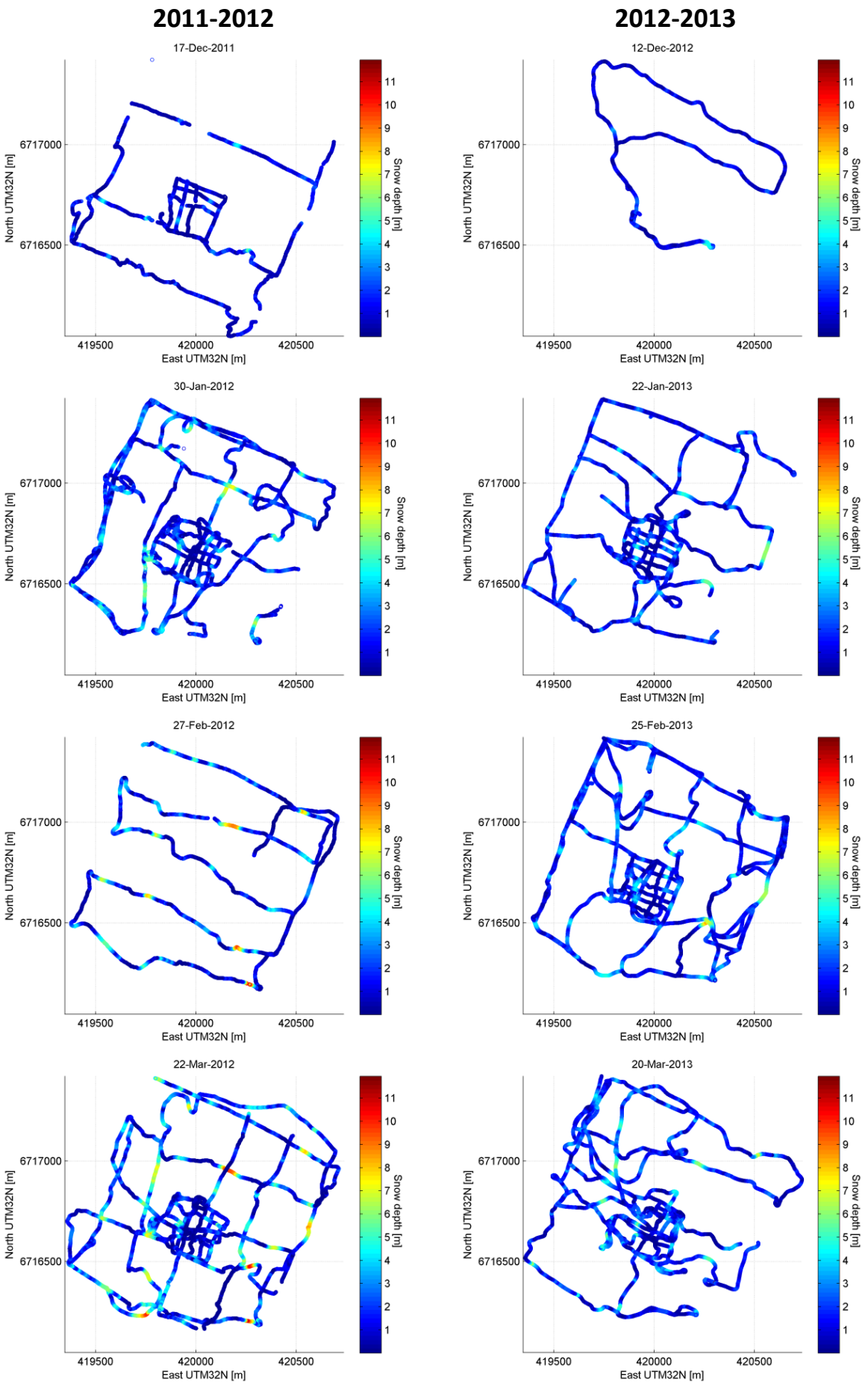

Figure 16 – GPR snow depth. Months are December, January, February and March from the top down.

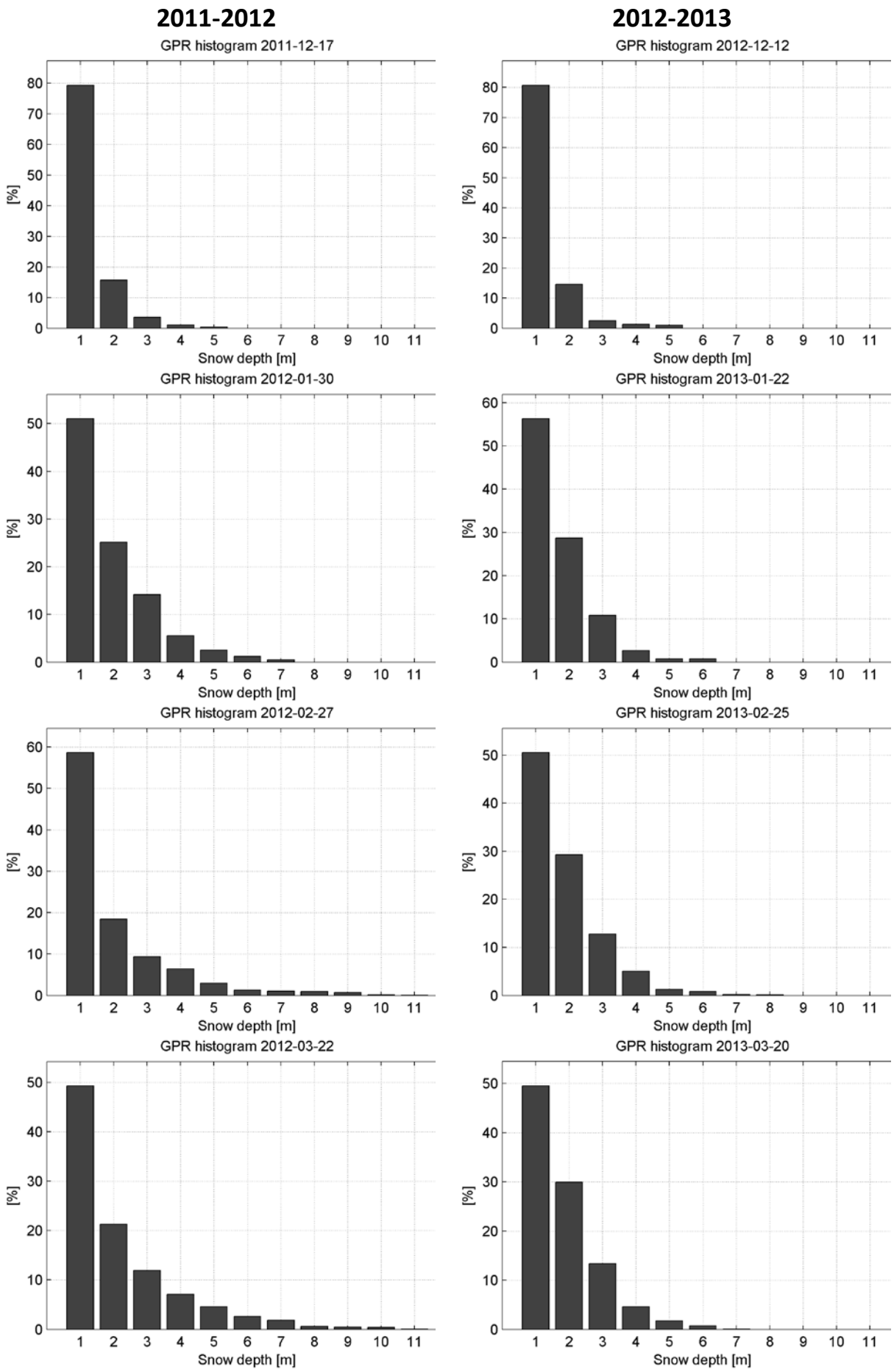

Figure 17 – Histograms of GPR data. Months are December, January, February and March from the top down.

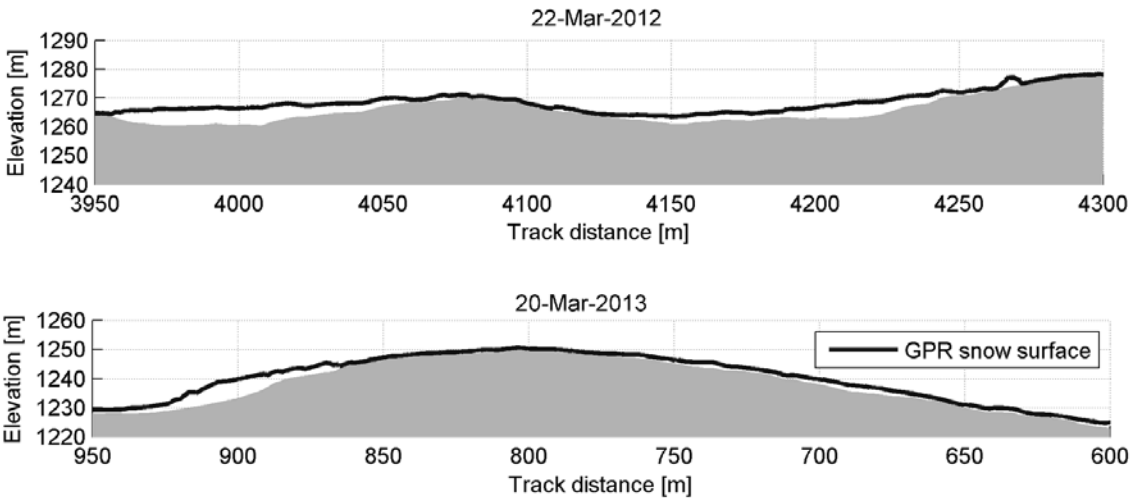

Figure 18 – GPR snow depths accumulations on lee-sides of slopes. Examples from March 22nd 2012 and March 20th 2013.

In December 2011 the municipality of Ulvik did not give us permission to utilize the snowmobile. To still have measurements from this month, the GPR equipment was pulled through the terrain manually by skiing. This was a very hard physical effort, and the rough terrain made it impossible to do measurements of the entire study area.

February 2012 saw an unfortunate accident with the snowmobile, and the excursion had to be aborted before GPR data collection was completed.

In December 2012 snow conditions were very difficult, with over 1 m of powder snow. The snowmobile couldn't traverse even the slightest slope without getting stuck, and the resulting data from this month is what was possible to collect in those conditions.

With these exceptions the datasets are complete. Figure 17 shows histograms of snow depth variation in GPR data. Snow depth variation increases through the season, with 2011-2012 experiencing more snow and a higher variation than 2012-2013. Snow depth observations follow the terrain in the manner one would expect, with the largest accumulations of snow occurring on the lee sides of the prevailing wind direction (Figure 18).

7 Model results

The following model results are from SnowModel with default parameters, and input data and constraints as described in Chapter 5. Model output is compared with the collected validation data. Comparisons of modelled and observed wind speed, wind direction, snow distribution and accumulated seasonal SWE will be presented, in that order. A thorough evaluation of these results will take place in Chapter 8.

7.1 Modelled wind speed

Figure 19 shows a time series of observed and modelled wind speed over 3 days in October 2012, a representative time span for the data sets. The plot shows that the modelled wind speed for Station A and B is higher than the corresponding observed data, while for Station C, the modelled data is closer to the observed. The median ratios of modelled over observed velocities are 1.60, 1.75 and 1.03 for each station respectively, indicating a general overestimation.

Figure 20 shows the corresponding wind speed distribution in the terrain on October 25th 2012, at 14:00. The wind speed varies intuitively with the terrain, but seems to be unable to recreate the larger eddies that might produce the lower wind speeds observed at Stations A and B. For the relationship with topography, see Figure 6.

Figure 21 shows the relationship between observed and modelled wind speed at the 3 meteorological stations (1, 3 and 5), along with the relationship between the model forcing data and the modelled data for each station (2, 4 and 6). The upward shift in Figure 21.1 and 3 strengthens the claim of overestimated wind speeds. Station A has the closest covariation with the model forcing data with $R^2 = 0.83$, maybe owing to its closer proximity to the model forcing station. Station C (Figure 21.5) shows winds of the same scale for both model forcing and observed, but with a slightly lower R^2. For the model to be able to recreate the wind speeds at each station there needs to be a substantial alteration of the wind speed in the models interpolation. As we can see from Figure 21.2, 4 and 6 there is only a small difference between model forcing and modelled data for the locations of Station A and B. From Figure 11 it is known that the wind speeds need to be significantly altered by wind direction to recreate the local wind field. As interpolated and model forcing data is almost the same for all locations, the model is apparently not able to create the same degree of variation.

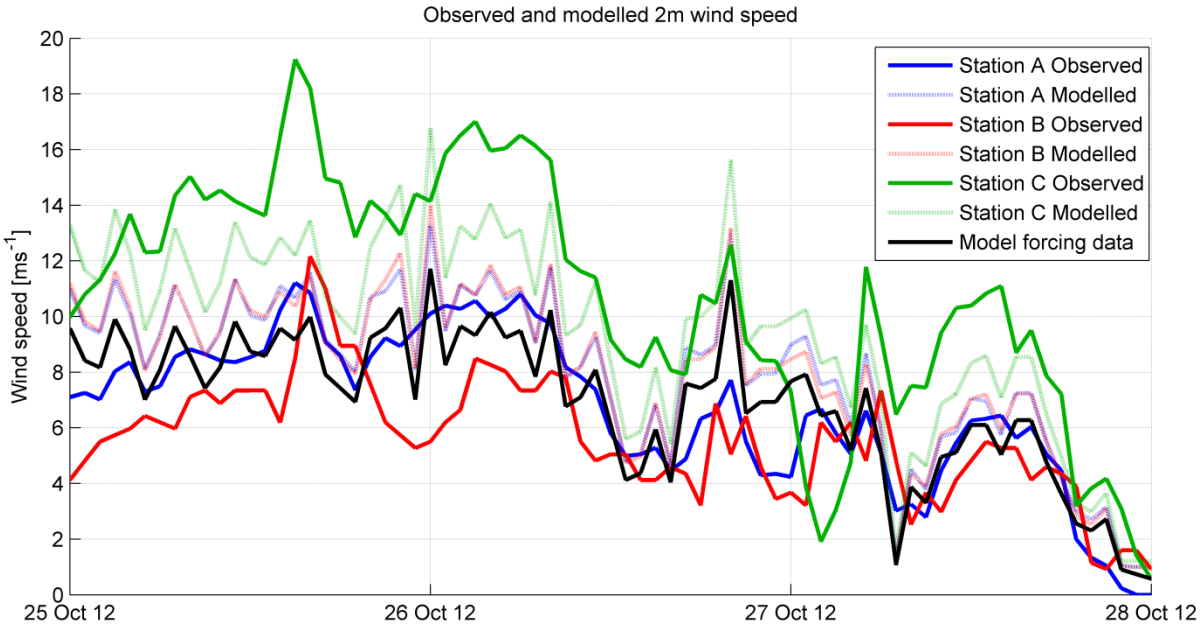

Figure 19 – Observed and modelled wind speed from October 25th 2012 till October 28th 2012.

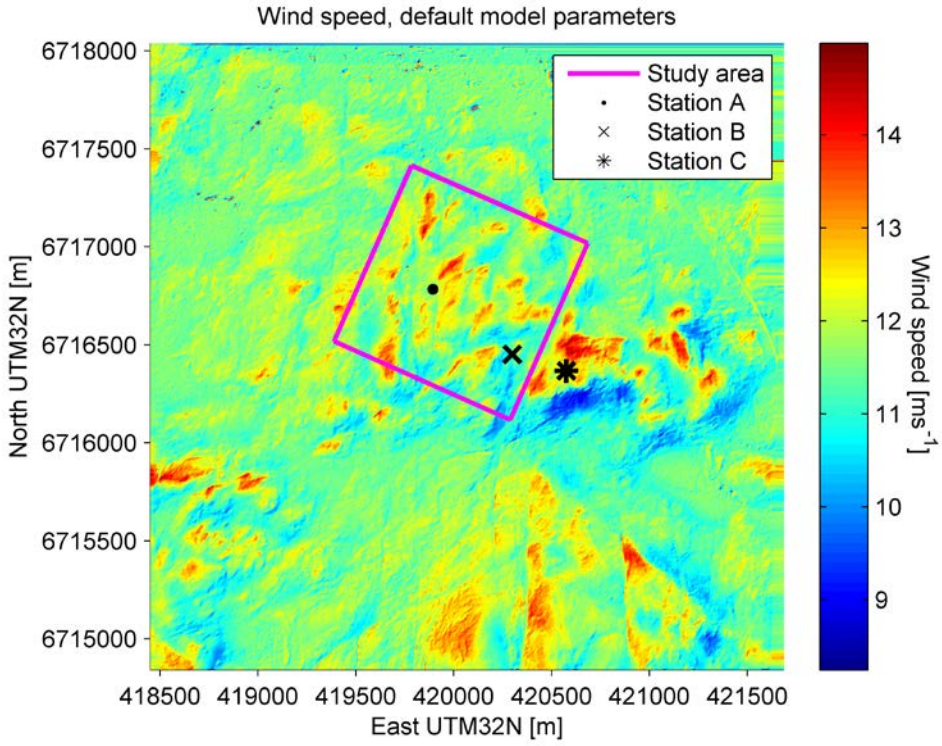

Figure 20 – Wind speed distribution on October 25th 2012.

7.2 Modelled wind direction

Figure 22 compares the validation data and the model forcing data with the model results for each station's location. Wind direction in the plots is categorized according to wind speed, as weak winds $< 3\ m\ s^{-1}$ tend to have a more erratic wind direction. This is reflected in the much higher R^2 between modelled and observed wind direction for all stations. Figure 22.2, 4 and 6 show that the model forcing data and the model output is practically identical. Since the model interpolation is practically identical to the model forcing data, the variation comparison in Figure 22.1, 3 and 5 is therefore the same as a comparison between the observed station data and the model forcing data.

7.3 Modelled temperature

Figure 23 shows comparisons of temperature data. As expected, the recognizable pattern of temperature inversion appears in Figure 23.1, 3 and 5. This reflects the phenomenon in the model forcing data seen in Figure 14. In Figure 23.2, 4 and 6 it is evident that there is a linear relationship between the model forcing data and the model output owing to the simple temperature elevation lapse rates used when SnowModel interpolates temperature from a single station.

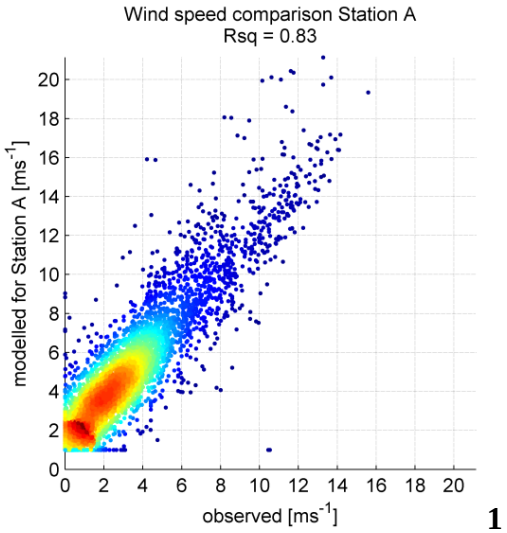

1

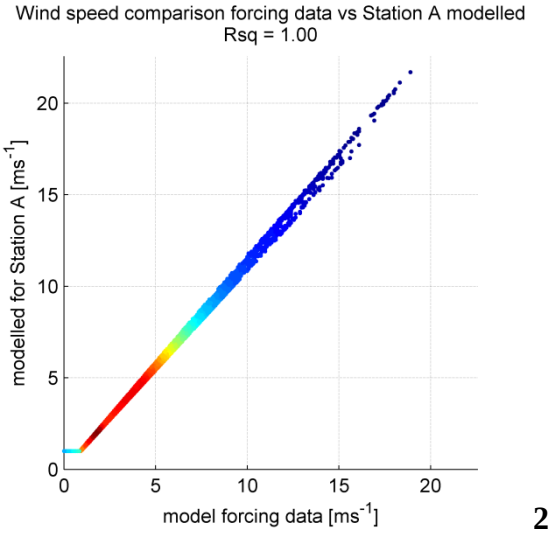

2

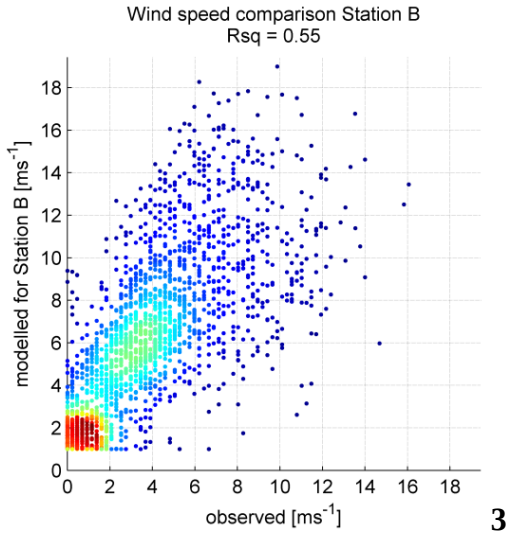

3

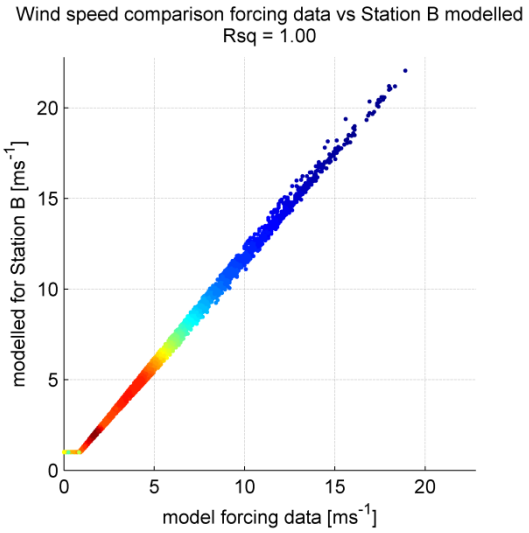

4

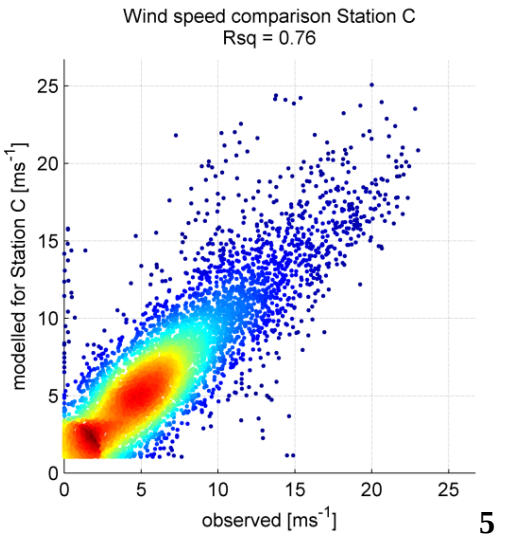

5

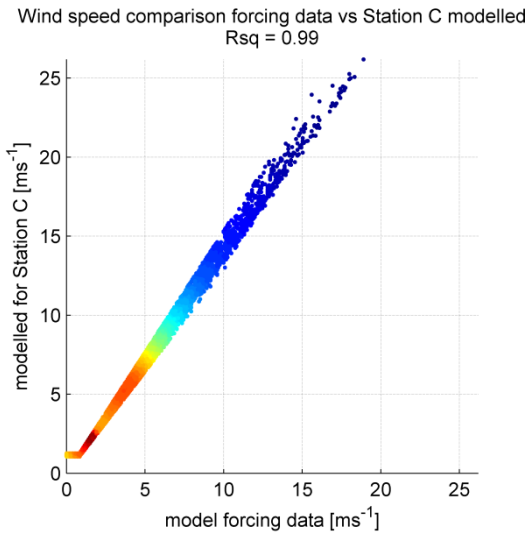

6

Figure 21 – Observed wind speed versus modelled data (1, 3, 5) and model forcing data versus modelled (2, 4, 6). Plots are colour coded for point density to clearly see the distributions.

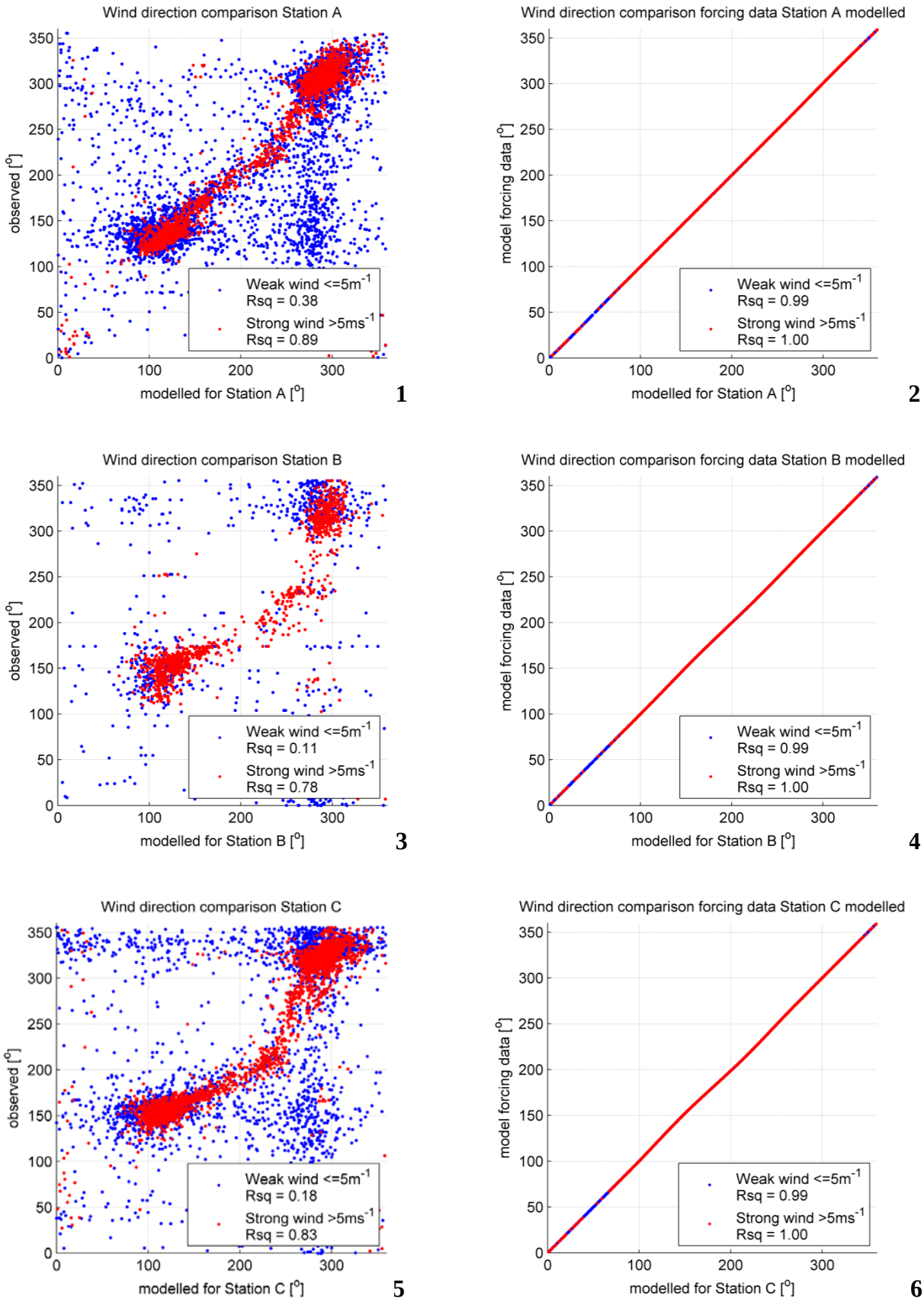

Figure 22 – Observed wind direction versus modelled data (1, 3, 5) and model forcing data versus modelled (2, 4, 6). Plots are colour coded for point density to clearly see the distributions.

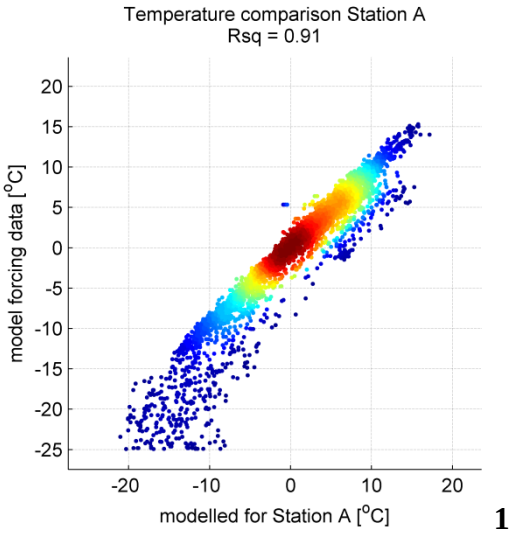

1

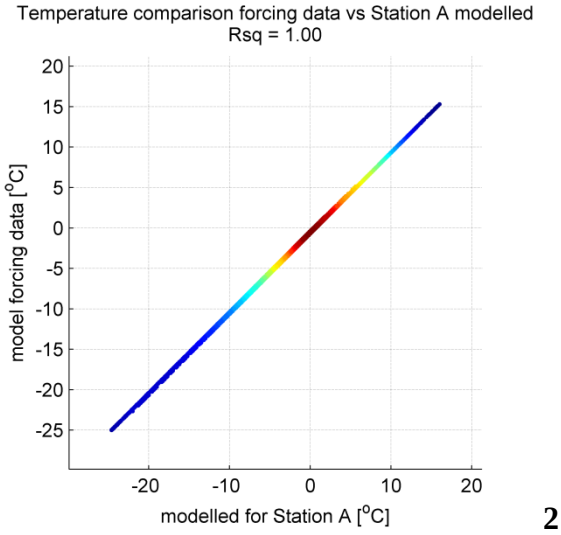

2

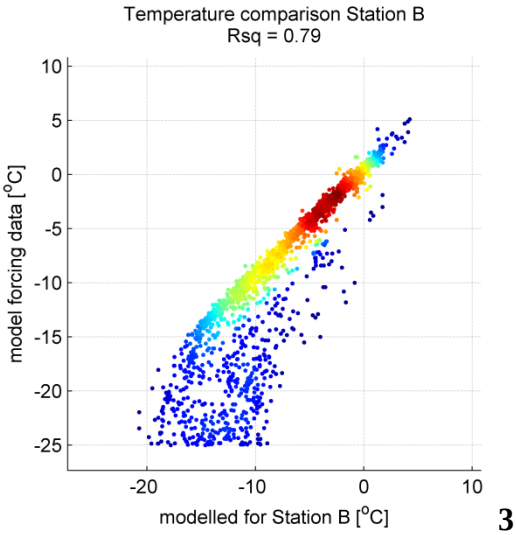

3

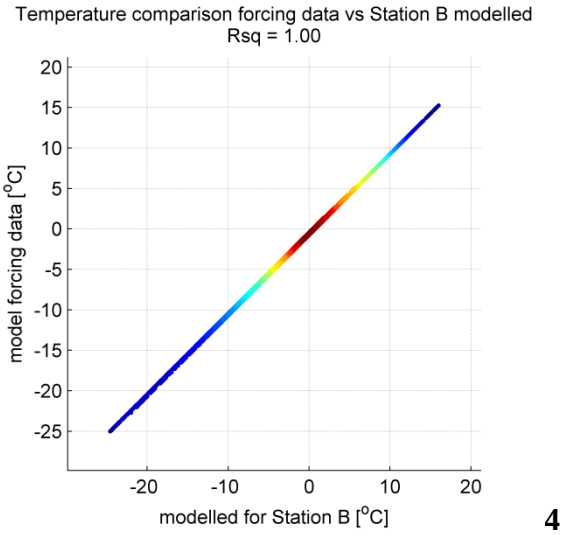

4

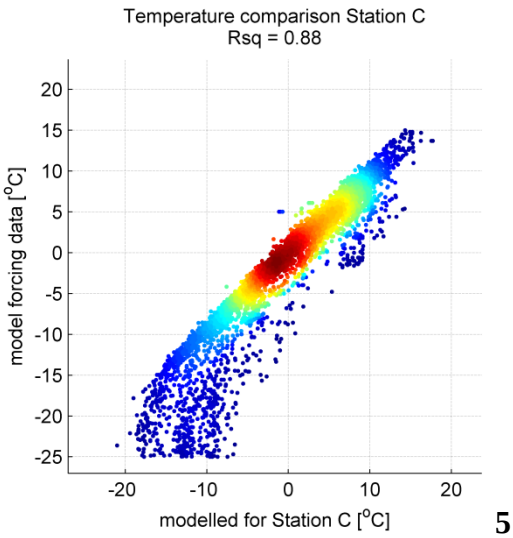

5

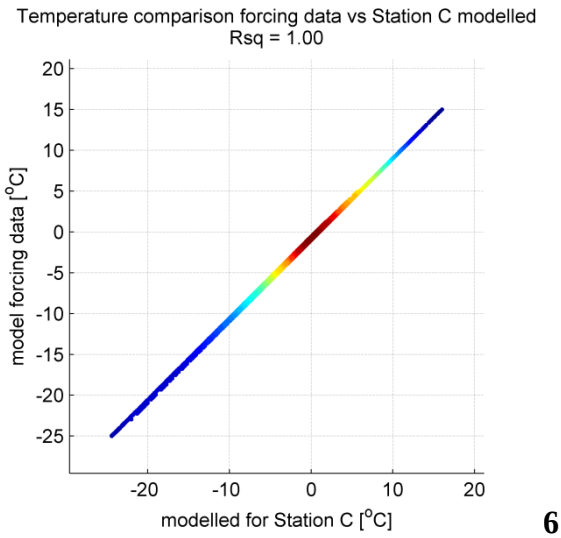

6

Figure 23 – Observed temperature versus modelled data (1, 3, 5) and model forcing data versus modelled (2, 4, 8). Plots are colour coded for point density to clearly see the distributions.

7.4 Snow cover

The model may be able to recreate distribution patterns but at the same time incorrectly estimate the average SWE, or vice versa. The analysis of snow data from SnowModel is therefore divided into two sets: (1) A comparison of snow distributions; and (2) a comparison of estimated average SWE depth in the study area.

Figure 24 shows the modelled snow distributions from March 2012 and March 2013, along with a point-for-point comparison with GPR and histograms for both datasets. With an $R^2 \approx 0$, there seems to be no covariation between the observed and modelled snow distributions. Figure 25 shows the GPR track of March 2013 overlaid the modelled snow distribution for the same date. The comparison shows that the accumulations of snow in SnowModel are located in the same approximate locations as several of the accumulations in the GPR, but the GPR observes generally deeper snow depths over all. The model does not seem to accumulate snow in flat terrain, and any prominent snow drifts are limited to areas in immediate proximity of steep slopes.

Figure 26 shows a plot of average, accumulated SWE for the entire winter season. Included are 4 datasets: (1) SnowModel with no snow transport (SnowTran-3D turned off); (2) accumulated precipitation for the entire plot time span; (3) estimated SWE from GPR datasets; and (4) data from the Norwegian Meteorological Institutes national $2\,km$ snow model SeNorge (seNorge.no, 2013). SWE depth from GPR data is calculated using a spatially averaged snow depth and the snow density corresponding to the GPR date. The spatial averaging consists of rescaling the point-based GPR data to $4\,m$ grid (equivalent to the model output).

The results show a systematic lack of snow in the model results, and no apparent relationship between precipitation and snow accumulation despite constant freezing temperatures during the winter. Any temporary increase in SWE depth late season seems to be removed at the same rate it is introduced. As the model without snow transport experiences 2.5 times the amount of accumulated SWE, it is apparent that the snow transport routine removes a substantial amount of snow from the modelling domain.

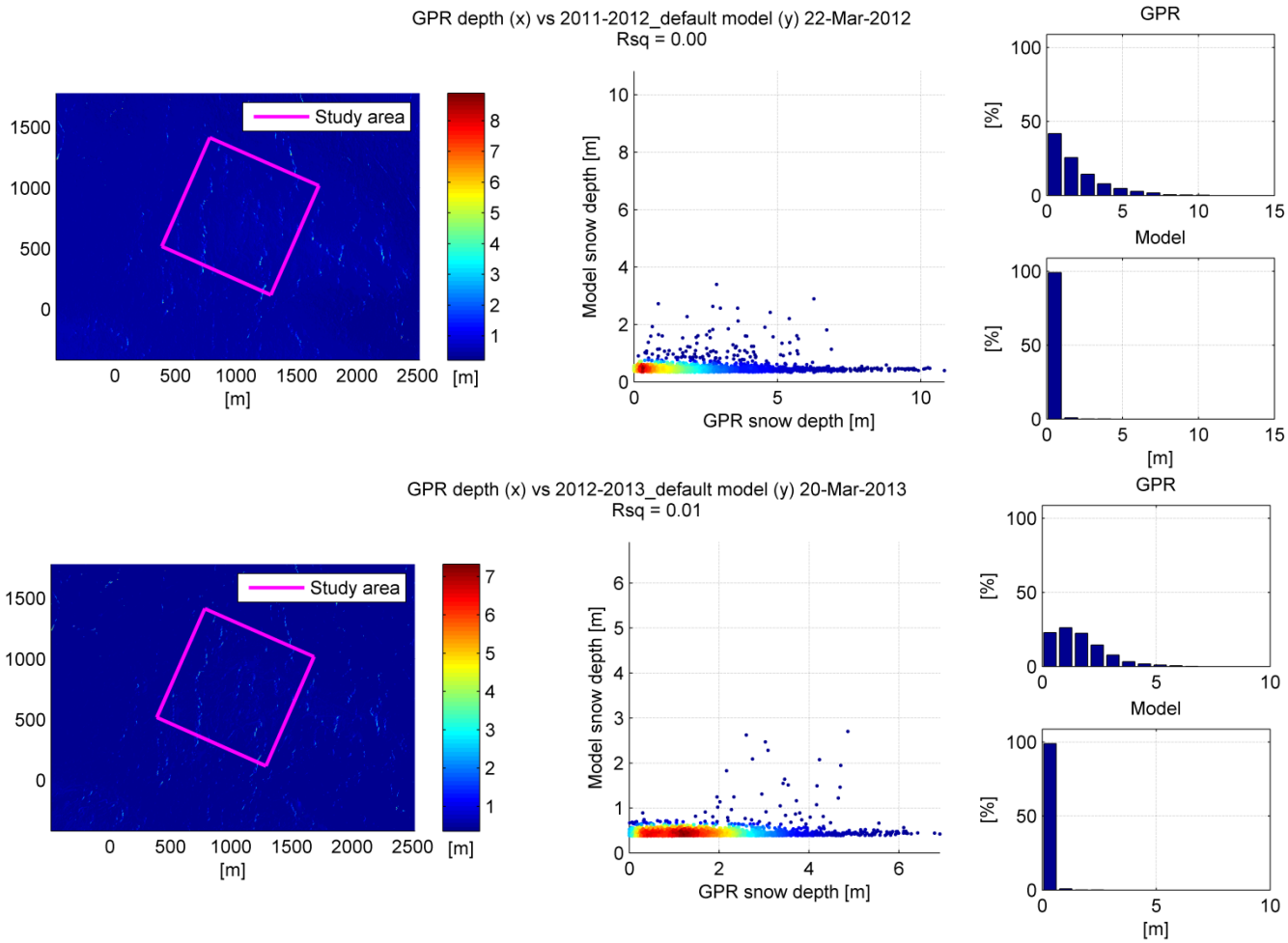

Figure 24 – Results of modelling the seasons of 2011-2012 and 2012-2013 with default model parameters. Left figure shows modeled snow surface, colour coded for snow depth. Scatter plot shows the co-variation of observed and modelled snow depth, colour coded for scatter point density. Right plots are histograms showing the variation in snow depth in the GPR and modelled datasets for March 2012 and 2013.

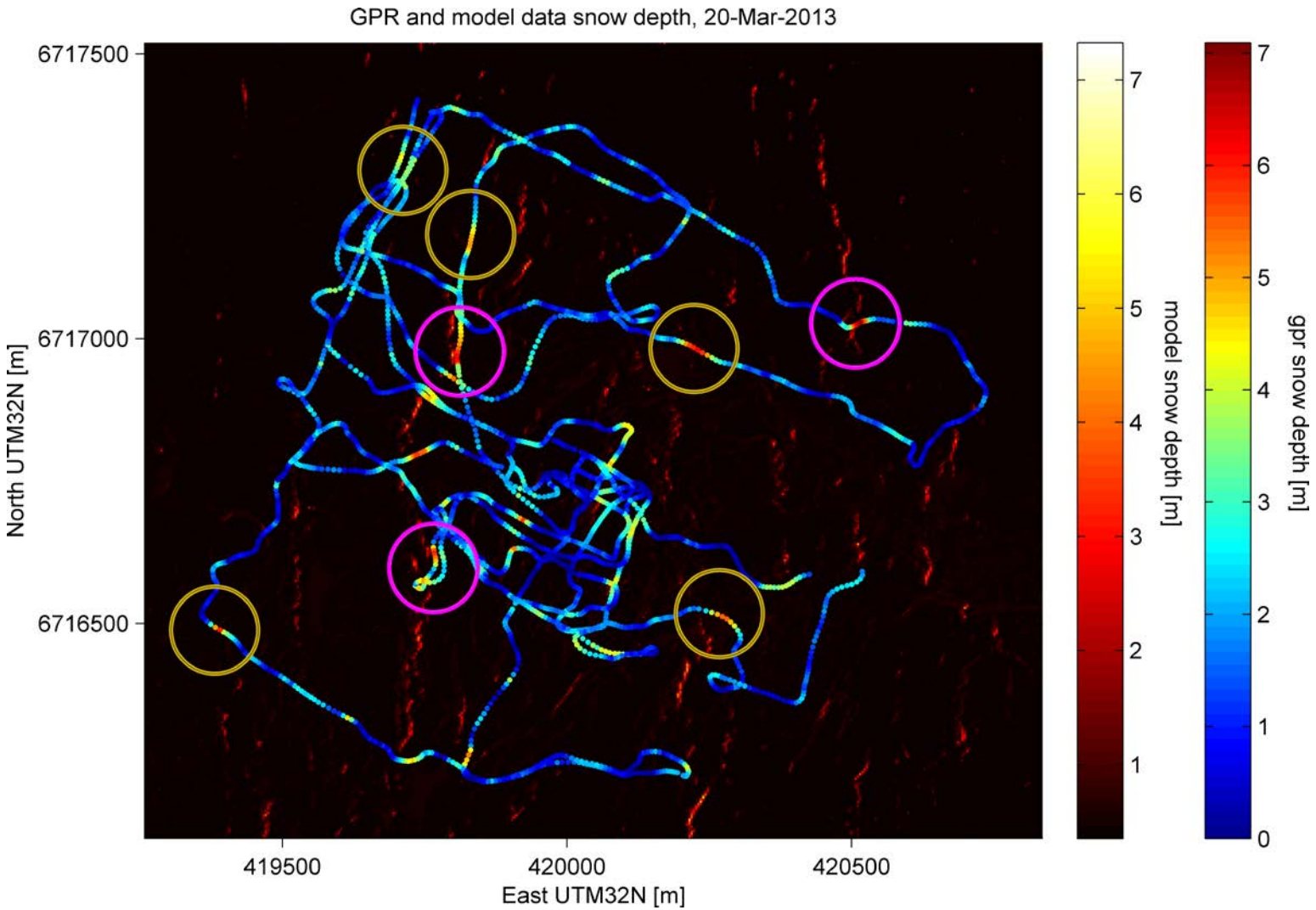

Figure 25 – GPR data overlaid modelled snow depth for default SnowModel. Purple and yellow circles mark examples were accumulations match and don't match, respectively.

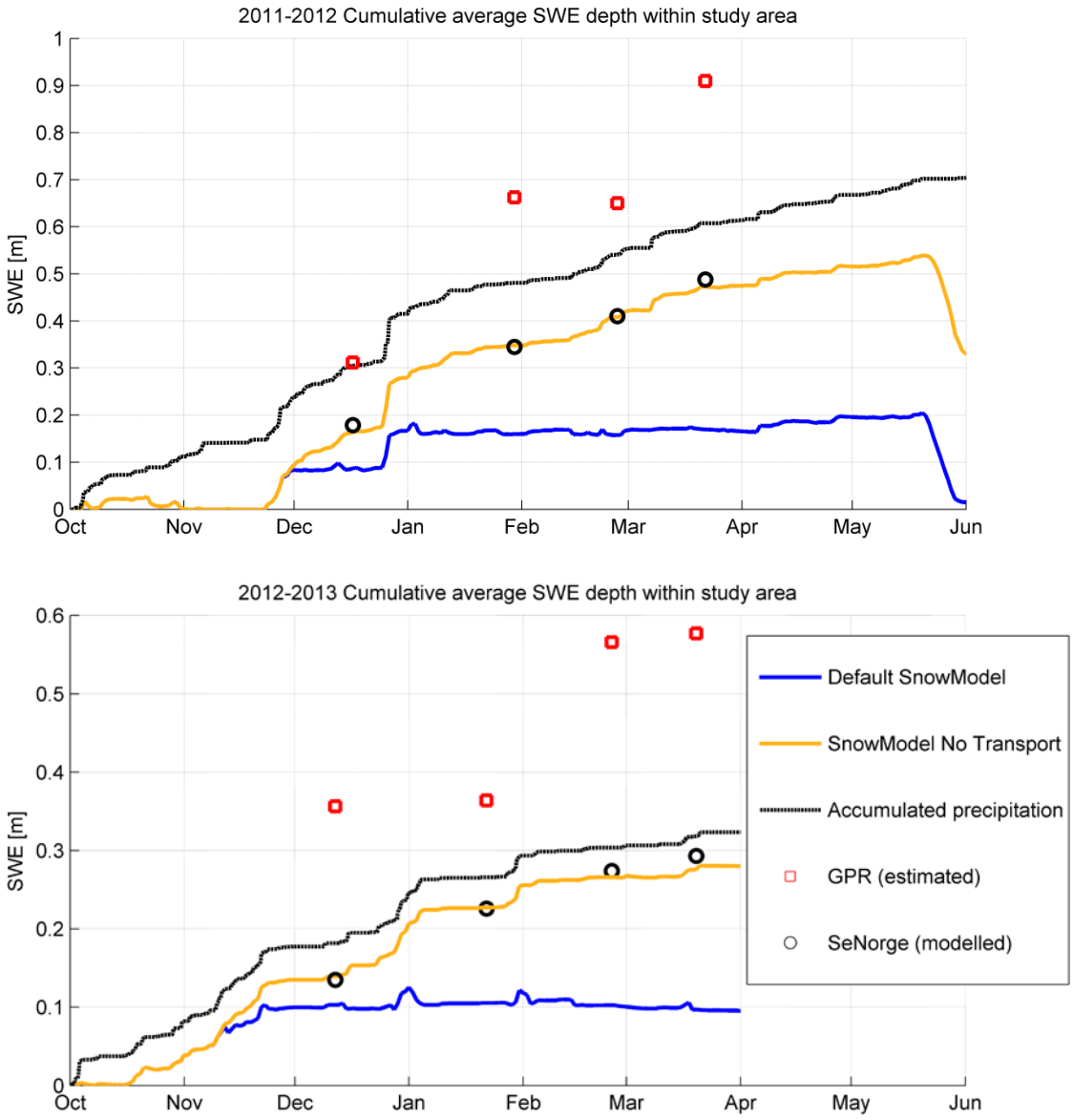

Figure 26 – Accumulated SWE for the two seasons of 2011-2012 and 2012-2013.

8 Model evaluation and adjustments

From the results of the default model, performance for the Finse study area was poor. The model wind field overestimates the observed wind speed at the validation stations. The increased speed will lead to more erosion and less deposition. Excessive transport might remove snow from the model domain, and produce the results observed.

The model has some accumulations of more than $8\,m$ and $7\,m$ in March 2012 and 2013 respectively, but these are sparsely distributed around the study area. This is consistent with the findings of Gascoin et al. (2012), who found that SnowTran-3D depletes the snow pack in surrounding areas and concentrates the transported snow in a few grid cells. They opted to run the model without SnowTran-3D, and do not propose reasons for, or solutions to, the problem. Figure 26 shows that there is a large discrepancy between modelled and observed snow mass.

It is deemed critical for the model to recreate approximate amounts of SWE retained in the terrain, before attempts are made at validating the spatial distribution.

In the following subchapters, different causes for the distribution issues are presented and discussed, and adjustments to compensate for the lack of snow are tested. First off is a discussion around the size of the model domain, followed by an analysis of the wind field and then a series of iterations to adjust calculations of snow surface density.

8.1 Model domain size

An explanation for the lack of snow is that the model domain is too small for this implementation, and snow is transported out of the model domain without being reintroduced. This in spite of the current size of 2500 by 1000 grid cells being within the recommended dimensions (pers.com. Liston, 2012) (Appendix E.1).

One method of correcting this would be to increase the model domain size. The model domain size is limited by the available memory on the client running the model. On hardware with more memory, it would be possible to increase the model domain to a size where net flux through the study area is smaller. The amount of snow transported out of the domain, however, and the rate at which it is transported, indicate the need for a much larger domain. Test runs of the default SnowModel were performed using hourly model output, in an attempt

to track the snow as it moves out of the domain. The data did not provide any additional insight, as snow was generally removed in the time step following a precipitation event.

Another method for handling the snow removal is to run he model on the same number of grid cells, but with each grid cell covering a larger area (increase the cell size). Test simulations were therefore performed with a $25\,m$ by $25\,m$ cell size and 2500 by 1000 grid cells. Results showed an increase in the snow retention of the default model, but the resulting snow cover was largely homogeneous. A complete assessment of the effects of scale and resolution is not within the scope of this thesis, so the resolution of $4\,m$ and a domain size of 2500 by 1000 is kept throughout the following simulations.

8.2 Sensitivity tests of wind speed

From Figure 19 we can see that there is a systematic difference between the observed wind speeds and modelled wind speeds.

The spatial interpolation of wind speed in Equation 14 can be rewritten as $W_t = V * W$ where W_t is the modelled wind speed, W is the model forcing wind speed and the total wind weight is $V = (1 + \gamma_s\Omega_s + \gamma_c\Omega_c)$ (Equation 14). V should approximate the ratio of observed wind speed W_o over model forcing wind speed W: W_o/W. The median ratio of model forcing data over observed velocities is 1.42, 1.50 and 0.72 for Stations A, B and C, respectively. To test this, W_o/W is calculated for all time steps at each of the three stations and compared with modelled V. V is controlled by three parameters; (1) the curvature length scale $\mu\,[m]$ (Equation 13); and (2) the curvature and slope weights γ_c and γ_s.

In an attempt to improve performance, parameters are evaluated by a series of Monte-Carlo (MC) simulations. The relative weights γ_s and γ_c and the curvature length scale μ are estimated by MC simulations to approximate the calculated total wind weights according to the Root Mean Square Error ($RMSE$) of V compared to W_o/W. As the ratio of W_o/W is unitless, $RMSE$ is also unitless. Figure 27 shows the results of the simulations. Default model parameters are $\gamma_s = 0.52$, $\gamma_c = 0.48$ and $\mu = 100\,m$, yielding an $RMSE = 0.71$. The plot shows that the $RMSE$ values are strongly controlled by slope, and with no substantial contribution from neither the curvature weight γ_c nor the curvature length scale μ. The minimum $RMSE = 0.46$ occurs at $\gamma_s = 0.25$, $\gamma_c = 5.70$ and $\mu = 100.23\,m$.

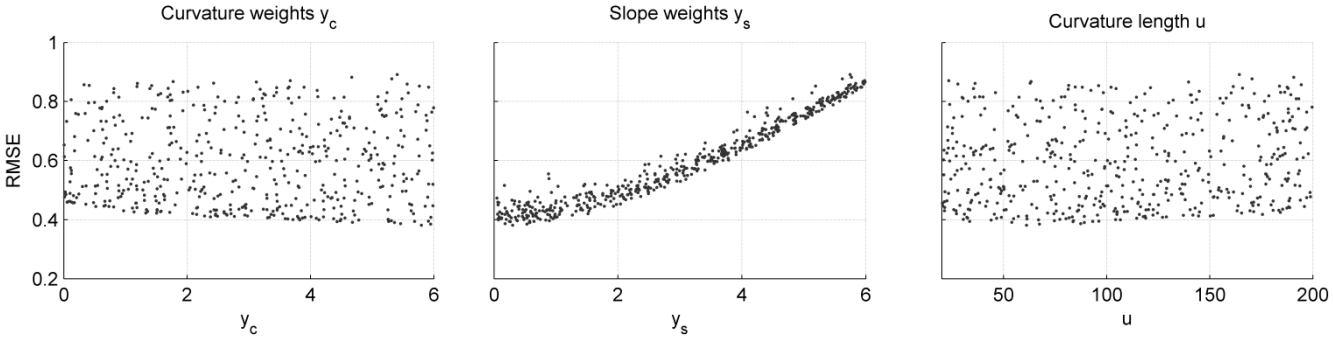

Figure 27 – Results of Monte-Carlo simulations of wind weight V given a parameter range of $[0\ 6]$ for γ_s and γ_c and a range of $[20\ 200]$ for μ.

Figure 28 shows all points for W_o/W along with the lines calculated for V using $\gamma_s = [0.58 \quad 1 \quad 0.25]$, $\gamma_c = [0.42 \quad 0 \quad 5.70]$ and $\mu = [100 \quad 100 \quad 100.23]$. The plots show that the median weights with parameters from MC are 0.90, 0.95 and 1.34 for Stations A, B and C, respectively. These values should therefore approximate median ratio of the observed over modelled velocities of 0.63, 0.57 and 0.97 for Stations A, B and C, respectively. Results show that in spite of improvements, the model will still overestimate the wind speed at Stations A and B, though by less than with the default weights.

SnowModel has hardcoded limits that do not allow γ_s or γ_c greater than 1, so the Monte-Carlo-acquired values are not applicable. Figure 28 shows that the weight equation is still not able to capture the variations in wind ratios. Therefore, the default weights are still used. SnowModel's calculations of slope and curvature might be modified to improve their ability to capture local topographic wind effects, but doing so within the time frame of the thesis was not possible.

The results of this analysis have a degree of uncertainty due to the lack of daily snow depth data at the weather stations. The snow depth at Stations A, B and C might reduce the wind speed substantially, making actual $2\,m$ wind speed higher than what is used in the analysis. The data periods used in the analysis is from March 22nd 2012 to March 20th 2013, resulting in about $1/3$ of the data experiencing snow depths warranting an adjustment.

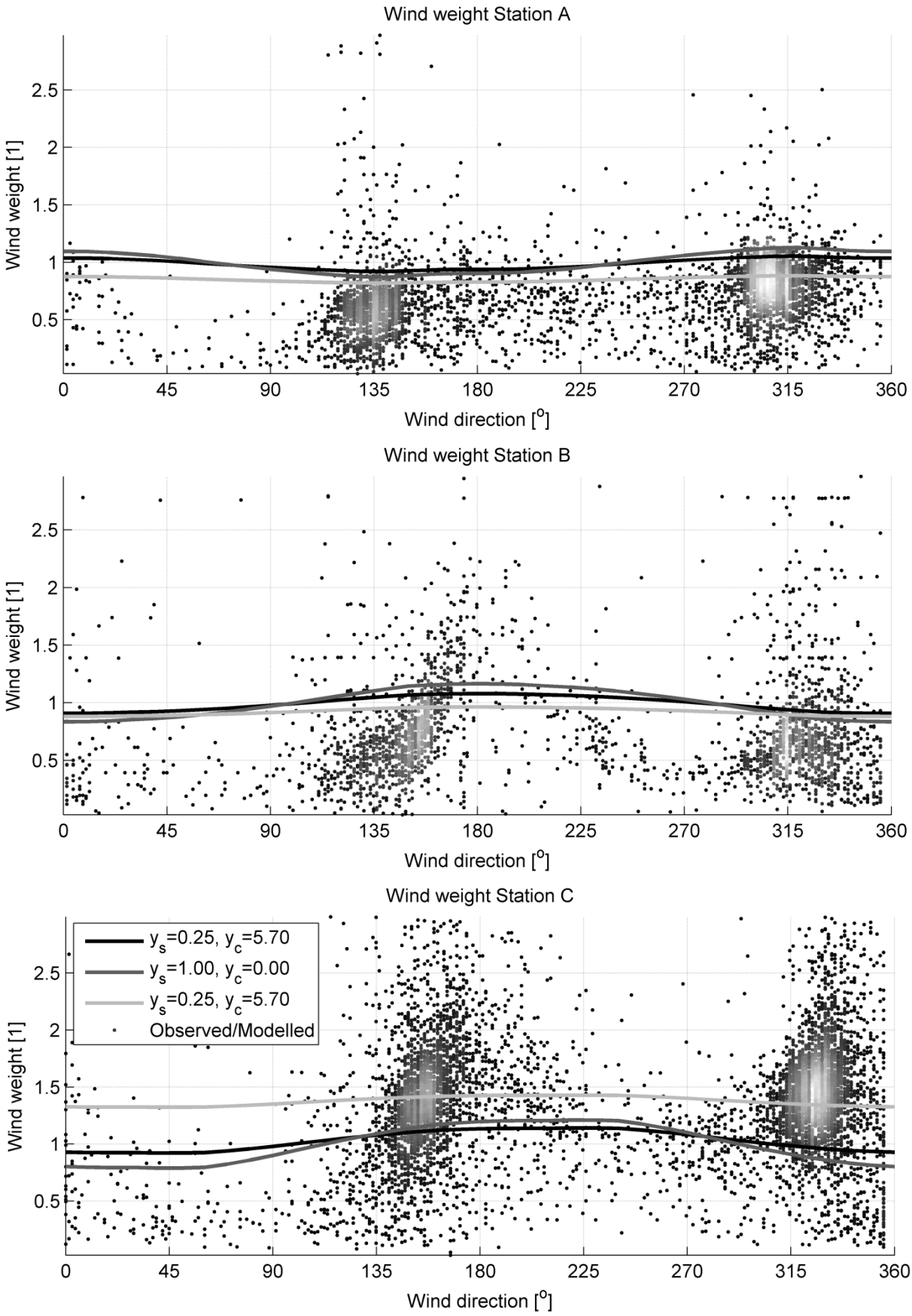

Figure 28 – Wind weights as a function of wind direction, along with the wind weights calculated for each of the observed datasets at Stations A, B and C. Scattered data is shaded for point density.

8.3 Wind direction and temperature

The median difference in wind direction between the model forcing data and the model results is 0°, with an average difference of 0.3°. Wind direction observations show that the wind direction for all stations has an axis tilt towards the north-south, compared to the model forcing data.

No modifications to the wind direction field are attempted, as the lack of variation between modelled and observed wind direction is so strong, and there are no parameters to adjust wind direction alterations.

The difference in wind direction between validation and model forcing data might be an effect of channelling through the valley, more than due to topographic curving of wind around the terrain immediately around the stations themselves. The model will not take into account these mesoscale topographic wind effects, so its ability to recreate these wind directions is poor. Increasing the scale of the model by any significant amount would require more accurate wind forcing data to function properly, due to one single station being incapable of capturing these wind fields. Model results might be improved by utilizing a more advanced wind field as input, like the MM5 data used as forcing data for SnowModel by Bernhardt et al. (2010).

Since our implementation of SnowModel only uses input from one single meteorological station, the models interpolation of temperature only relies on the temperature lapse rate. Thus, no adjustments to temperature interpolations are performed.

8.4 Improved snow density routines

Figure 29 contains the accumulated SWE depth for all the following iterations of the model. The lack of accumulation is apparent when compared with the GPR, accumulated precipitation and SeNorge. Since SnowModel with no transport manages to accumulate SWE corresponding more closely to the accumulated precipitation, it is apparent that snow is blown out of the model domain, without any new snow being reintroduced at the upwind boundary.

Each of the following iteration attempts to improve these results by altering SnowModel source code and recompiling the model with the new settings to perform the tests.

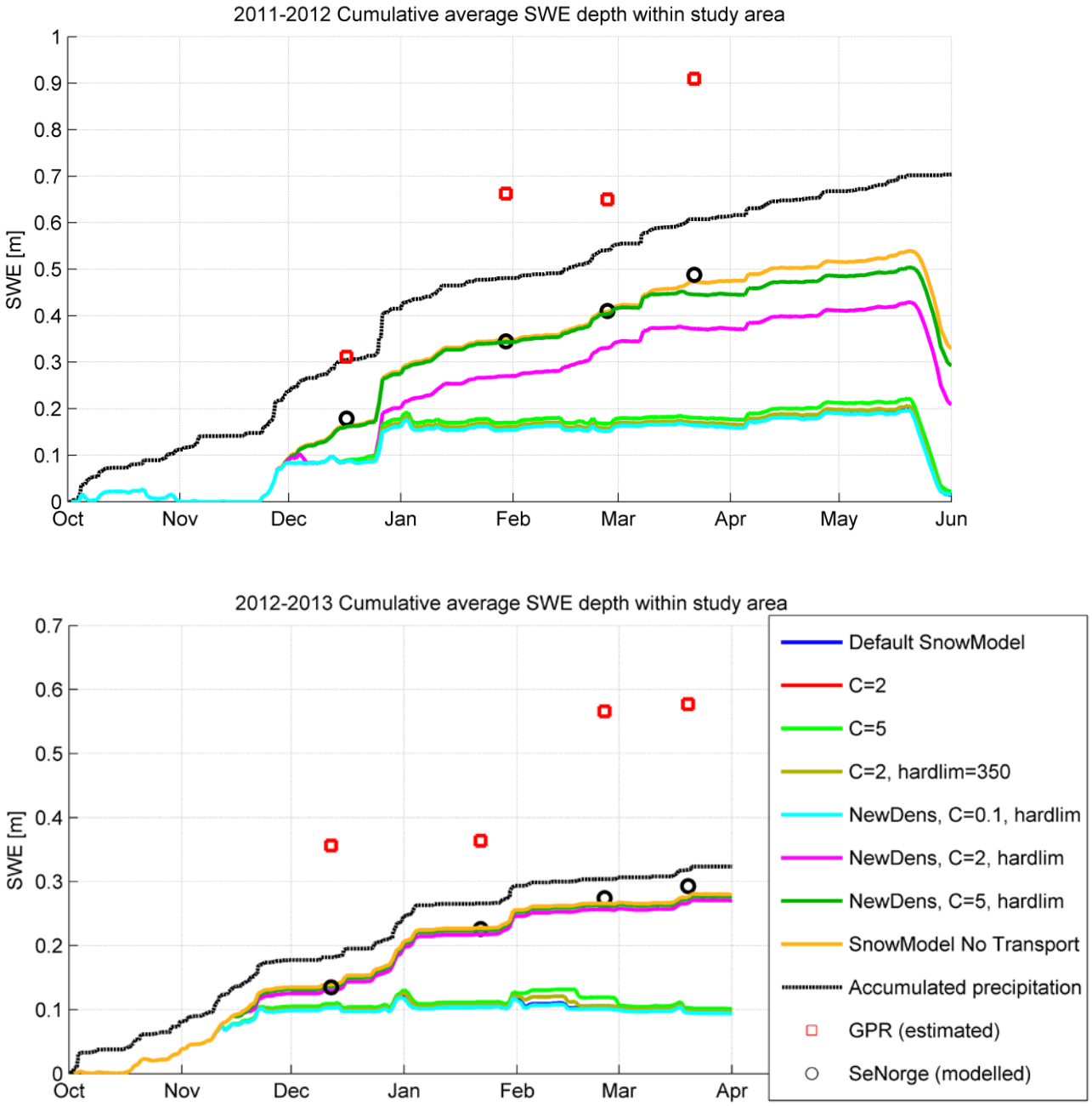

Figure 29 – Accumulated SWE for all model iterations for the two seasons of 2011-2012 and 2012-2013. Note: There is a lot of overlap between model iterations. With the exception of $NewDens, C = 2, hardlim$ and $NewDens, C = 5, hardlim$ and $SnowModel\ No\ Transport$, all iterations converge at 0.19 m (2011-2012) and 0.1 m (2012-2013). Accumulated precipitation accounts for all precipitation, not limited to snow.

8.4.1 Increased rate of surface density change

In 2011, the model only produced two significant accumulation events; one in late November and one late December. For 2013, there was an initial accumulation from October till mid-November, with two small accumulation events at the start of January and the start of February which were removed by the wind at approximately the same rate the snow was

introduced. There are no melt events, as air temperature is constantly below 0 ℃. Snow surface density controls the transport of snow through the calculations of threshold shear velocity (Equation 26). The initial assumption is therefore that the rate of surface density change is not high enough. If new snow is introduced, and the density of this snow is not significantly increased as a function of time, then the new snow will be removed from the domain before it is allowed to settle.

SnowModel calculates surface snow density as a function of wind speed and temperature, which is calibrated using the dimensionless parameter C (Equation 24). This parameter controls the rate of surface density change as a function of time. We therefore perform a sensitivity test on C to see if an increased snow surface density will result in more snow retention in the terrain. The initial value is $C = 0.1$, and the sensitivity test will encompass values up to $C = 5$.

The actual maps of snow surface density are not available as output from the model without substantial restructuring of the code. Sensitivity tests of snow surface density are therefore done on the basis of their impact on SWE accumulation.

In Figure 29, these tests are represented with $C = 2$ and $C = 5$. At both these instances, we see that the amount of SWE retained after the small accumulations period in February 2013 lasts longer before being removed. This indicates that even though the density is vastly increased, the snow is still eligible for transport. In general, we see is that even when increasing the rate of density change by a factor of 50, there is no significant change in the amount of snow retained in the terrain.

8.4.2 Immovable snow, density threshold

Further analysis of accumulation data shows that the only increase in SWE occurs when temperatures momentarily exceed 3 ℃. This is one of the limits for creating hard, immovable snow layers in SnowModel (Liston et al., 2007). The immovable snow layers, hard layers, represent the snow metamorphism brought on by high surface temperatures or by wind forces, giving the snow surface high shear strength. This hard layer is defined as completely immovable by wind, and can only be removed by snow melt. Snow that accumulates on top of hard snow is defined as soft, and can be moved as a function of surface shear stress and wind speed. An illustration of the effect of a temperature limit is found in Figure 30.

SnowModel documentation by Liston et al. (2007) states that there are two thresholds for creating hard layers. First is a temperature threshold of 3 ℃ which creates an immovable layer ice layer. The second threshold states that "at any point in time when the snow threshold velocity exceeds a value for snow that cannot be transported by naturally occurring winds (e.g. $u_{*t} \geq 1.7\ ms^{-1}$, corresponding to a $10\ m$ wind speed of approximately $40\ m\ s^{-1}$), the soft snow layer is added to the hard (unmovable) snow layer." (Liston et al., 2007)

This is effectively a density threshold for immovable layers, as surface density controls the snow threshold velocity through Equation 26.

A thorough walkthrough of the models code finds no evidence of this second condition in the calculations. Apparently, the density threshold for the hard layer was removed from the model as it did not significantly affect distribution results for the models current use (pers.com. Liston, 2013) (Appendix E.2). This leads to temperature being the only factor controlling hard and soft snow. Field observations show that hard immovable layers are common at Finse, but temperatures never exceed 3℃ during the winter. The issue is comparable to that encountered by Bruland et al. (2004) before the temperature hard layer limit was implemented into SnowModel. This might indicate that temperature is not the factor controlling their creation at Finse.

To reduce transport, the density threshold for hard immovable layers is reintroduced. If the surface density exceeds $350\ kg\ m^{-3}$, the entire snow pack is defined as immoveable snow, and it can only be removed by melting (Figure 31). As the manual snow density measurements done in relation to the GPR data showed hard surface densities in this range, it is assumed that this is a reasonable threshold. Due to the apparent initial lack of surface snow density change, the parameter C is kept equal to 2 (up from the initial 0.1).

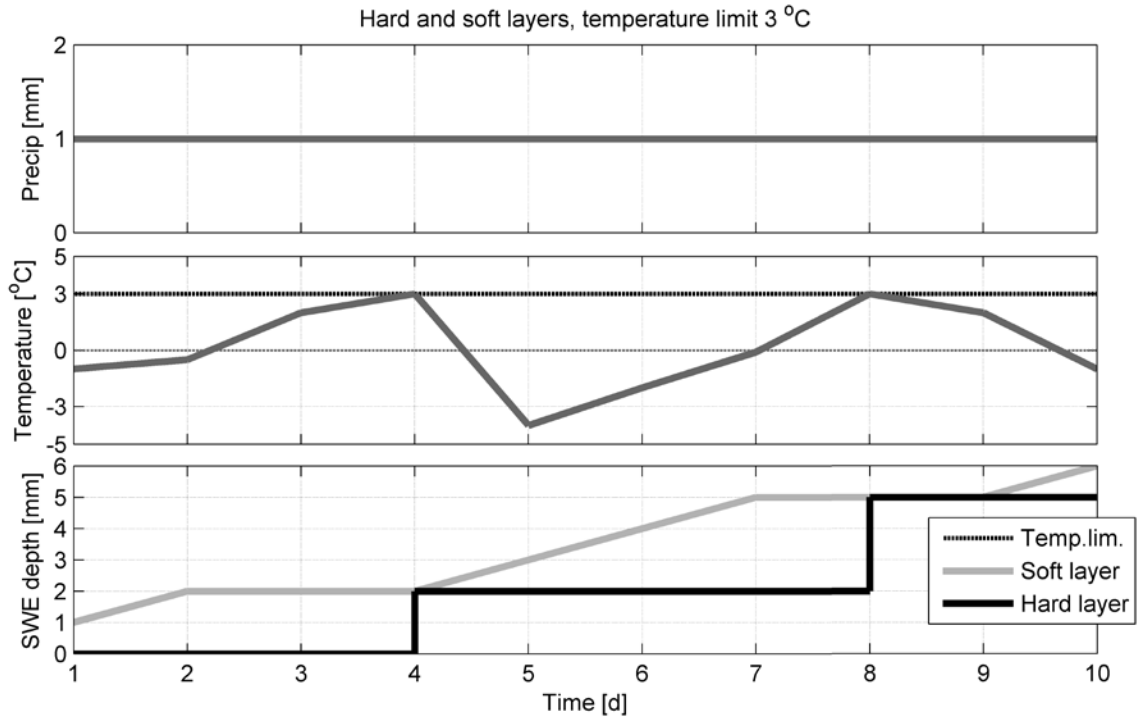

Figure 30 – A time series illustration showing the evolution of hard and soft snow. Soft and hard layers are shown as portions of the entire snow pack. 3 ℃ temperature limit to creating hard layers with constant precipitation and a 0 ℃ limit to solid precipitation.

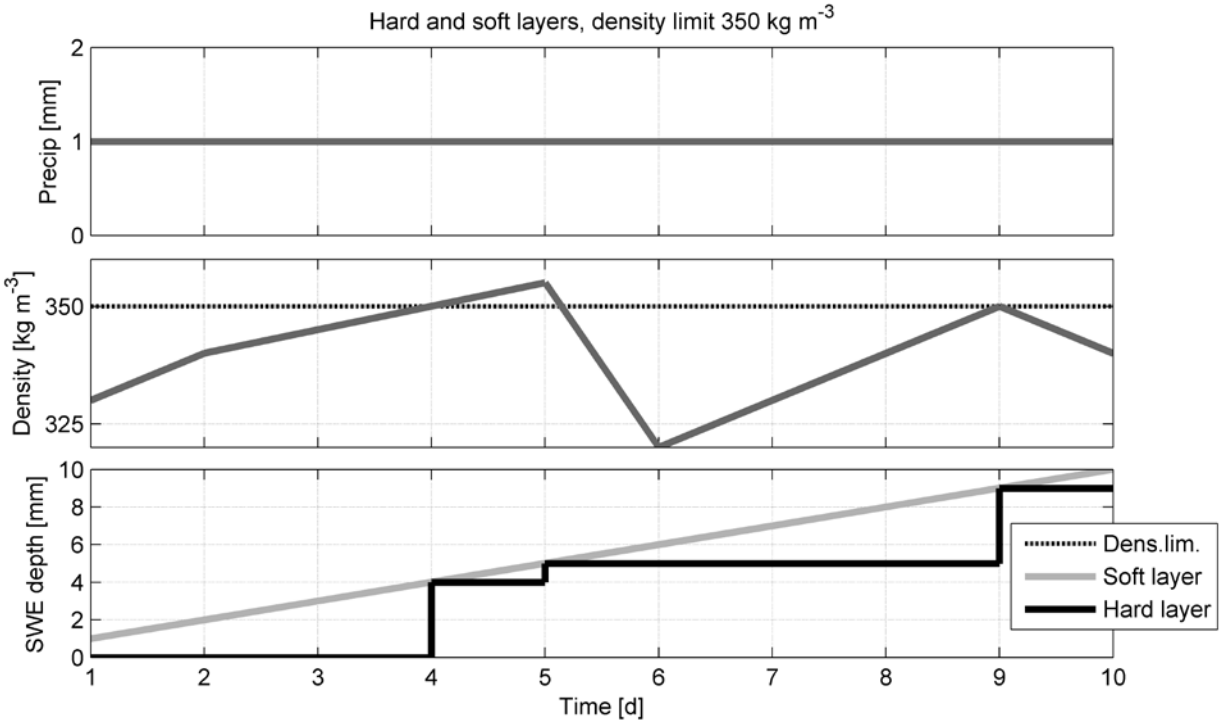

Figure 31 – A time series illustration showing the evolution of hard and soft snow. Soft and hard layers are shown as portions of the entire snow pack. 350 $kg\ m^{-3}$ temperature limit to creating hard layers with constant solid precipitation.

In Figure 29, all model results with a density threshold are named $hardlim$. There is no measurable difference between $C = 2, hardlim = 350$ and $C = 2$, indicating that surface snow density never exceeds 350 $kg\ m^3$ at any time during the simulations.

8.4.3 Weighted average new snow density

The model calculates new snow density according to Equation 22 and calculates change in surface snow density according to Equation 24. Further analysis of SnowModel's source code indicates that these calculations are not in effect at every time step, but are dependent on the amount of precipitation at any given time (Code 1). If precipitation is greater than $0\ mm$, the model sets the surface snow density (ro_soft_snow) equal to the density of the new snow plus a wind induced offset (ro_nsnow and ro_offset). If the precipitation is equal to $0\ mm$, the surface snow density is evolved by way of the method $surface\_snow\_2$, which contains the calculations of Equation 24.

```
if (prec.gt.0.0) then
[...]
        if (windspd_2m.lt.5.0) then
          ro_offset = 0.0
        else
          ro_offset = 25.0 +
     &      250.0 * (1.0 - exp(-(alfa*(windspd_2m - 5.0))))
        endif
        ro_soft_snow = ro_nsnow + ro_offset
[...]
else
        call
surface_snow_2(ro_soft_snow_old,ro_soft_snow,Utau_t,
     &    dt,Tair,windspd_2m,C,ro_max,ro_min,alfa,Tf)
[...]
end
```

Code 1 – Extract from file *snowtran_code.f*, the subroutine of SnowModel that handles snow transport. Written by Liston and Elder (2006a). Approximately lines 3390 through 3425.

The consequence of this is that the surface density may evolve through time, but the density is reset to that of new snow at any time step where there is precipitation (Figure 32). This means that the density threshold previously implemented in the model will not have any affect if precipitation events are close enough in time to reset the density before the threshold triggers. As temperature never exceeds the 3 ℃ threshold either, the result is that the snow pack gets a

very low surface density at any precipitation event, and snow will never be defined as hard. This inevitably leads to excessive amounts of snow transport.

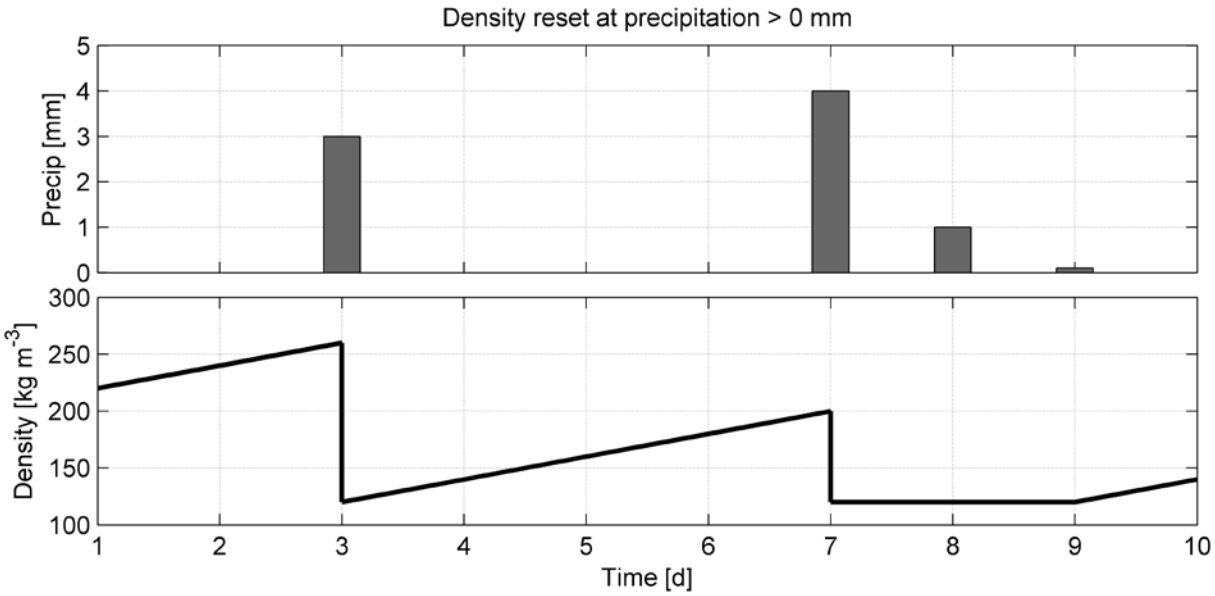

Figure 32 – A time series illustration showing the evolution of density as a function of time and precipitation. Assumes constant solid, a constant increase in density of 20 $kg\ m^{-3}\ d^{-1}$, and a new snow surface density of 120 $kg\ m^{-3}$.

To mitigate the effect of this parameterization, the calculation of surface density at new snow events is altered to not be controlled exclusively by new snow. This is done by setting the surface density after snow events ρ_{soft} $[kg\ m^{-3}]$ equal the weighted average of new snow density ρ_{new} $[kg\ m^{-3}]$ and soft layer density ρ_{soft_old} $[kg\ m^{-3}]$. The weights are the snow water equivalent depths d_{ns} and d_{soft} $[mm]$ representing by each layer:

$$\rho_{soft} = \frac{\rho_{new} * d_{new} + \rho_{soft\_old} * d_{soft\_old}}{d_{new} + d_{soft\_old}} \qquad \text{Equation 31}$$

This new parameterization should allow the surface snow density to evolve sufficiently to trigger the density threshold implemented earlier. This should create a hard, immovable snow layers and hopefully reduce snow transport. The hard snow density limit of 350 kgm^{-3} is kept, along with variations of $= [0.1 \quad 2.0 \quad 5.0]$.

Results in Figure 29 are represented by the three datasets identified by the $NewDens$ prefix. The variant $NewDens, C = 0.1, hardlim$ (model default C) does not show any significant change from the default model. This indicates that the density limit and the new density calculations are not sufficient on their own to keep snow from blowing out of the domain. The two other variants using $C = 2$ and $C = 5$ show an accumulation of snow more closely

resembling the model with no transport, and fit the general variation exhibited by the accumulated precipitation data. The average accumulated SWE does not indicate any spatial distribution, so an analysis of the actual distributions in comparison to GPR data is also needed.

Figure 33 contains snow distribution data for $NewDens, C = 2, hardlim$. The distribution map for March 2012 does not show any apparent distribution, as a few grid cells have outlier values of $5\ m$ which offset the linear colour map. Scatter plot and histogram show that the distribution is almost homogeneous and have no apparent covariation with GPR snow depth ($R^2 \approx 0$). The model manages to capture distributions of the most prominent topographical catches, but fails to accumulate snow on flat ground due to the excessive transport.

Figure 34 is a closer look at the results of $NewDens, C = 2, hardlim$ overlaid the results of the GPR. It is apparent that the model produces general distribution patters similar to those observed in GPR, but with no substantial accumulation, and very little spatial variation in the maximum and minimum snow depths.

Figure 35 shows the distribution of $NewDens, C = 5, hardlim$.When the maps are compared with Figure 33, it is apparent that the variation follows elevation and is controlled by precipitation lapse rates and differences in short wave radiation due to aspect. As a result of this lack of variation, the correlation between GPR and modelled snow depth is still very poor.

Despite the attempted adjustments, the model does not recreate GPR distributions adequately.

8.5 Variable transport boundary

The main problem for this particular implementation of SnowModel seems to be the general lack of snow. This lack of snow is a consequence of the model area being too small, resulting in a net transport of snow out of the model domain. Following is a suggestion for a simplification that would solve the snow removal issues, without compromising computational efficiency or resolution.

The easiest solution to a problem of outblown snow would be to increase the model area by increasing the number of grid cells or to increase the size of each cell. Adversely, an increase in domain size would be more computationally demanding, and an increased cell size would

reduce resolution of the snow distributions. A third solution, presented here, would be to force the model to not remove snow from the domain.

For small scale studies, one could assume that the down wind boundary of the study area experiences the same amount of outflow of snow as the upwind boundary experiences an inflow. The removal of snow could thereby be mitigated by forcing to model to reintroduce the out-blown snow at the opposite upwind boundary.

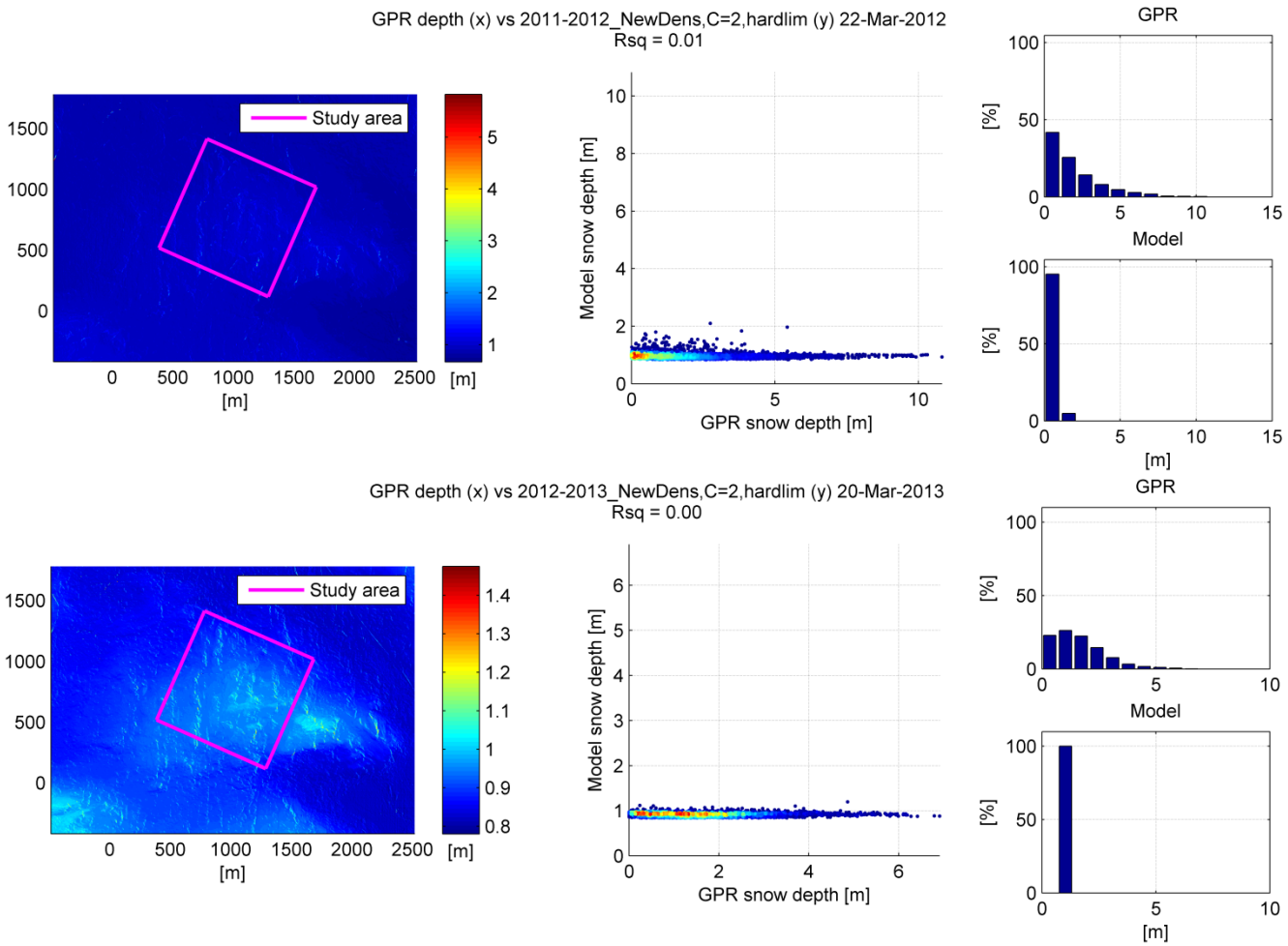

Figure 33 – Results of modelling the seasons of 2011-2012 and 2012-2013 weighted surface density calculations, $C = 2$ and an implemented surface density threshold of 350 $kg\ m^{-1}$ and the altered new snow density algorithm. Left figure shows modelled snow surface, colour coded for snow depth. Right plots are histograms showing the variation in snow depth in the GPR and modelled datasets for March 2012 and 2013.

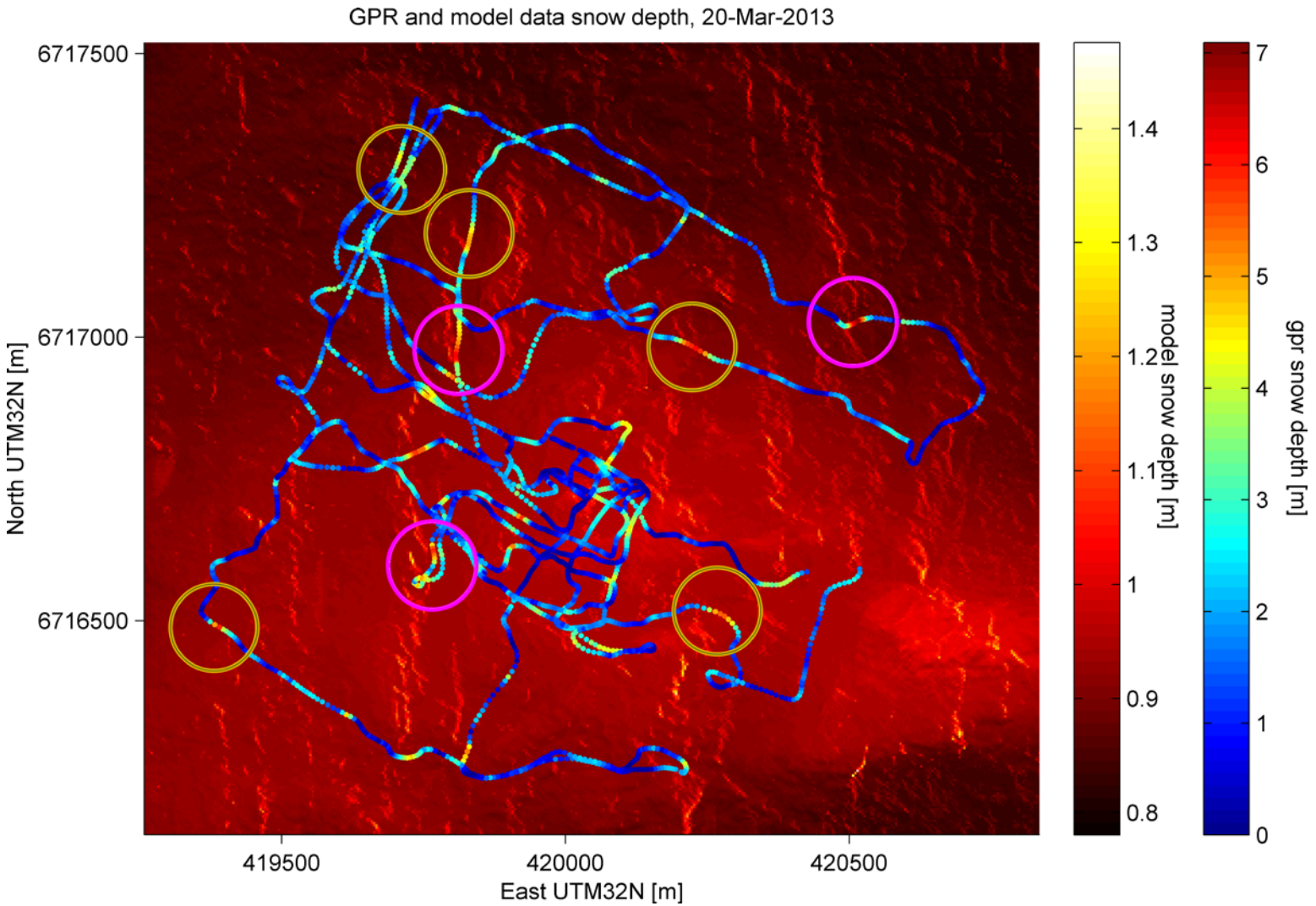

Figure 34 – GPR data overlaid modelled snow depth for $NewDens, C = 2, hardlim$. Purple and yellow circles mark examples were accumulations match and don't match, respectively. Circles are the same as in Figure 25.

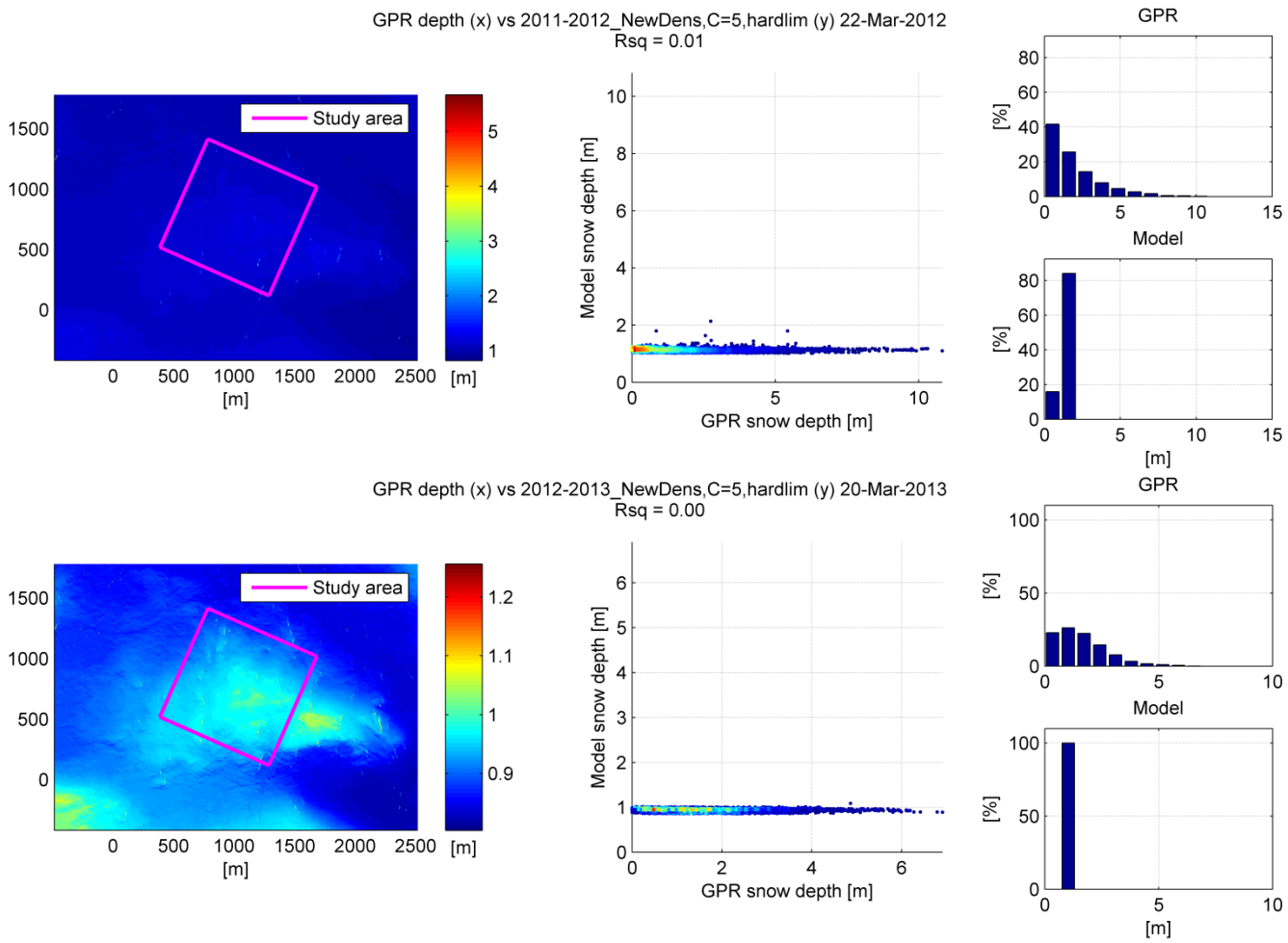

Figure 35 – Results of modelling the seasons of 2011-2012 and 2012-2013 with weighted surface density calculations, $C = 5$ and an implemented surface density threshold of 350 $kg\ m^{-1}$ and the altered new snow density algorithm. Left figure shows modelled snow surface, colour coded for snow depth. Right plots are histograms showing the variation in snow depth in the GPR and modelled datasets for March 2012 and 2013.

The mass, speed and direction of snow transport at any grid cell are known. Creating a variable transport boundary is a matter of identifying the cells that remove snow from the model area, and locate the opposite upwind boundary grid cell along the current wind direction. The out-blown snow is then introduced in the opposite upwind boundary grid cell with the already known mass, speed and direction. Developing a variable transport boundary in SnowModel is therefore technically possible.

The assumption of equal upwind and downwind transport may introduce new errors if the study area naturally experiences a net increase or decrease of snow due to transport to or from surrounding areas. No literature was found on the topic of variable transport boundaries. Writing and testing these algorithms within the SnowModel framework is time consuming, and was therefore not possible to study further in this thesis.

9 Discussion

9.1 Meteorological validation data

9.1.1 Temperature inversions

From the observed temperature data, we see that the model forcing data from the Finsevatn meteorological station experiences significant temperature inversions both during winter and spring (Figure 14). These inversions last from just a couple of hours to spanning several weeks with only intermittent temperature increases. The station collecting the model forcing data is located in an open area of low topography, down river from the Finsevatn lake (Figure 2). The meteorological validation stations are located at higher elevations in more exposed topography, and are therefore more likely to experience turbulence and mixing of air, while the Finsevatn station experiences an accumulation of cold air in the valley bottom. The inversion may also be increased by cold air flowing down into the valley from the ice covered lake and from katabatic winds from the Hardangerjøkulen glacier, just south west of the model forcing station (Sømme and Østbye, 1997). These findings are consistent with other research from the same area (Giesen and Oerlemans, 2010; Lilleøren et al., 2013).

With most winter inversions occurring when all meteorological stations are below -0 ℃, the impact on simulations will be limited. On the other hand, the spring inversion in May 2012 shows that the Finsevatn station observes temperatures below 0 ℃ while the validation stations observe temperatures above 0 ℃. This local variation may have significant effects on modelling snow melt, and care must be taken when using the Finsevatn station for large scale simulation or spatial interpolation.

As the scope of the modelling in this thesis is limited to the accumulation season, and the inversions do not adversely affect the evolution of accumulating snow, the impact on modelling results is assumed to be negligible.

9.1.2 Wind

Wind data from the validation stations show the characteristic wind speed distributions of the area, with most wind events occurring along a west-east axis (Sømme and Østbye, 1997). The

wind data also shows a considerable dependency on the local topography immediately around the stations them selves. Figure 11 shows that the stations capture how wind speed varies with shelter according to wind direction. Figure 10 shows that the wind speed distributions also capture local variations, with the exposed Station C showing higher wind speeds, while Station A and B show similar distributions owing to their more sheltered locations.

Due to a faulty wind sensor in Station A, continued data collection is only done at Station B and C.

9.2 GPR validation data

The discussion on GPR data will focus on the representativeness of topographic characteristics, uncertainty, and a look at the amount of snow observed by GPR, in that order.

9.2.1 Representativeness of terrain parameters

To be sure that the GPR data provides a reliable picture of the conditions in the study area, we compare the terrain characteristics beneath the GPR track with the terrain characteristics of the entire study area framed by the GPR grid (Figure 2).

The terrain in the study area is very rough, and this poses significant limitations on where it is possible to perform GPR measurements with a snowmobile. The planned tracks seen in Figure 2 were used to guide the snowmobile, but the actual tracks were controlled by the terrain in the immediate area and the local snow conditions. Therefore, the comparison between study area terrain characteristics and GPR terrain characteristics are done using the recorded track from a complete GPR survey of the study area instead of the planned track. The chosen GPR set for the comparison was from March 22nd 2012, which is the most complete set. The results can be seen in Figure 36. The plots to the left are the study area distributions of aspect, curvature, slope and elevation. The plots to the right are the corresponding values extracted from the GPS positioning of the GPR.

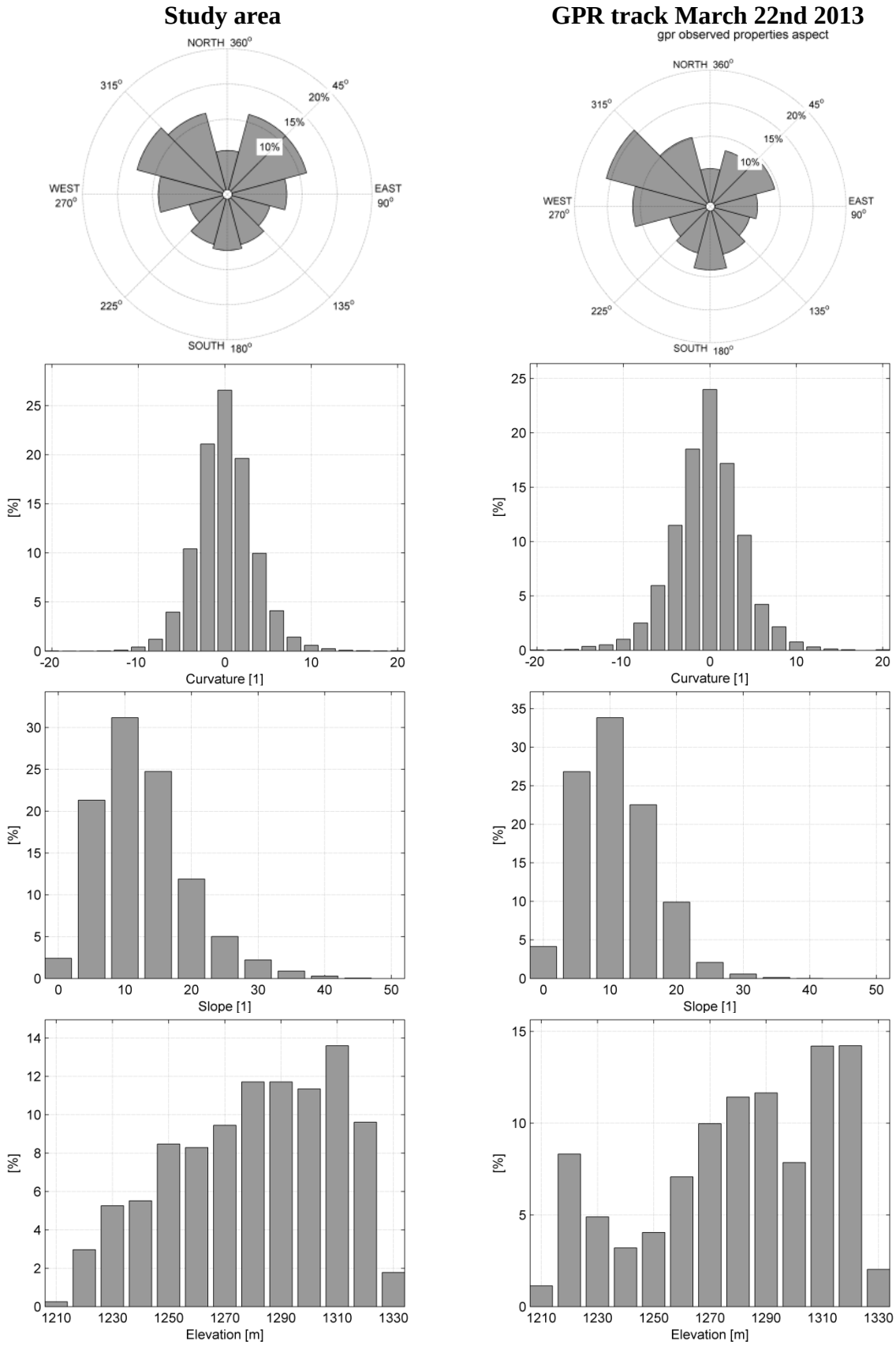

Figure 36 – Comparison of study area terrain parameters between the entire study area and the GPR track from March 22nd 2012,

From these plots we see that the GPR track is representative of the study area in regards to aspect, slope and curvature. The elevation distribution is not the same, owing to some of the east-west GPR tracks follow the same elevation, and thereby having too many measurements in the $1220\,m$ range. As the elevation differences in the area are small, the orographic component of precipitation is assumed to be negligible. Slope, curvature and aspect fit well, and are also the most important regarding deposition and erosion of snow on smaller scales (Liston et al., 2007).

9.2.2 GPR uncertainty

The GPR datasets have some aspects that introduce uncertainties. The primary factors introducing uncertainty in the GPR data are; (1) the non-static nature of the GPR tracks from month to month, (2) incomplete monthly datasets, (3) the manual processing of raw GPR data, (4) the snow densities derived from snow pit surveys, and (5) the use of Kovacs et al (1994) for conversion from density to signal times (Dunse et al., 2008).

Due to varying snow conditions, the GPR tracks differ each month (Figure 16). This makes for varying representativeness and completeness of the datasets. These errors are hard to correct for and difficult to avoid in areas of rough topography and varying snow condition. Attempts were made to mitigate the effects by having flexible time windows for field work, to be able to prioritize field work when weather and snowmobile conditions were optimal.

Incomplete monthly datasets are the consequence of the difficult physical conditions and with GPR/GPS errors. Equipment errors were mainly a problem during the first field season. By the second season, practical experience with the GPR system made identifying and correcting any issues much smoother, and datasets are more complete.

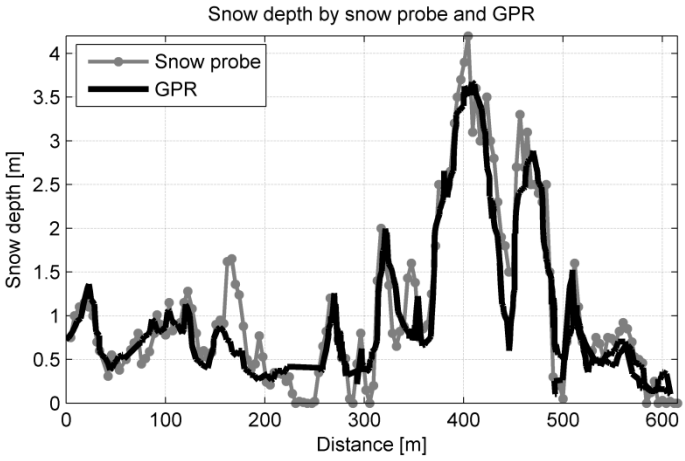

Figure 37 – Comparison of snow depth measurement with manual probe and Ground Penetrating Radar from Juvass. Data collected by Kjersti Gisnås.

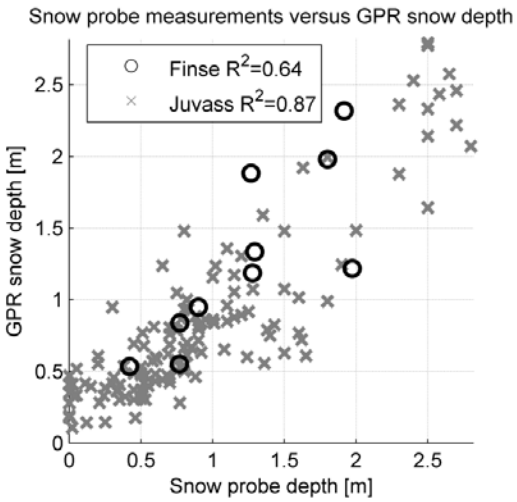

Figure 38 – Snow depth covariation between GPR and manual snow probing. Measurements were performed at distributed points and not continuous stretches.

Manually tracking reflection horizons may introduce an error if the wrong wave is selected as a ground reflection. To validate the GPR data in this project, two sets of manual snow probe measurements collected: One extensive at Juvass, Norway, performed by Kjersti Gisnås on March 28th 2012, and one less extensive at Finse performed by Tobias Litherland on February 25th 2013. Figure 37 shows the data from Juvass. Here, manual snow probe measurements were performed at $4\,m$ intervals over a stretch of $600\,m$, along with GPR snow depth for the exact same profile. The data fit reasonably well, with the exception of the GPR under-estimating some spiked depths. This is consistent with scattered data in Figure 38. Here, the decreased R^2 value of Finse may be due to the smaller sample size. The R^2 across all calibration measurements equals 0.87. The standard deviation is $0.42\,m$ between snow probe and GPR depth. The data is not normally distributed, as the data has a significant skew at higher depths (Figure 39). The deviation between probe depth and GPR depth is a function of snow depth, making the deviance not entirely random. Regular standard deviation and R^2 do therefore not give a complete picture of the covariation between the data. This fact makes a more precise analysis of the actual uncertainty of the GPR data difficult, and not possible within the bounds of this thesis. Given the generally good covariation in Figure 38, the GPR data is found to follow the spatial variation of snow depth well.

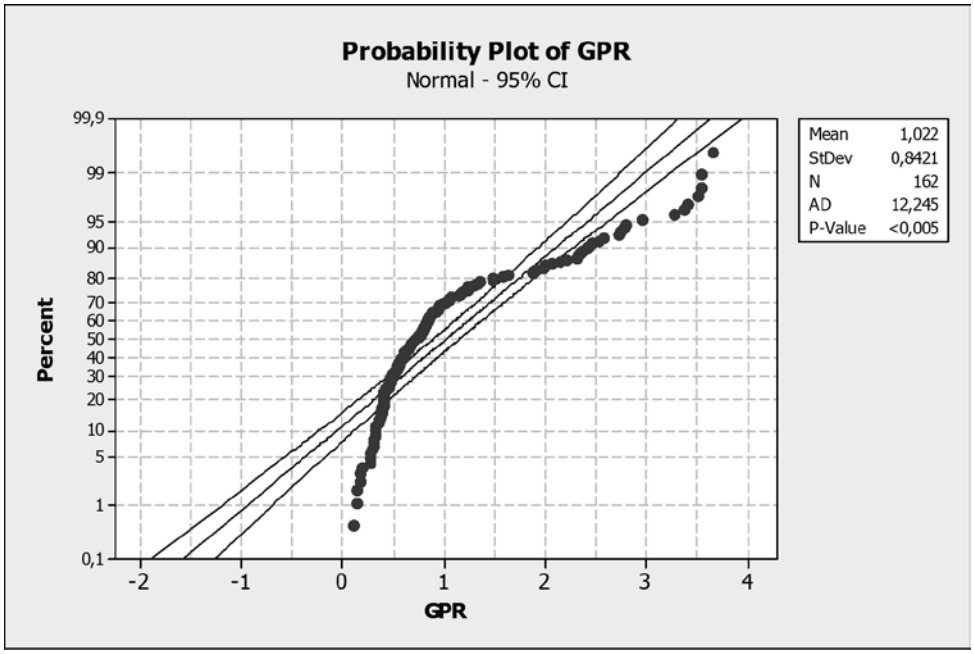

Figure 39 – Normal probability plot of GPR calibration data. Central line shows a perfect normal distribution, with the enclosing lines defining the 95% confidence interval for a normal distribution.

Good quality snow density measurements are important for the conversion of signal times to snow depths. The offset between probe and GPR measurements is also a function of the uncertainty in the density data. The average difference within each monthly measurement is 14 %. Figure 40 shows a plot of snow depth as a function of density for a given two-way signal time of 5 ns. The depth decreases as a function of density. The plot shows that ± 14 % yields a maximum offset of $+0.40\ m$ and – 0.30 if the initial density is 330 $kg\ m^{-3}$. Figure 41 shows the average offset in depth given a ± 14 % error in density for various initial densities. As bulk densities are in the range of 300 to 450 kgm^{-3}, the assumed maximum offsets for $t = 5\ ns$ are between 0.28 and 0.42 m. The offsets scale linearly with signal time, so a signal time of $t = 2.5\ ns$ will have possible offsets of between 0.14 and 0.21 m. This calculates to an uncertainty of 14.2 % in depth measurements.

Uncertainty regarding GPR snow depth measurements may also arise from ambiguity of reflections and anomalies beneath the snow (Dunse et al., 2008). Ambiguities in the reflected signals arise when the snow is deeper than the GPR signal times can accommodate. Anomalies under the snow tend to come in the form of split rocks with shear sides and frozen water, both distorting the signal and misrepresenting the ground snow interface. Both these types of errors are very hard to correct (Jaedicke, 2003). The only feasible way of handling

them is removing traces that have evidence of these kinds of errors. In the entire data set there were no substantial ambiguities or anomalies.

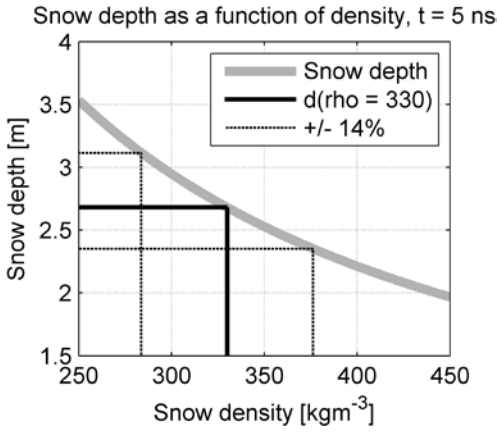

Figure 40 – Snow depth as a function of density for a two-way signal time of $5\,ns$. Example showing the depth given $\rho = 330\ kgm^{-3}$, with 14% uncertainty.

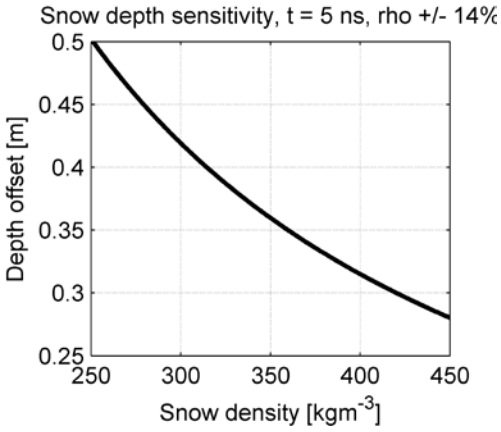

Figure 41 – Offset in snow depth given a 14% uncertainty in density in various initial densities.

In total, the GPR snow depth data is subject to an estimated uncertainty of 14 % due to snow density measurements and an unknown uncertainty due to inconsistent data coverage and the offset between manually picked GPR-depth and manual snow probe measurements.

For hydrological and engineering applications, it is preferable with an accuracy of $\pm 0.10\ m$ in snow depth (Jaedicke, 2003). Given this limit, the uncertainty is acceptable for snow depths below $0.70\ m$ ($0.70 * 14.00\% = 0.098\ m$). The uncertainty will increase linearly with depth with an uncertainty of $1.40\ m$ for snow depths of $10\ m$.

In spite of this, the data is still considered a viable means of assessing snow distributions: The GPR data covers a large area with a good temporal resolution, tracks show a representative coverage of terrain characteristics, the processed GPR data shows a good covariation with probe depths, and the snow surface follows the terrain according to prevailing wind directions and topographic catches. In general, the datasets is should be able assess a models ability to recreate seasonal snow distribution patterns.

9.2.3 GPR snow distributions

Data from the ground penetrating radar surveys show variations in the spatial distribution of snow from 0 to $12\ m$ of snow, and an increase in the depth variation as the seasons progress. The data shows a high degree of topographic dependency, with lee side accumulation with regards to prevailing wind directions. The data is somewhat hampered by incomplete monthly

sets due to difficult field conditions. However, both seasons contain complete measurements for March, giving information on the seasonal maximum snow distributions. With the exception of missing data, the data has few obvious errors. Analysis shows that the GPR tracks are representative of the study area with regards to terrain parameters, and have an uncertainty within acceptable limits for distribution analyses. The data should produce snow distributions that are representative of the area.

Table 6 – SWE depth for study area, all units in mm.

Data	March 22nd 2012	March 20th 2013
GPR	909.55	577.00
Snow pit	891.00	408.00
Accumulated model forcing precip. from Oct. 10.	607.67	318.88
Accumulated model forcing precip. from Oct. 10. No wind correction.	401.93	206.81

When calculating the SWE depth from the GPR sets, they show a much larger amount of snow than what is given by accumulated precipitation alone (Figure 29). Table 6 contains SWE depth calculated from GPR data, snow pit data and accumulated precipitation for both model forcing data and model forcing data without the wind correction from Equation 28. Data shows that the model forcing precipitation is substantially corrected for undercatch, so it is assumed unlikely that the remaining discrepancy is due to even further undercatch. Another explanation is that snow is eroded from the more gentle terrain to the west and deposited at Vesle Hansbunut. This snow movement may indicate that large scale redistributions of snow are in effect, making the study area a preferable site for studies of snow distributions models. If so, the data also shows that a model domain for the area needs to encompass a larger surrounding area to be able to recreate these effects.

9.3 Model performance

SnowModel with default parameters and algorithms performs poorly for the model implementation at Finse. All simulations, regardless of improvements, produced an $R^2 \approx 0$ when compared to the GPR snow distribution observations.

A raw comparison of GPR data and snow distributions show that the default model manages to recreate some of the snow in the most prominent topographic catches, but fails to accumulate snow on flat ground. The 4 encountered issues in the default model are; (1) wind speed calculations not reproducing observed wind speeds; (2) that the snow surface density is being forced equal to new snow density at precipitation events; (3) the lack of a wind-induced hard layer algorithm; and (4) transport of snow out of the domain.

It is assumed that these disparities are a result of the climate at Finse. Snow redistribution simulations with SnowModel have primarily been performed in continental climates (Liston and Sturm, 1998; Liston et al., 2007; Liston et al., 2008; Bernhardt et al., 2009; Bernhardt et al., 2010) and arctic climates (Hasholt et al., 2003; Bruland et al., 2004; Liston and Elder, 2006a; Mernild, Liston, Steffen, et al., 2010; Mernild, Liston, van den Broeke, et al., 2010; Mernild et al., 2011). Finse experiences a higher annual precipitation which is more evenly distributed through the year, compared to these temperate continental and arctic climates (Pomeroy and Gray, 1990; Dingman, 2002). The more temporally distributed precipitation at Finse may need a different conceptualization of snow surface density evolution, and would explain issue (2). Finse also seems to experience a higher average $2\,m$ wind speed than the studies performed in Greenland (Hasholt et al., 2003) and Svalbard (Bruland et al., 2004), which might be the reasons for issues (1) and (4).

For issue (1), adjustments to model parameters to alter the model wind field did not significantly impact the simulations. For issues (2), (3) and (4), increasing the rate of snow density change (C) did only increase the average SWE depth when coupled with a density threshold and weighted average calculations of surface snow density. These adjustments had the adverse effect of a homogeneous snow cover.

In general, the analysis shows that SnowModel has worked well for high resolution simulations in continental and arctic climates, but further development is needed to be sufficiently applicable in temperate, non-continental alpine climates.

10 Conclusion

Knowledge of the distribution of seasonal snow is important for a long range of applications. This thesis has presented an approach to data collection and evaluation of snow distribution models for Finse, an alpine site in Norway. This study has presented the following: (1) A data collection campaign where snow distributions, temperature, wind direction and wind speed were collected and analysed; (2) a parameterization of SnowModel and the results of an implementation at the study area of Finse; and (3) an evaluation of model results based on a comparison with the observed snow, temperature, wind speed and wind direction data together with a series of adjustments to SnowModel with the aim of improving results for this specific implementation.

The data sets of snow distribution cover the planned 4 months over the 2 seasons, and show a varied snow distribution based on wind direction and topographic features. The GPR tracks are representative of the topographic characteristics of the study area, and have an acceptable uncertainty with regards to analyses of distributed snow cover. The installed meteorological stations have performed well, and captured the intended topographic variability in wind speed and direction, and containing very little artefacts and corrupted values. These data sets are deemed capable of assessing the performance of a wide range of snow distribution models for application in a Norwegian, alpine climate.

SnowModel has been implemented for the selected study area, and its performance has been evaluated according to the collected field data. An analysis of the results has shown some areas of improvement for model application the windy, cold and wet climate at Finse:

i. The modelled wind distribution does not show sufficient topographic variation.

ii. Hard, immovable snow is only recreated as a function of temperature, while the study area experiences hard snow induced by wind speed.

iii. Snow surface density is set equal to new snow density at any precipitation event, leading to excessive transport at continuous precipitation events.

iv. Snow is removed from the modelling domain without any snow being reintroduced upwind, leading to large discrepancies between input precipitation and modelled snow.

Adjustments to the model with the aim of improving performance managed to increase the snow retention in the terrain, at the expense of spatial variation. In general, the modelled snow distributions did not resemble the observed snow distributions. Further studies of SnowModel in a Norwegian, alpine climate should attempt to more thoroughly implement and test the model adjustments presented.

In conclusion, this study has attempted to increase knowledge of snow distributions in Norway, and has succeeded in the identifying local snow cover conditions that make modelling of snow distributions in a temperate, non-continental alpine climates conceptually different from other areas were SnowModel has been successfully implemented previously. This knowledge and the data collected may help to improve snow distribution models for similar climates.

References

Anderson, E. A. (1976). A point energy and mass balance model of a snow cover. *NOAA Tech. Rep., 19*.

Bernhardt, M., Liston, G. E., Strasser, U., Zängl, G., & Schulz, K. (2010). High resolution modelling of snow transport in complex terrain using downscaled MM5 wind fields. *The Cryosphere, 4*, 15.

Bernhardt, M., Zängl, G., Liston, G. E., Strasser, U., & Mauser, W. (2009). Using wind fields from a high-resolution atmospheric model for simulating snow dynamics in mountainous terrain. *Hydrological processes, 23*(7), 1064.

Berthling, I., Eiken, T., & Sollid, J. L. (2001). Frost Heave and Thaw Consolidation of Ploughing Boulders in a Mid-Alpine Environment, Finse, Southern Norway. *Permafrost and Periglacial Processes, 12*, 12.

Blöschl, G., Gutknecht, D., & Kirnbauer, R. (1991). Distributed snowmelt simulations in an alpine catchment. *Water resources research, 27*(12), 3171.

Bruland, O., Liston, G. E., Vonk, J., Sand, K., & Killingtveit, Å. (2004). Modelling the snow distribution at two high arctic sites at Svalbard, Norway, and at an alpine site in central Norway. *Nordic hydrology, 35*(3), 191.

Dadic, R., Mott, R., Lehning, M., & Burlando, P. (2010). Wind influence on snow depth distribution and accumulation over glaciers. *Journal of Geophysical Research, 115*, 8.

Davis, J. L., & Annan, A. P. (1989). Ground-Penetrating Radar for High-Resolution Mapping of Soil and Rock Stratigraphy. *Geophysical Prospecting, 37*, 20.

Dingman, S. L. (2002). *Physical hydrology* (2 ed.): Waveland Press, Inc.

Dunse, T., Eisen, O., Helm, V., Rack, W., Steinhage, D., & Parry, V. (2008). Characteristics and small-scale variability of GPR signals and their relation to snow accumulation in Greenlands percolation zone. *Journal of Glaciology, 54*(185), 10.

Erxleben, J., Elder, K., & Davis, R. (2002). Comparison of spatial interpolation methods for estimating snow distribution in the Colorado Rocky Mountains. *Hydrological processes, 16*(18), 3627.

Essery, R., Samuel, M., Lajeune, Y., & Ménard, C. B. (2013). A comparison of 1701 snow models using observations from an apline site. *Advances in Water Resources, 55*, 17.

Evans, S. (1965). Dielectric properties of ice and snow - a review. *Journal of Glaciology, 5*(42), 19.

Førland, E., Allerup, P., Dahlström, B., Elomaa, E., Jónsson, T., Madsen, H., . . . Vejen, F. (1996). Manual for Operational Correction of Nordic Precipitation Data. E. Førland (Ed.)*: The Norwegian Meteorological Institute*. Report Nr. 24/96

Galley, R. J., Trachtenberg, M., Langlois, A., Barber, D. G., & Shafai, L. (2009). Observations of geophysical and dielectric properties and ground penetrating radar signatures for discrimination of snow, sea ice and freshwater ice thickness. *Cold Regions Science and Technology, 57*(1), 29-38.

Gascoin, S., Lhermitte, S., Kinnard, C., Bortels, K., & Liston, G. E. (2012). Wind effects on snow cover in Pascua-Lama, Dry Andes of Chile. *Advances in Water Resources, 55*(2013), 14.

Gauer, P. (2001). Numerical modeling of blowing and drifting snow in Alpine terrain. *Journal of Glaciology, 47*(156), 97.

Giesen, R. H., & Oerlemans, J. (2010). Response of the ice cap Hardangerjøkulen in southern Norway to the 20th and 21st century climates. *The Cryosphere, 4*, 22.

Greene, E. M., Liston, G. E., & Pielke, R. A. s. (1999). Simulation of above treeline snowdrift formation using a numerical snow-transport model. *Cold regions science and technology, 30*(1-3), 135.

Harris, C. M., D.V., Isaksen, K., Haeberli, W. S., J.L., King, L., Holmlund, P., Francesco, D., . . . Palacios, D. (2003). Warming permafrost in European mountains. *Global and planetary change, 39*(3-4), 215.

Hasholt, B., Liston, G. E., & Knudsen, N. T. (2003). Snow-distribution modelling in the Ammassalik region, south east Greenland. *Nordic hydrology, 34*(1/2), 1.

Heimstra, C. A., Liston, G. E., & Reiners, W. A. (2002). Snow Redistribution by Wind and Interactions with Vegetation at Upper Treeline in Medicine Bow Mountains, Wyoming, U.S.A. *Arctic, Antarctic and Alpine Research, 34*(3), 262-273.

Jaedicke, C. (2003). Snow Mass Quantification and Avalanche Victim Search By Ground Penetrating Radar. *Surveys in Geophysics, 24*, 14.

Jaedicke, C., & Sandvik, A. D. (2002). High resolution snow distribution data from complex Arctic terrain: a tool for model validation. *Natural hazards and Earth System Sciences, 2*, 8.

Kind, R. J. (1992). One-Dimensional Aeolian Suspension Above Beds Of Loose Particles - A New Concentration-Profile Equation. *Atmospheric Environment, 26A*(5), 4.

Kirnbauer, R., Blöschl, G., & Gutnecht, D. (1994). Entering the era of distributed snow models. *Nordic hydrology, 25*(1), 1.

Kohler, J. C., Moore, J. C., Kennett, M., Engset, R., & Elvehøy, H. (1997). Using ground-pentrating radar to image previous years summer sirfaces for mass-balance measurements. *Annals of Glaciology, 24*, 6.

Kojima, K. (1967). Densification of seasonal snow cover. *Physics of Snow and Ice: proceedings= 雪氷の物理学: 論文集, 1*(2), 929-952.

Kovacs, A., Gow, A. J., & Morey, R. M. (1995). The in-situ dielectric constant of polar firn revisited. *Cold Regions Science and Technology, 23*, 11.

Lehning, M., Löwe, H., Ryser, M., & Raderschall, N. (2008). Inhomogeneous precipitation distribution and snow transport in steep terrain. *Water Resources Research, 44*, 19.

Lehning, M., Völksch, I., Gustafsson, D., Nguyen, T. A., Stähli, M., & Zappa, M. (2006). ALPINE3D: a detailed model of mountain surface processes and its application to snow hydrology. *Hydrological processes, 20*(10), 2111.

Lilleøren, K. S. H., O., Nesje, A., & Etzelmüller, B. (2013). Holocene development and geomorphic processes at Omnsbreen, southern Norway: Evidence for glacier–permafrost interactions. *The Holocene, 0*(0), 14.

Liston, G. E. (1995). Local advection of momentum, heat, and moisture during the melt of patchy snow covers. *Journal of applied meteorology, 34*(7), 1705.

Liston, G. E. (2012). Email: [Re: Questions regarding a study in Norway using SnowModel]. Recieved: 20.09.2012. Can be found in Appendix E.1

Liston, G. E. (2013). Email: [RE: Questions regarding SnowModel]. Recieved: 03.04.2013. Can be found in Appendix E.2

Liston, G. E., & Elder, K. (2006a). A distributed snow-evolution modeling system (SnowModel). *Journal of hydrometeorology, 7*(6), 1259.

Liston, G. E., & Elder, K. (2006b). A meteorological distribution system for high-resolution terrestrial modeling (MicroMet). *Journal of hydrometeorology, 7*(2), 217.

Liston, G. E., Haehnel, R. B., Sturm, M., Heimstra, C. A., Berezovskaya, S., & Tabler, R. D. (2007). Instruments and methods: Simulating complex snow distributions in windy environments using SnowTran-3D. *Journal of Glaciology, 53*(181), 241.

Liston, G. E., & Hall, D. K. (1995). An energy-balance model of lake-ice evolution. *Journal of Glaciology, 41*(138), 373.

Liston, G. E., Heimstra, C. A., Elder, K., & Cline, D. W. (2008). Mesocell study area snow distributions for the Cold Land Processes Experiment (CLPX). *Journal of hydrometeorology, 9*(5), 957.

Liston, G. E., McFadden, J. P., Sturm, M., & Pielke, R. A. s. (2002). Modelled changes in arctic tundra snow, energy and moisture fluxes due to increased shrubs. *Global change biology, 8*(1), 17.

Liston, G. E., & Sturm, M. (1998). A snow-transport model for complex terrain. *Journal of Glaciology, 44*(148), 498.

Liston, G. E., & Sturm, M. (2002). Winter precipitation patterns in arctic Alaska determined from a blowing-snow model and snow-depth observations. *Journal of hydrometeorology, 3*(6), 646.

Liston, G. E., & Winther, J. G. (2005). Antarctic surface and subsurface snow and ice melt fluxes. *Journal of Climate, 18*(10), 1469.

Liston, G. E., Winther, J. G., Bruland, O., Elvehøy, H., Sand, K., & Karlöf, L. (2000). Snow and blue-ice distribution patterns on the coastal Antarctic ice sheet. *Antarctic science, 12*(01), 69.

Malå Geoscience. (2012). Malå GPR ProEx System. Retrieved 20.11.2012, from http://www.malags.com/Products/MALA-ProEx-System

Marchand, W. D., Bruland, O., & Killingtveit, Å. (2001). Improved Measurements and Analysis of Spatial Snow Cover by Combining a Ground Based Radar System With a Differential Global Positioning System Reciever. *Nordic Hydrology, 32*(3), 13.

Marks, D., Domingo, J., Susong, D., Link, T., & Garen, D. (1999). A spatially distributed energy balance snowmelt model for application in mountain basins. *Hydrological processes, 13*(12-13), 1935-1959.

Marsh, P. (1999). Snowcover formation and melt: recent advances and future prospects. *Hydrological processes, 13*(14-15), 2117.

Matsuoka, K., Aoki, T., Yamamoto, T., & Naruse, R. (2003). Field-performance tests of a portable low frequency ice-penetrating radar and a ground-penetrating radar at Athabasca Glacier, Canadian Rockies. *Bulletin of Glaciological Research, 20*, 6.

Mernild, S. H., Liston, G. E., Hiemstra, C. A., Christensen, J. H., Stendel, M., & Hasholt, B. (2011). Surface Mass Balance and Runoff Modeling Using HIRHAM4 RCM at Kangerlussuaq (Sondre Stromfjord), West Greenland, 1950-2080. *Journal of Climate, 24*(3), 609-623.

Mernild, S. H., Liston, G. E., Steffen, K., & Chylek, P. (2010). Meltwater flux and runoff modeling in the ablation area of Jakobshavn Isbræ, West Greenland. *Journal of Glaciology, 56*(195), 20.

Mernild, S. H., Liston, G. E., van den Broeke, M., & Hasholt, B. (2010). Runoff and mass-balance simulations from the Greenland Ice Sheet at Kangerlussuaq (Søndre Strømfjord) in a 30-year perspective, 1979-2008. *The Cryosphere, 4*(2), 231.

met.no. (2012). Observing stations in operation. Retrieved 22.11.2012, from eklima.no

Mott, R., Schirmer, M., Bavay, M., Grünewald, T., & Lehning, M. (2010). Understanding snow-transport processes shaping the mountain snow-cover. *The Cryosphere, 4*(4), 545.

Onset. (2012). Onset Computer Corporation. Retrieved 22.11.2012, from http://www.onsetcomp.com

Pomeroy, J. W., & Gray, D. M. (1990). Saltation of Snow. *Water Resources Research, 26*(7), 11.

Prasad, R., Tarboton, D. G., Liston, G. E., & Luce, C. H. (2001). Testing a blowing snow model against distributed snow measurements at Upper Sheep Creek, Idaho, United States of America. *Water resources research, 37*(5), 1341.

Reynolds, J. M. (2011). *An Introduction to Applied and Environmental Geophysics*.

Richardson, C., Aarholt, E., Hamran, S. E., Holmlund, P., & Isaksson, E. (1997). Spatial distribution of snow in western Dronning Maud Land, East Antarctica, mapped by a ground-based snow radar. *Journal of Geophysical Research, 102*(B9), 11.

Sand, K., & Bruland, O. (1998). Application of Georadar for Snow Cover Surveying. *Nordic Hydrology, 29*(4/5), 9.

Sandmeier Scientific Software. (2012). Reflexw. Retrieved 20.11.2012, from http://www.sandmeier-geo.de

seNorge.no. (2013). Snow, weather, water and climate in Norway. Retrieved 28.03.2013, from www.senorge.no

Serma, A. I. A., & Setan, H. (2009). Ground Penetrating Radar (GPR) for Subsurface Mapping: Preliminary Result. *Geoinformation Science Journal, 9*(2), 18.

Sinisalo, A., Grinsted, A., Moore, J. C., Kärkäs, E., & Pettersson, R. (2003). Snow-Accumulation studies in Antarctica with ground-penetrating radar using 50, 100 and 800 antenna frequencies. *Annals of Glaciology, 37*, 5.

Store Norske Leksikon. (2012). Hardangervidda. Retrieved 20.02.2013, from http://snl.no/Hardangervidda

Sømme, L., & Østbye, E. (1997). Høyfjellsøkologisk forskningsstasjons historie. *Finse - Et senter for høyfjellsforskning*, 56.

Tabler, R. D. (1975a). Estimating the transport and evaporation of blowing snow. *Research Committee Great Plains Agricultural Council, 73*, 85-104.

Tabler, R. D. (1975b). *Predicting Profiles Of Snowdrifts in Topographic Catchments*. Paper presented at the Western Snow Conference, Coronado, California.

Tarboton, D. G., Chowdhury, T. G., & Jackson, T. H. (1994). A Spatially Distributed Energy Balance Snowmelt Model. *Proceedings of Symposium in Biogeochemestry of Seasonally Snow Covered Catchments*.

Taurisano, A., Schuler, T. V., Hagen, J. O., Eiken, T., Loe, E., Melvold, K., & Kohler, J. C. (2007). The distribution of snow accumulation across the Austfonna ice cap, Svalbard: direct measurements and modelling. *Polar Research, 26*, 6.

Uematsu, T., Nakata, T., Takeuchi, K., Arisawa, Y., & Kaneda, Y. (1991). Three-dimensional numerical simulation of snowdrift. *Cold regions science and technology, 20*(1), 65-73.

Winstral, A., Marks, D., & Gurney, R. (2013). Simulating wind-affected snow accumulations at catchment to basin scales. *Advances in Water Resources, 55*, 15.

Yamamoto, T., Matsuoka, K., & Naruse, R. (2004). Observation of internal structures of snow covers with a ground-penetrating radar. *Annals of Glaciology, 38*, 4.

Yang, D., Goodison, B. E., Metcalfe, J. R., Golubev, V. S., Bates, R., Pangburn, T., & Hanson, C. L. (1996). Accuracy of NWS 8" Standard Nonrecording Precipitation Gauge: Results and Application of WMO Intercomparison. *Journal of atmospheric and oceanic technology, 15*(1), 54.

Zhang, Y., Suzuki, K., Kadota, T., & Ohata, T. (2004). Sublimation from snow surface in southern mountain taiga of eastern Siberia. *Journal of Geophysical Research, 109*, 10.

Appendix A – GPR implementation

A.1 Theory

Ground penetrating radar (GPR) offers a method of performing large scale snow depth measurements efficiently, while being able to measure snow depth down to $10\,m$ without disturbing more than $20\,cm$ of top snow (Jaedicke, 2003; Dunse et al., 2008). It is considered the best way of studying the spatial variability of snow cover with a high temporal resolution (Yamamoto et al., 2004). GPR has been used to successfully measure snow cover distributions for many years (Evans, 1965) and around the world: Japan (Yamamoto et al., 2004); Greenland (Dunse et al., 2008); and Antarctica (Richardson et al., 1997) among others. Several successful implementations have been performed in mainland Norway by Kohler et al. (1997), Sand and Bruland (1998), and Marchand et al. (2001).

A GPR system consists of an antenna and a receiver that emits electromagnetic (EM) waves into the ground and records the time of receiving the reflected signal (Jaedicke, 2003). The velocity of the radio waves through the ground material along with the recorded travel time can be used to calculate the travel distance of the signal. The velocity of radio waves V_m $[m\ s^{-1}]$ through any medium is described by Equation 32 (Reynolds, 2011).

$$V_m = c/\left\{\left(\frac{\mathcal{E}_r\mu_r}{2}\right)[(1+\sigma/(2\pi f\mathcal{E}_r\mathcal{E}_0))^2+1]\right\}^{\frac{1}{2}} \qquad \text{Equation 32}$$

Here, $c = 299.8 * 10^8\ m\ s^{-1}$ is the speed of light in a vacuum, μ_r $[H\ m^{-1}]$ is the relative magnetic permeability ($\mu_r = 1$ for non-magnetic materials), σ $[S\ m^{-1}]$ is the conductivity of the material, f $[Hz]$ is the frequency of the antenna, $\mathcal{E}_r$ [1] is the dielectric constant, and $\mathcal{E}_0$ $[F\ m^{-1}]$ is the permittivity of free space (given as $8.854 * 10^{-12}\ F\ m^{-1}$). Snow and ice have an extremely low the conductivity (σ) and is non-magnetic ($\mu_r = 1$) (Davis and Annan, 1989; Kovacs et al., 1995; Reynolds, 2011), and we can therefore simplify Equation 32 to

$$V_m = \frac{c}{\sqrt{\mathcal{E}_r}}. \qquad \text{Equation 33}$$

As c is constant, the relative dielectric constant $\mathcal{E}_r$ controls velocity. The contrast in $\mathcal{E}_r$ between materials facilitates reflection of radio waves, with greater contrast giving a higher

degree of reflection. When a radio wave travels through material 1 and meets material 2, the amount of energy reflected is given by

$$R = \frac{\sqrt{\mathcal{E}_2} - \sqrt{\mathcal{E}_1}}{\sqrt{\mathcal{E}_2} + \sqrt{\mathcal{E}_1}}. \quad \text{Equation 34}$$

An increased $\mathcal{E}_2$ (lower layer) relative to $\mathcal{E}_1$ (upper layer) will give more reflected energy returned to the receiver. Generally, the dielectric constant of materials will increase with depth (Reynolds, 2011). The objective of this GPR study is to precisely measure the distance between the antenna and the snow-ground interface. The difference in $\mathcal{E}_r$ between snow and ground is higher than the dielectric differences between layers in the snow (Yamamoto et al., 2004). Therefore, the strongest reflection will be from the ground (Marchand et al., 2001). The two-way travel time t $[s]$ is the time spent from emission through reflection and back to the antenna. If an average speed V_m of the radio waves is calculated, then the travel distance D $[m]$ of the waves can be calculated from the two-way travel time using Equation 33:

$$V_m = \frac{2D}{t} \Rightarrow D = \frac{tV_m}{2} = \frac{tc}{2\sqrt{\mathcal{E}_r}} \quad \text{Equation 35}$$

As t is measured by the equipment, D relies on the ability to estimate a representative V_m or $\mathcal{E}_r$ for the snow pack (Kovacs et al., 1995). Measuring the dielectric constant $\mathcal{E}_r$ for snow – a mixture of air and ice – is very difficult, although many studies have attempted to do so (Evans, 1965; Galley et al., 2009). It also varies greatly according to snow density. For this study we will estimate $\mathcal{E}_r$ using the empirical formula from Kovacs et al. (1995). Their method describes an empirical equation for determining the relative dielectric constant as a function of the density of a snow pack. Equation 36 states the simple and robust relationship between the density ρ $[kg\ m^{-3}]$ and the dielectric constant $\mathcal{E}_r$ (Kovacs et al., 1995).

$$\mathcal{E}_r = (1 + 0.845\rho)^2 \quad \text{Equation 36}$$

Snow density measurements were performed at three locations within the Finse study area to provide representative data for ρ. A limitation to Equation 36 is its dependence on a dry snow pack (Marchand et al., 2001).

Unless the free water content is known or the snow is dry, the only practical method of estimating V_m for wet snow is to do stationary depth measurements with a known reflection

surface, and thereby calculate the speed V_m using trace times t and the measured depth D between the snow surface and the reflection surface (Marchand et al., 2001). For this study, all field work was performed at times when the snow pack was dry, making the empirical relationship of Kovacs et al. (1995) applicable for all datasets. The density and the results of the velocity calculations are found in Appendix D.

A.2 GPR equipment and parameters

GPR data was collected using the commercial radar system RAMAC (ProEx) from Malå Geoscience (Malå Geoscience, 2012), operating with a shielded antennae at $800\ Hz$. $800\ Hz$ is an optimal system frequency for studying snow, as it is a good compromise between resolution and penetration depth (Yamamoto et al., 2004). The shielded antenna is not prone to interference from nearby metal objects, and can therefore be pulled close behind the snowmobile (Figure 42) (Sinisalo et al., 2003). This specific system has been thoroughly tested for measuring glacial and ground based snow cover in Canada (Matsuoka et al., 2003), Japan (Yamamoto et al., 2004), Svalbard (Taurisano et al., 2007) , Greenland (Dunse et al., 2008) and Antarctica (Sinisalo et al., 2003). The system includes a signal processor and a computer with screen for data storage, on site viewing of collected data and adjustment of system parameters. A global positioning system (GPS) receiver from Garmin connected to the computer will give continuous positioning data synchronized with the GPR measurements. Measurements were recorded at intervals of $0.25\ s$, coupled with positioning data. The complete set of data acquisition parameters are found in Table 7.

Table 7 – Parameters used in GPR logger.

Parameter	Value
Antenna	$800\ Hz$ shielded
Sample type	Time triggering
Logging interval	$0.25\ s$
Speed	220
Sample Frequency	9527
Time window	$132\ ns$
Stacks	8

A.3 Processing

The processing software used was Reflexw by Sandmeier Scientific Software (Sandmeier Scientific Software, 2012). Processing involved converting the two-way travel time to actual snow depth. This also involved several steps to increase the contrast of return signals making

the strongest return signal more easily detectable, and the manual tracing more robust. The first step was a static correction where the first return of the signal was shifted to match the snow surface position. Afterwards, 3 filters were applied to increase the signal-to-noise ratio: (1) a Butterworth bandpass filter for noise removal, with cutoffs at approximately 300 Hz to 1300 Hz; (2) a mean subtraction-filter (dewow) for correction of low frequency and direct current bias in data; and (3) a 2D background removal to improve the signal to noise ratio (Serma and Setan, 2009). A linear gain adjustment was applied when needed. Reflexw creates the connection between individual GPR and GPS data points, along with UTM coordinate calculations. Reflection traces were then picked manually. When finished, the picked two-way-travel times were converted into depths using the signal velocity V_m derived from Equation 36 and Equation 33 using the observed snow density ρ (Kovacs et al., 1995).

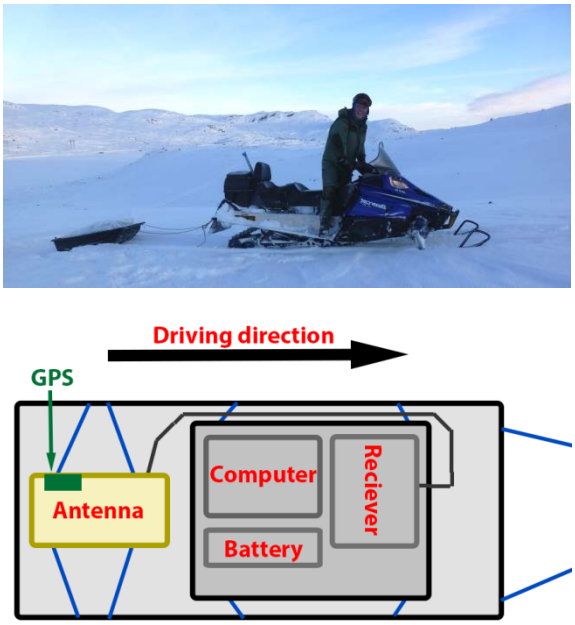

Figure 42 – Picture of the snowmobile with sled, December 2012, and a top-down schematic of the GPR equipment mounted in the sled. Computer, battery and receiver are inside a waterproof casing. GPS and antenna are self contained and waterproof. (photo: Torbjørn Østby)

Appendix B – Station construction

Station rigs were made from scratch in the department workshop (Figure 43) and installed in November 2011 (Figure 44). The stations are placed so they represent the variation in topography of the terrain, while still maintaining a proximity to the GPR-domain. The area experiences a lot of snow during the winter, and a limiting factor for placing the stations is the risk of being buried in snow.

Figure 43 – Tobias Litherland making the meteorological station rigs in the workshop at the University of Oslo, October 2011 (photo: Kjersti Gisnås).

All predetermined locations for weather stations were deemed acceptable and stations where installed at locations displayed in Figure 2 and Figure 6. Figure 45 shows the schematics of the station rigs, with the dimensions of the equipment used. Figure 46 shows pictures of each station.

Figure 44 – Kjersti Gisnås and Tobias Litherland installing Station B in the field in November 2011 (photo: Bas Altena).

The winter of 2011 and 2012 experienced storms with hurricane winds during early winter, without the stations taking any noticeable harm. In late winter 2012, the SnowPack in the study area had increased to a depth of over $2\,m$. The slight incline of the ground around Stations A and B produced snow creep which exerted a heavy force on the installations. The strain broke several wires on each station, luckily without the aluminium rods taking any detectable toll. During the late summer of 2012, all wires where redone and fastened better. In March 2012, Station A was elongated before to account for snow depths almost exceeding its initial height. The same was

done for Station B in October 2012. The final height, position and elevation of the stations can be found in Table 1. Permission to install and operate these specific stations was granted by the municipality council of Ulvik, Hordaland, for the time period of 2011 through 2015.

Table 8 shows the array of meteorological sensors installed on the stations. Sensors were tested on Blindern campus prior to field installation, to ensure they were all functioning (Figure 47). All sensors are acquired from the HOBO series by Onset Computer Corporation Inc (Onset, 2012).

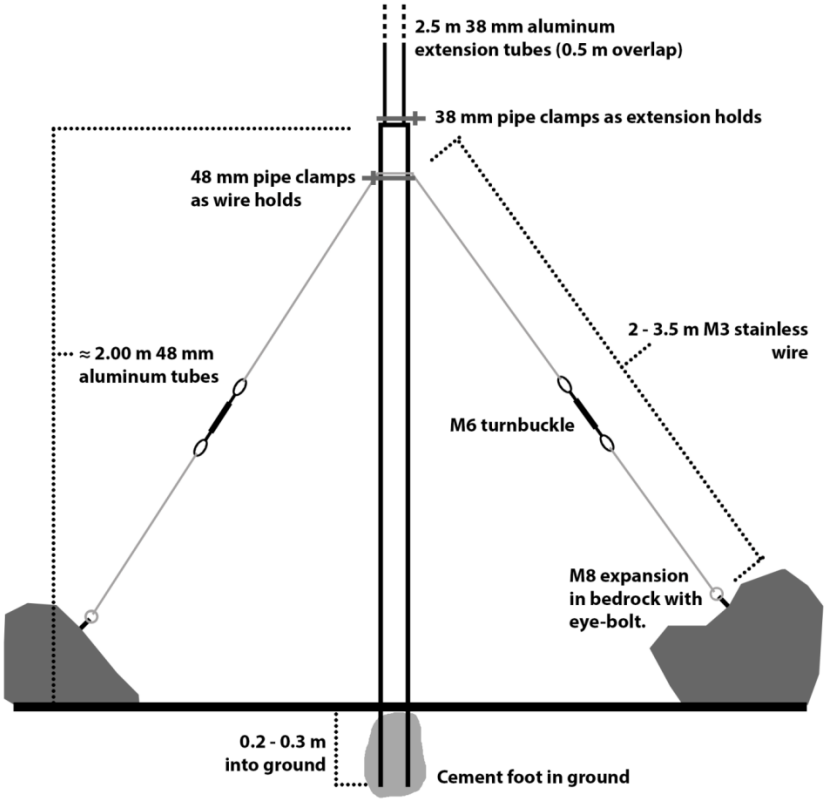

Figure 45 – Schematic of the weather station base used for all 3 meteorological stations. Each station is fastened with 3 wires anchored to the ground.

A

B

C

Figure 46 – Pictures of the installed meteorological stations. Pictures A, B and C show Station A, B and C respectively. (photos by: A - Tobias Litherland, B - Kjersti Gisnås, C - Tobias Litherland)

Table 8 – Meteorological sensors installed at weather stations. All equipment is from the HOBO series by Onset Computer Systems.

	Station A	Station B	Station C
Logger	H21-002	H21-002	U30-NRC-SYS-B
Wind speed/dir	S-WSET-A	S-WSET-A	U30-NRC-SYS-B
Temp/Humid	S-THB-M002	S-THB-M002	U30-NRC-SYS-B
Radiation	None	None	2 pyranometer S-LIB-M003

Figure 47 – Testing meteorological sensors at Blindern Campus, University of Oslo. (photo: Tobias Litherland)

Appendix C – SnowModel default parameters

The below model parameters are the ones used for the default run of SnowModel for the winter season of 2011 to 2012. Parameters are equal to the ones used for the 2012 to 2013 simulation, with the exception of the dates. Variable names correspond to the names in the snowmodel.par initiation file in SnowModel.

```
nx = 2500
ny = 1000
deltax = 4.0
deltay = 4.0
xmn = 415047.1009
ymn = 6714424.238
dt = 3600.0
iyear_init = 2011
imonth_init = 10
iday_init = 1
xhour_init = 0.0
max_iter = 5856
isingle_stn_flag = 0
igrads_metfile = 0
undef = -9999.0
ascii_topoveg = 1.0
veg_shd_25 = 0.10
veg_shd_26 = 0.10
veg_shd_27 = 0.10
veg_shd_28 = 0.10
veg_shd_29 = 0.10
veg_shd_30 = 0.10
const_veg_flag = 15.0
iveg_ht_flag = 0
xlat = 60.0
lat_solar_flag = 0
UTC_flag = 0.0
run_micromet = 1.0
run_enbal = 1.0
run_SnowPack = 1.0
run_snowtran = 1.0
irun_corr_factor = 0
ihrestart_flag = -2
i_dataassim_loop = 1
ihrestart_inc = 0
print_user = 1.0
iprint_inc = 24
i_tair_flag = 1
i_rh_flag = 1
i_wind_flag = 1
i_solar_flag = 1
i_longwave_flag = 1
i_prec_flag = 1
ifill = 1
iobsint = 0
dn = 1.0
barnes_lg_domain = 0.0
n_stns_used = 5
curve_len_scale = 100.0
slopewt = 0.58
curvewt = 0.42
windspd_min = 1.0
lapse_rate_user_flag = 0
iprecip_lapse_rate_user_flag = 0
calc_subcanopy_met = 1.0
gap_frac = 0.2
cloud_frac_factor = 1.0
use_shortwave_obs = 0.0
use_longwave_obs = 0.0
use_sfc_pressure_obs = 0.0
print_micromet = 0.0
Utau_t_flag = 1.0
Utau_t_const = 0.25
subgrid_flag = 0.0
erosion_dist = 0.0
tp_scale = 1.0
tabler_dir = 270.0
slope_adjust = 1.0
twolayer_flag = 1.0
bc_flag = 1.0
ht_windobs = 10.0
ht_rhobs = 2.0
ro_snow = 300.0
snow_d_init_const = 0.0
topoflag = 1.0
print_snowtran = 0.0
icond_flag = 0
albedo_snow_forest = 0.45
albedo_snow_clearing = 0.60
albedo_glacier = 0.40
print_enbal = 0.0
sfc_sublim_flag = 1.0
print_SnowPack = 0.0
multilayer_SnowPack = 0
tsls_threshold = 24.0
max_layers = 6
dz_snow_min = 0.001
print_multilayer = 0.0
izero_snow_date = 999999
```

Appendix D – Snow density data

Following is the complete set of density data from the snow pit surveys. Average density is calculated as the weighted average of each profile with regards to each profiles depths (deeper profile counts more towards total density). Average signal velocity is calculated by Equation 33 and Equation 36.

December 17. 2011

Tube length:	20.00 cm			
Tube volume:	500.00 cm^3	Average density [$g\ cm^{-3}$]:		0.31
Bag weight:	30.00 g	Average velocity acc. to Kovacs (1995) [$m\ ns^{-1}$]		0.24
Station A	Profile 1			
Start [cm]	Stop [cm]	Column length [cm]	Weight w/o bag [g]	Density [gcm^{-3}]
34.50	14.50	20.00	150.00	0.30
14.50	0.00	14.50	170.00	0.47
			Aver. density [$g\ cm^{-3}$]:	0.37
Station A	Profile 2			
34.00	14.00	20.00	145.00	0.29
14.00	0.00	14.00	180.00	0.51
			Aver. density [$g\ cm^{-3}$]:	0.38
Station B	Profile 1			
58.00	38.00	20.00	90.00	0.18
38.00	18.00	20.00	140.00	0.28
18.00	2.00	16.00	130.00	0.33
			Aver. density [$g\ cm^{-3}$]:	0.26
Station B	Profile 2			
61.00	41.00	20.00	100.00	0.20
41.00	21.00	20.00	140.00	0.28
21.00	2.00	19.00	150.00	0.32
			Aver. density [$g\ cm^{-3}$]:	0.26

January 30. 2012

Tube length:	20.00 cm			
Tube volume:	500.00 cm^3	Average density [$g\ cm^{-3}$]:		0.38
Bag weight:	30.00 g	Average velocity acc. to Kovacs (1995) [$m\ ns^{-1}$]:		0.24
Station A	Profile 1			
Start [cm]	Stop [cm]	Column length [cm]	Weight w/o bag [g]	Density [gcm^{-3}]
141.00	121.00	20.00	100.00	0.20
121.00	101.00	20.00	155.00	0.31
101.00	81.00	20.00	180.00	0.36
81.00	61.00	20.00	185.00	0.37
61.00	41.00	20.00	205.00	0.41
41.00	21.00	20.00	230.00	0.46
21.00	1.00	20.00	255.00	0.51
			Aver. density [$g\ cm^{-3}$]:	0.37
Station A	Profile 2			
122.00	102.00	20.00	150.00	0.30
102.00	82.00	20.00	160.00	0.32
82.00	62.00	20.00	170.00	0.34
62.00	42.00	20.00	180.00	0.36
42.00	22.00	20.00	210.00	0.42
22.00	2.00	20.00	240.00	0.48
			Aver. density [$g\ cm^{-3}$]:	0.37
Station B	Profile 1			
137.00	117.00	20.00	145.00	0.29
117.00	97.00	20.00	175.00	0.35
97.00	77.00	20.00	195.00	0.39
77.00	57.00	20.00	225.00	0.45
57.00	37.00	20.00	180.00	0.36
37.00	17.00	20.00	210.00	0.42
17.00	0.00	17.00	210.00	0.49
			Aver. density [$g\ cm^{-3}$]:	0.39
Station B	Profile 2			
140.00	120.00	20.00	140.00	0.28
120.00	100.00	20.00	175.00	0.35
100.00	80.00	20.00	180.00	0.36
80.00	60.00	20.00	230.00	0.46
60.00	40.00	20.00	195.00	0.39
40.00	20.00	20.00	230.00	0.46
20.00	0.00	20.00	215.00	0.43
			Aver. density [$g\ cm^{-3}$]:	0.39

February 27. 2012

Tube length:	20.00 cm			
Tube volume:	500.00 cm^3	Average density [$g\ cm^{-3}$]:		–
Bag weight:	30.00 g	Average velocity acc. to Kovacs (1995) [$m\ ns^{-1}$]		–
Station A	Profile 1			
Start [cm]	Stop [cm]	Column length [cm]	Weight w/o bag	Density [g/cm^3]
–	–	–	–	–
			Aver. density [$g\ cm^{-3}$]:	–
Station A	Profile 2			
–	–	–	–	–
			Aver. density [$g\ cm^{-3}$]:	–
Station B	Profile 1			
–	–	–	–	–
			Aver. density [$g\ cm^{-3}$]:	–
Station B	Profile 2			
–	–	–	–	–
			Aver. density [$g\ cm^{-3}$]:	–

March 22. 2012

Tube length:	20.00 cm			
Tube volume:	500.00 cm^3	Average density [$g\ cm^{-3}$]:		0.45
Bag weight:	30.00 g	Average velocity acc. to Kovacs (1995) [$m\ ns^{-1}$]:		0.30
Station A				
Start [cm]	Stop [cm]	Column length [cm]	Weight w/o bag	Density [gcm^{-3}]
227.00	207.00	20.00	230.00	0.46
207.00	187.00	20.00	250.00	0.50
187.00	167.00	20.00	240.00	0.48
167.00	147.00	20.00	270.00	0.54
147.00	127.00	20.00	230.00	0.46
127.00	107.00	20.00	230.00	0.46
107.00	87.00	20.00	220.00	0.44
87.00	67.00	20.00	220.00	0.44
67.00	47.00	20.00	280.00	0.56
47.00	27.00	20.00	260.00	0.52
27.00	7.00	20.00	250.00	0.50
7.00	0.00	7.00	120.00	0.69
			Aver. density [$g\ cm^{-3}$]:	0.47
Near research station				
200.00	180.00	20.00	245.00	0.49
180.00	160.00	20.00	225.00	0.45
160.00	140.00	20.00	225.00	0.45
140.00	120.00	20.00	235.00	0.47
120.00	100.00	20.00	250.00	0.50
100.00	80.00	20.00	230.00	0.46
80.00	60.00	20.00	235.00	0.47
60.00	40.00	20.00	230.00	0.46
40.00	20.00	20.00	240.00	0.48
20.00	0.00	20.00	260.00	0.52
			Aver. density [$g\ cm^{-3}$]:	0.29
Hill near research station				
167.00	147.00	20.00	0.34	6.80
147.00	127.00	20.00	0.39	7.80
127.00	107.00	20.00	0.44	8.80
107.00	87.00	20.00	0.36	7.20
87.00	67.00	20.00	0.40	8.00
67.00	47.00	20.00	0.38	7.60
47.00	27.00	20.00	0.40	8.00
27.00	7.00	20.00	0.38	7.60
7.00	0.00	7.00	0.34	2.37
			Aver. density [$g\ cm^{-3}$]:	0.38

December 12. 2012

Tube length:	20.00 cm			
Tube volume:	500.00 cm^3	Average density [$g\ cm^{-3}$]:		0.34
Bag weight:	30.00 g	Average velocity acc. to Kovacs (1995) [$m\ ns^{-1}$]:		0.23
Station A	Profile 1			
Start [cm]	Stop [cm]	Column length [cm]	Weight w/o bag [g]	Density [gcm^{-3}]
102.00	82.00	20.00	65.00	0.13
82.00	62.00	20.00	150.00	0.30
62.00	42.00	20.00	200.00	0.40
42.00	22.00	20.00	220.00	0.44
22.00	2.00	20.00	240.00	0.48
2.00	0.00	2.00	–	–
			Aver. density [$g\ cm^{-3}$]:	0.35
Station A	Profile 2			
108.00	88.00	20.00	55.00	0.11
88.00	68.00	20.00	175.00	0.35
68.00	48.00	20.00	188.00	0.38
48.00	28.00	20.00	215.00	0.43
28.00	8.00	20.00	220.00	0.44
8.00	0.00	8.00	125.00	0.63
			Aver. density [$g\ cm^{-3}$]:	0.36
Station B	Profile 1			
58.00	38.00	20.00	65.00	0.13
38.00	18.00	20.00	150.00	0.30
18.00	0.00	18.00	200.00	0.44
			Aver. density [$g\ cm^{-3}$]:	0.29
Station B	Profile 2			
52.00	32.00	20.00	55.00	0.11
32.00	12.00	20.00	175.00	0.35
12.00	0.00	12.00	188.00	0.63
			Aver. density [$g\ cm^{-3}$]:	0.32

January 22. 2013

Tube length:	20.00 cm			
Tube volume:	500.00 cm^3	Average density [$g\ cm^{-3}$]:		0.31
Bag weight:	30.00 g	Average velocity acc. to Kovacs (1995) [$m\ ns^{-1}$]:		0.24
Station A	Profile 1			
Start [cm]	Stop [cm]	Column length [cm]	Weight w/o bag [g]	Density [gcm^{-3}]
80.00	60.00	20.00	120.00	0.24
60.00	40.00	20.00	150.00	0.30
40.00	20.00	20.00	190.00	0.38
20.00	0.00	20.00	150.00	0.30
			Aver. density [$g\ cm^{-3}$]:	0.31
Station A	Profile 2			
71.00	51.00	20.00	130.00	0.26
51.00	31.00	20.00	155.00	0.31
31.00	11.00	20.00	170.00	0.34
11.00	0.00	20.00	60.00	0.22
			Aver. density [$g\ cm^{-3}$]:	0.29
Station B	Profile 1			
94.00	74.00	20.00	130.00	0.30
74.00	54.00	20.00	155.00	0.28
54.00	34.00	20.00	200.00	0.32
34.00	14.00	20.00	190.00	0.38
10.50	0.00	10.50	120.00	0.34
			Aver. density [$g\ cm^{-3}$]:	0.32
Station B	Profile 2			
94.00	74.00	20.00	150.00	0.30
74.00	54.00	20.00	145.00	0.29
54.00	34.00	20.00	190.00	0.38
34.00	14.00	20.00	150.00	0.30
12.00	0.00	12.00	110.00	0.37
			Aver. density [$g\ cm^{-3}$]:	0.32

February 25. 2013

Tube length:	20.00 cm			
Tube volume:	500.00 cm^3	Average density [$g\ cm^{-3}$]:		0.33
Bag weight:	30.00 g	Average velocity acc. to Kovacs (1995) [$m\ ns^{-1}$]:		0.23
Station A	Profile 1			
Start [cm]	Stop [cm]	Column length [cm]	Weight w/o bag [g]	Density [gcm^{-3}]
97.00	77.00	20.00	175.00	0.35
77.00	57.00	20.00	170.00	0.34
57.00	37.00	20.00	170.00	0.34
37.00	17.00	20.00	185.00	0.37
17.00	0.00	17.00	185.00	0.44
			Aver. density [$g\ cm^{-3}$]:	0.36
Station A	Profile 2			
99.00	79.00	20.00	175.00	0.35
79.00	59.00	20.00	170.00	0.34
59.00	39.00	20.00	170.00	0.34
39.00	19.00	20.00	185.00	0.37
19.00	0.00	19.00	185.00	0.39
			Aver. density [$g\ cm^{-3}$]:	0.36
Station B	Profile 1			
97.00	77.00	20.00	130.00	0.26
77.00	57.00	20.00	155.00	0.31
57.00	37.00	20.00	200.00	0.40
37.00	17.00	20.00	190.00	0.38
17.00	0.00	17.00	120.00	0.28
			Aver. density [$g\ cm^{-3}$]:	0.33
Station B	Profile 2			
99.00	79.00	20.00	130.00	0.26
79.00	59.00	20.00	145.00	0.29
59.00	39.00	20.00	145.00	0.29
39.00	19.00	20.00	145.00	0.29
19.00	0.00	19.00	145.00	0.31
			Aver. density [$g\ cm^{-3}$]:	0.29

March 20. 2013

Tube length:	20.00 cm			
Tube volume:	500.00 cm^3	Average density [$g\ cm^{-3}$]:		0.34
Bag weight:	30.00 g	Average velocity acc. to Kovacs (1995) [$m\ ns^{-1}$]:		0.23
Station A	Profile 1			
Start [cm]	Stop [cm]	Column length [cm]	Weight w/o bag [g]	Density [gcm^{-3}]
120.00	100.00	20.00	179.00	0.36
100.00	80.00	20.00	165.00	0.33
80.00	60.00	20.00	175.00	0.35
60.00	40.00	20.00	170.00	0.34
40.00	20.00	20.00	175.00	0.35
20.00	0.00	20.00	150.00	0.30
			Aver. density [$g\ cm^{-3}$]:	0.34

Appendix E – Correspondence

E.1 Email from Glen Liston, 20.09.2012

Title: RE: Questions regarding a study in Norway using SnowModel

Dear Tobias,

I have a note about your poster. In it you indicate you have a 1-km by 1-km domain, with a 250-m grid increment, or 16 grid cells. I regularly run the model with 1 million grid cells (1,000,000) or a domain that is 1000 grid cells by 1000 grid cells. And the grid cell size can range from 10-m to 10-km, depending on the processes you want to represent. If blowing snow is important in your domain, like in an alpine area, then you probably want to run the model with a 10-m to 100-m grid increment. A 30-m grid cell size works pretty well, but really anything is possible.

Also note that if blowing snow is an important physical process in your domain, then you should have a 2 to 3 km boundary along all sides of your domain (or at the upwind sides at least) in order to eliminate any boundary effects from influencing the simulation in the area of interest. With this, even if you are only really interested in a 1-km area, your total simulation domain will need to be 5-km by 5-km.

To bring you up to speed on my models, I have 7 recent papers that describe the latest version of my snow-evolution modeling system. They can be found on my anonymous ftp site:

ftp://ftp.cira.colostate.edu/liston/papers/first_author/

2006a.liston.JHM.pdf (MicroMet)
2006b.liston.JHM.pdf (SnowModel)
2007.liston.JGLAC.pdf (latest version of SnowTran-3D)
2008a.liston.JHM.pdf (SnowAssim)
2008b.liston.JHM.pdf (Example Application)
2011a.liston.JCLIM.pdf (Example Application)
2011b.liston.JCLIM.pdf (Example Application)

These last three papers provide a nice summary of applications of the entire collection of models, while the other papers provide details of each individual modeling component.

The MicroMet/SnowModel code, etc., is available from this anonymous ftp server:

ftp://gliston.cira.colostate.edu/micromet_SnowModel/

You want the latest version.

Before using the model I encourage you to read the "readme_first.txt" file and all of the *.txt files in the "docs/" directory in the above distribution. And you should also read the SnowModel.par file.

Then, I would try to reproduce the example simulation in the distribution. Once you can do this, and when you have read everything listed above, you should have a pretty good idea of what you need to do to run your own

simulations.

Usually the hardest part of all of this is getting a Fortran 77 compiler working on your computer.

Good luck, and feel free to contact me if you have any questions.

Glen

~~~~~~
Glen E. Liston, Ph.D.
  Cooperative Institute for Research in the Atmosphere (CIRA)
  Colorado State University
  Fort Collins, CO 80523-1375

Email: glen.liston@colostate.edu
Voice: (970)491-8220; FAX: (970)491-8241
~~~~~~

-----Original Message-----
From: Tobias Litherland [mailto:tobiasli@student.geo.uio.no]
Sent: Friday, September 07, 2012 7:02 AM
To: Liston,Glen
Cc: thomas Vikhamar Schuler
Subject: Questions regarding a study in Norway using SnowModel

Hello Mr. Liston,

I am a master student at the University of Oslo planning on doing a study on snow distributions in alpine Norway using SnowModel. The study is part of a larger project on permafrost at UiO called CryoMet. The aim of my study is to do a thorough test of SnowModel's ability to follow intra-seasonal variations in snow cover. To do this, we are collecting a two-year monthly set of GPR over a grid at Finse, Norway. This data will be used for calibration and validation of SnowModel's performance.

Next week I will be attending the 2nd Conference on Modelling Hydrology, Climate and Land Surface Processes at Lillestrøm, Norway. I will be presenting a poster showing preliminary results and project outline, with a short description of SnowModel. The poster is attatched to this email.

May I ask your permission to use SnowModel in this study, to acknowledge you in this poster, and note you as a co-author in any resulting work?

We have not started using SnowModel yet, but hope to start working in about a weeks time.

If you have any questions or suggestions, please contact either myself or my supervisor Thomas V. Schuler (t.v.schuler@geo.uio.no).

I hope to hear from you.

Regards,
Tobias Litherland
tobiasli@student.matnat.uio.no

E.2 Email from Glen Liston, 03.04.2013

Title: RE: Questions regarding SnowModel

RE: Questions regarding SnowModel

Dear Tobias,

It is good to hear from you! Sorry I have been so slow in returning your email.

1) You are right, your question 1) is not implemented anymore in the model (it didn't seem to make any difference in my simulations). The snow density and snow transport threshold is modified as a function of wind speed and transport. See surface_snow_1 and 2 subroutines.

2) The largest domain I have run is 9000 x 6000 grid cells. This requires a workstation with about 25 GB of memory set up with a similar amount of swap space. Whether I use hourly or daily time steps also makes a big difference in how long the simulations take!

As a check, my workstation gives me the following (see the CPU calculation below):

Computational requirements (e.g., CPU time and memory) increase linearly with the number of grid cells and time steps.

nx = number of grid cells in x-direction
ny = number of grid cells in y-direction
nt = number of time steps in the simulation

CPU time (in hours) = 2.74x10-9 * nx * ny * nt

Examples:
nx = 1000, ny = 1000, nt = 365, takes ~1 hour CPU time.
nx = 1000, ny = 1000, nt = 365*24, takes ~1 day CPU time.
nx = 700, ny = 700, nt = 365*8*30, takes ~5 days CPU time.

Let me know if you have any other questions. I will have some email access in my field camp over the next few weeks!

Sincerely,
Glen

~~~~~~
Glen E. Liston, Ph.D.
Cooperative Institute for Research in the Atmosphere (CIRA)
Colorado State University
Fort Collins, CO 80523-1375

Email: glen.liston@colostate.edu
Voice: (970)491-8220; FAX: (970)491-8241
~~~~~~

-----Original Message-----
From: Tobias Litherland [mailto:tobiasli@student.geo.uio.no]

Sent: Wednesday, March 20, 2013 1:19 AM
To: Liston,Glen
Subject: Questions regarding SnowModel

Hello Mr. Liston,

I am a student using SnowModel in my master thesis, and I have two questions regarding the model. I would be very grateful if you have time to answer them.

---

1) Regarding two-layer snow in regards to transport: In your Snowtran-3D paper from 2007 (Simulating complex snow distributions in windy environments using SnowTran-3D, Liston et al 2007) you state that:

"At any point in time when the snow threshold velocity exceeds a value for snow that cannot be transported by naturally occurring winds (e.g. $u_{(*t)} \geq 1.7$ ms^(-1), corresponding to a 10 m wind speed of approximately 40 ms^(-1)), the soft snow layer is added to the hard (unmovable) snow layer."

In the model code there is a temperature threshold of 3°C controlling if the soft layer is added to the hard layer, but I can't seem to find a threshold velocity condition for the soft/hard layer shift. Is this condition implemented?

---

2) I am interested in a modelling area of about 2000*2000 grid cells. Have you any experience running the model at these grid sizes?

Thank you for any feedback!

Tobias Litherland
hydrology student at the University of Oslo